UNIVERSITY OF HELSINKI
FACULTY OF SCIENCE

Towards radiolabeled tracers for the Cs-rich microparticles released from the FDNPP accident for *in vivo* studies

TRACERS IN MOLECULAR IMAGING

Radiopharmaceutical Research at the University of Helsinki

Master's Programme in Chemistry and Molecular Sciences

Radiochemistry study track

Master's thesis

Author:

Patricia Valdés Portas

Supervisor(s):

Mirkka Sarparanta

Surachet Imlimthan

05.06.2024

Helsinki

Abstract

Faculty: Kumpula (Faculty of Science)
Degree programme: Master's Programme in Chemistry and Molecular Sciences
Study track: Chemistry and Molecular Sciences
Author: Patricia Valdés Portas
Title: Towards radiolabeled tracers for the Cs-rich microparticles released from the FDNPP accident for in vivo studies
Level: Master's
Month and year: May 2024
Number of pages: 130
Keywords: cesium-rich microparticles (CsMPs), borosilicates, radiolabeling, positron emission tomography (PET)
Supervisor or supervisors: Mirkka Sarparanta, Surachet Imlimthan
Where deposited: this thesis is archived in the Digital Repository of the University of Helsinki/E-thesis.
Additional information: -
Abstract: The Fukushima-Daiichi Nuclear Power Plant (FNDPP) accident on March 11, 2011, resulted in the release of radioactive cesium-rich microparticles (CsMPs), which can travel long distances thanks to their small size and light weight. Since the long-term radiobiological health-effects and accumulated radiation dose of inhaled CsMPs remain unknown, this thesis proposes a model for tracking synthetic 44-µm and 2.2-µm borosilicate microparticles, which resemble the SiO_2 composition and spherical morphology of CsMPs, under Positron Emission Tomography (PET) by radiolabeling them with positron-emitting radionuclides. The use of 44-µm microparticles was discontinued early on as the size of the 2.2-µm particles was more representative of the more common type A CsMPs (0.1-10 µm). Three different radiolabeling approaches were pursued along this project, two directed at ^{68}Ga-labeling, and a third one at ^{18}F-fluorination. The first and main approach was based on the surface functionalization of the particles with (3-aminopropyl)triethoxysilane (APTES) and a suitable chelator for the coordination of [^{68}Ga]Ga^{3+} ions, like 2,2′-(7-(1-carboxy-4-((4-isothiocyanato-benzyl)-amino)-4-oxobutyl)-1,4,7-triazonane-1,4-diyl)diacetic acid (p-NCS-Bn-NODAGA) or desferrioxamine (DFO). The second approach involved surface functionalization with ethanolamine, polyethylene glycol (PEG) and DFO. The third approach was based on the natural ability of [^{18}F]F^- to substitute silanol groups present on the surface of the borosilicates. Surface

functionalization with APTES was confirmed using X-ray photoelectron spectroscopy (XPS), zeta potential and elemental analysis, as opposed to functionalization with PEG-ethanolamine. Scanning electron microscopy (SEM) images showed no significant morphological alterations upon functionalization. ^{68}Ga-labeling of the NODAGA-APTES functionalized 2.2-μm borosilicates was achieved with a mean radiochemical yield (RCY) and radiochemical purity (RCP) of 65 ± 5% and 94 ± 2%, respectively. ^{68}Ga-labeling of DFO-APTES and DFO-PEG-ethanolamine functionalized 2.2-μm borosilicates was not successful (RCY below 15% and RCP of about 50%). ^{18}F-fluorination was not successful due to the high tendency of [^{18}F]F-Si bonds to undergo hydrolysis in aqueous media. The stability of the final [^{68}Ga]Ga-NODAGA-APTES product over a 0-3 hour time period was higher than 90% in five different simulated physiological conditions. The results of this project serve as a promising prospect for the design of radiotracers resembling CsMPs for PET tracking upon *in vivo* administration.

Acknowledgements

I would first like to thank my supervisors, Mirkka and Oxy, for giving me the opportunity of participating in such a relevant and interesting project and guiding me throughout every step of this thesis. Thank you Mirkka for being an incredible thesis director, group leader, teacher, and role model. Thanks to you I have been able to experience amazing opportunities beyond the extent of this thesis. Thank you Oxy for being a patient and understanding supervisor. You have taught me how to set my limits and to be proud of my job, and I will always remember this in the future.

Thank you Gareth for being an amazing thesis co-director and director of the chemistry unit. Thank you for supporting me in the early stages of my scientific career and being a close and attentive person. Thank you to Alvin and Gianni for helping me during this thesis and being two great co-supervisors. Thank you to Satoshi and Kanako for supporting this thesis all the way from Japan. Special thanks to Anna and Natalia, for being my two biggest supports throughout this year. I really cannot put into words how grateful I am for you being by my side, and I don't think this would all have been possible without you.

Thank you to all of the personnel in the radiochemistry unit and the responsible people of the characterization techniques. You help has been essential for the understanding and completion of this research.

I would also like to thank my friends and family for supporting me during these two years I have spent far away from home. I would especially like to thank Aida, for telling me when I was being dramatic, and for staying with me until late in the night when I needed company while writing this manuscript. You know that it would all have been very different without you. Finally, the biggest thanks to Franito for being the best possible boyfriend in the distance, for helping me with science many kilometers away, for comforting me when I was not feeling the best, and for staying with me even when I know how difficult I can be sometimes. You have given me the strength to finish this project and all of the things I have achieved until now. Thank you.

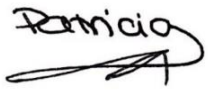

Table of contents

List of abbreviations and symbols

α – Alpha Radiation
β⁺ – Positron Radiation
γ – Gamma Radiation
ALI – Air-Liquid Interface
APTES – (3-Aminopropyl)triethoxysilane
AT-I – Alveolar Epithelial Type I Cells
AT-II – Alveolar Epithelial Type II Cells
BE - Bronchial Epithelial Cells with Cilia
BD – Biodistribution
BGO – Bismuth Germanium Oxide
C – Clara Cells
COOH – Carboxylic Acid
CsMPs – Cesium-rich Microparticles
DFO – Desferrioxamine
DIPEA – N,N-Diisopropylethylamine
DMF – N,N-Dimethylformamide
DMSO – Dimethyl sulfoxide
DOTA – 2,2′,2”,2”'-(1,4,7,10-Tetraazacyclododecane-1,4,7,10-tetrayl)tetraacetic acid
EC – Endothelial Cells
EDG – Electron Donating Group
EDS – Energy Dispersirve Spectroscopy
EDTA - Ethylenediaminetetraacetic acid
ERDA – Elastic Recoil Detection Analysis
EtOH – Ethanol
EWG – Electron Withdrawing Group
FDNPP – Fukushima Daiichi Nuclear Power Plant
FTIR – Fourier Transform Infrared
GC - Goblet Cells
IAEA – International Atomic Energy Agency
iTLC – Instant Thin Layer Chromatography
LET – Linear Energy Transfer
LNT – Linear Non Threshold
LOR – Line of Response
M - Macrophages
MCCIs – Molten Core Concrete Interactions
MPs – Microparticles
NHS – N-hydroxysuccinimide
NISA – Nuclear & Industrial Safety Agency
NOTA – 2,2′,2”-(1,4,7-triazacyclononane-1,4,7-triyl)triacetic acid
PBS – Phosphate Buffered Saline
PD – Pharmacodynamics
PEG – Polyethylene glycol

PET - Positron Emission Tomography
PK – Pharmacokinetics
PMT – Photomultiplier Tube
***p*-NCS-Bn-NODAGA** – 2,2′-(7-(1-carboxy-4-((4-isothiocyanatobenzyl)amino) -4-oxobutyl)-1,4,7-triazonane-1,4-diyl)diacetic acid
***p*-SCN-Bn-DFO** – 1-(4-Isothiocyanatophenyl)-3-[6,17-dihydroxy-7,10,18,21-tetra-oxo-27-(N-acetylhydroxylamino)- 6,11,17, 22- tetraazaheptaeicosine] thiourea
RCY – Radiochemical Yield
RCP – Radiochemical Purity
RPV – Reactor Pressure Vessel
SCX – Strong Cation Exchange
SiFA – Silicon Fluoride Acceptor
SA – Silicic Acid
SEM – Scanning Electron Microscopy
SG – Silica Gel
SOS – Start Of Synthesis
SPE – Solid Phase Extraction
TGA – Thermogravimetric Analysis
ToF – Time of Flight
XPS – X-ray Photoelectron Spectroscopy

1 Introduction

In March 2011, the consequences of a tsunami originated at the north-east coast of Japan lead to the failure of the backup generators for the cooling of four nuclear reactors of the Fukushima Daiichi Nuclear Power Plant (FDNPP). This resulted in a tragic series of explosions, where large amounts of radioactive contaminants were released into the atmosphere and dispersed several kilometers away from the nuclear site.[1]

Due to the high temperatures associated with the meltdown of the reactors, cesium-134 and cesium-137 reacted with concrete and associated with SiO_2, forming micron sized cesium-rich microparticles (CsMPs) that spread up to 200 km away from the Fukushima prefecture. The most predominant type A CsMPs are of about 0.1 - 10 μm in size with a spherical morphology, although larger particles have also been reported. The relatively long half-life of radioactive cesium raises important long-term health concerns regarding about the fate of emitted CsMPs.[2–4]

The small size of CsMPs (0.1 - 10 μm) poses a significant inhalation risk (**Figure 1**, **A**). While larger particles can be expelled through mucociliary clearance, small particles of about 1 - 5 μm can penetrate the alveoli and enter the blood stream, potentially reaching the brain, the gastrointestinal track, and other organs. The exact distribution and accumulation of CsMPs along the human body has not been precisely assessed yet, as their overall low activity of 10^{-2}-10^{2} Bq/particle limits their direct observation using nuclear medicine imaging techniques. Furthermore, the dynamics of radiocesium cannot be directly studied in animals because of their large tissue thickness, which prevents the observation of β rays emitted by cesium-134 and cesium-137.[5–8]

Radiolabeling CsMPs with positron emitting could provide precise tracking of their distribution along the body under Positron Emission Tomography (PET). PET allows for a real time follow-up of positron emitting radiotracers upon *in vivo* administration (**Figure 1**, **B**). However, experimentation with real CsMPs is limited because of the difficulties associated with their obtention and isolation. Synthetic borosilicate microparticles can be used as surrogates thanks to their spherical morphology, size similarity and SiO_2-based matrix, resembling that of CsMPs. Their evaluation under PET can therefore help determine the potential accumulation of CsMPs along the body.

If this factor was to be precisely assessed, estimation of the radiobiological health related to the inhalation and accumulated dose of CsMPs could allow for the application of preventive policies towards the affected population.

Radiometals are of great interest in radiochemistry due to their wide versatility for diagnostic and therapeutic applications. Gallium-68 (half-life of 67.629*(24)* minutes) is one of the most widely used radiometals for PET imaging, and it is routinely produced in many radiopharmaceutical laboratories. The relatively easy accessibility of gallium-68 makes it a nice candidate for the design of radiotracers used in PET imaging. One of the main limitations related to the use of gallium-68 is its relatively short half-life, which limits its use for extended *in vivo* tracking studies. Alternative longer lived radionuclides like zirconium-89, with a half-life of 78.41*(12)* hours are more interesting for advanced studies. Chelators derived from the NOTA – 2,2′,2”-(1,4,7-triazacyclononane-1,4,7-triyl)triacetic acid (NOTA) moiety, like 2,2′-(7-(1-carboxy-4-((4-isothiocyanatobenzyl)amino)-4-oxobutyl)-1,4,7-triazonane-1,4-diyl)diacetic acid (*p*-SCN-Bn-NODAGA) are more the most suitable for the coordination of $[^{68}Ga]Ga^{3+}$ ions thanks the compatible size of the cavity with the ionic radius. Desferrioxamine (DFO) derived chelators can also coordinate $[^{68}Ga]Ga^{3+}$, but are better suited for $[^{89}Zr]Zr^{4+}$ ions.[9–11]

Grafting of a suitable chelator capable of coordinating $[^{68}Ga]Ga^{3+}$ ions depends on the chemistry between the surface of the synthetic microparticles and the reactive group of the chelator moiety. Grafting an appropriate chelator requires prior functionalization of the particles for its conjugation through appropriate reactive groups. However, excessive surface functionalization must be avoided in order to preserver the natural surface properties of the synthetic microparticles.

The use of APTES as a functionalization agent in glass surfaces has been extensively reviewed for a wide variety of applications. Grafting of APTES is based on a silanization reaction with silanol groups present at the surface of borosilicates. APTES branches expose free amine ends on the surface of the microparticles. Chelator moieties with free isothiocyanate groups can react with these free amine ends forming a thiourea bond. The use of longer functionalizing units composed of polyethylene glycol (PEG) polymer conjugated to ethanolamine molecules was proved an effective method for the surface functionalization of solid glass supports in the past. The

distance provided by the use of a flexible PEG linker allows functionalized supports to react with other molecules in their native way.[12–14]

The use of alternative PET radionuclides like fluorine-18 has also been widely reported throughout the years. Substitution of hydroxyl groups exposed by silanol-containing molecules with $[^{18}F]F^-$ has been reported, although the stability of the [18F]F-Si bond is often compromised by its tendency to undergo hydrolysis in aqueous media.[15–17]

The aim of this study was to design and optimize an appropriate functionalization method for radiolabeling of synthetic borosilicate particles resembling CsMPs released from the FDNPP. Beyond the scope of this thesis, the end goal of this project is to determine the potential radiobiological health effects associated with the inhalation of CsMPs to develop appropriate prevention measures.

Three different approaches were evaluated throughout the extent of this project, two of them directed for ^{68}Ga-labeling and a third one based on ^{18}F-fluorination. Initially, amine-end surface functionalization was pursued using (3-aminopropyl)triethoxysilane (APTES), followed by the conjugation to 2,2′-(7-(1-carboxy-4-((4-isothiocyanatobenzyl)amino)-4-oxobutyl)-1,4,7-triazonane-1,4-diyl)diacetic acid (p-NCS-Bn-NODAGA) or 1-(4-Isothiocyanatophenyl)-3-[6,17-dihydroxy-7,10,18,21-tetra-oxo-27-(N-acetylhydroxylamino)- 6,11,17, 22- tetraazaheptaeicosine] thiourea (*p*-SCN-Bn-DFO) derived chelators, suitable for coordingating $[^{68}Ga]Ga^{3+}$ ions. The second method was based on an alternative functionalization based on building of PEG-Ethanolamine moieties and conjugation with desferrioxamine (DFO) mesylate salt. The final approach, oriented to the direct ^{18}F-fluorination of the silica microparticles was based on the natural ability of $[^{18}F]F^-$ to substitute surface silanol groups. A general guide for the pursued experiments is provided in the graphical abstract shown in **Figure 1**, **C**.

Characterization of the surface functionalization of the particles was evaluated using Fourier transform infrared spectroscopy (FTIR), zeta potential, thermogravimetric analysis (TGA), elemental analysis, scanning electron microscopy (SEM), energy dispersive spectroscopy (EDS), X-ray photoelectron spectroscopy (XPS) and elastic recoil detection analysis (ERDA). Radiolabeling was carried out with gallium-68 and fluorine-18, and experimental conditions were optimized based on

acquired radiochemical yield (RCY), radioactivity concentration, specific activity (A_S) and radiochemical purity (RCP) results. Stability assays were performed over a 0-3 hour time period in five different simulated physiological media, which were 1 x phosphate buffered saline (PBS), 50% human plasma in 1 × PBS, 0.2 mM iron chloride ($FeCl_3$), 2 mM ethylenediaminetetraacetic acid (EDTA) and simulated lung fluid (SLF).

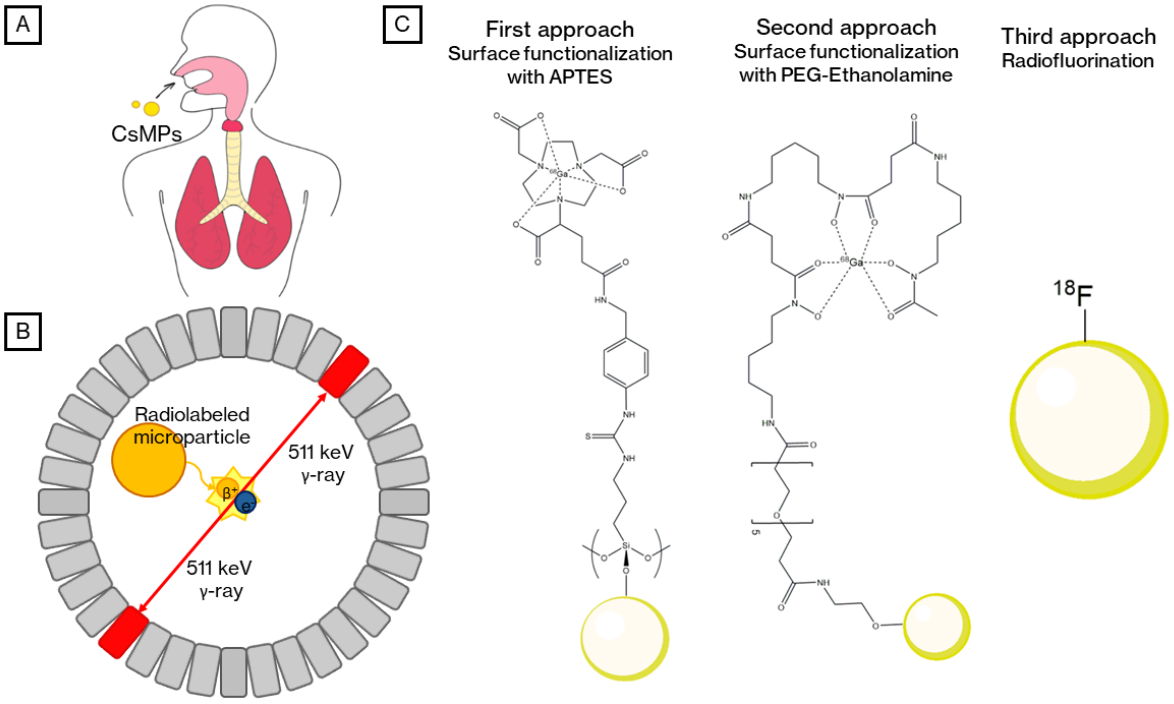

Figure 1. Graphical abstract representing the overall composition of this thesis. (A) Inhalation of CsMPs, (B) Tracking of radiolabeled microparticles under Positron Emission Tomography (PET), (C) Different radiolabeling approaches followed throughout the extent of this study.

2 Literature review

2.1 Fukushima-Daiichi Nuclear Power Plant (FDNPP) accident

The FDNPP accident led to the emission of copious amounts of radioactive contaminants that spread widely outside the Fukushima prefecture potentially affecting the surrounding population and biota.

2.1.1 Disaster timeline and overview

On March 11, 2011, a magnitude 9.0 and 3-minute duration earthquake centered 130 km away from Sendai, in the north-east coast of Japan, originated a tsunami that flooded 650 km^2 of the country and took more than 19 500 lives.[18] The tsunami run over the coastal FDNPP installations, disabling its back-up generators responsible for the cooling of 4 out of 6 nuclear reactors of the facility, and subsequently giving place to Unit 1, 3 and 4 explosions on March 12, 14 and 15 respectively. The events resulted in the partial meltdown of 3 reactors and the release of 5.2×10^{17} Bq in radioactive contaminants. The superficial contamination of the area and the waste treatment of all four reactors as well as their contaminated cooling water is yet to be resolved. However, *on-site* actions are limited due to the very high radiation levels surrounding the power plant area.[1]

The FDNPP was initially designed taking into consideration the likelihood of a 10-meter-high tsunami, nevertheless the waves reaching the facility that day were of about 15 meters high. The International Atomic Energy Agency (IAEA) had previously called out for preparation against more dramatic scenarios, years prior the disaster, but the power plant continued operating normally under the supervision of the Japanese Nuclear and Industrial Safety Agency (NISA).[18]

While the earthquake did not cause any damage to the reactors, six power supplies were destroyed, which resulted in the shutdown of units 1-3 and subsequent activation of their emergency cooling protocols. Once the tsunami run over the installations, both auxiliary cooling and condenser circuit pumps were disabled, as well as the electrical system and batteries below some of the buildings, emergency reparations being not possible due to the consequences of the tsunami over the roads surrounding the facility. Failure of the cooling systems resulted in the meltdown of

reactors 1-3 which ultimately produced the rupture of the pressure vessels and led to the subsequent hydrogen explosions of units 1, 3 and 4 on the following days.[18]

On the aftermath of the accident, the Tokyo Electric Power Company Holdings (TEPCO), responsible for the management of the nuclear facility, proposed a management plan for the treatment of the reactors with focus on the decommissioning of units 1 to 6, the removal and relocation of spent fuel, and the decontamination of the water used as a fuel coolant when the accident took place. Economical compensation to citizens and business was provided by TEPCO, which received its funding from the Japanese government and power companies over the years, and has also been dedicated to the treatment of the power plant and contaminated areas.[18]

2.1.2 Cesium-rich microparticles (CsMPs)

Cesium radioisotopes obtained as fission products were liberated from the UO_2 reactor fuel after its temperature rose up to about 2200 K. The amount of released cesium-134 and cesium-137 was of 10^{15}-10^{16} Bq.[4] Radiocesium-based contaminants were immediately considered of high importance due to their volatility and high dispersion range, soil-assimilation capabilities, and long half-lives with respect to the rest of emitted radionuclides (30.07*(3)* and 2.0648*(10)* years from cesium-137 and cesium-134, respectively).[19] Insoluble cesium-rich microparticles (CsMPs) rapidly distributed along land and sea, through air convection transport, as well as dry and wet deposition mechanisms. Upon atmospheric release, the amount of radioactivity that reached the sea was much higher than that which remained on land, of 12-15 PBq in cesium-137 measured along the Pacific Ocean, and 3-6 PBq throughout the terrain.[3]

Radioactive cesium can be found in contaminated areas either as soluble CsI or CsOH readily formed upon fission that can readily adsorb onto clays, as sparingly soluble Cesium-rich microparticles (CsMPs) of very high specific activity (about 10^{11} Bq/g) or embedded into larger particles in lower amounts (400 μm diameter with approximately 10^{7} Bq/g).[4,20]

Ultimately, a suggested division between these two types of particles has recently been made, dividing the forementioned in two main classes called type A and type B CsMPs. The more commonly observed type A CsMPs are smaller and spherical-shaped, with particle diameters ranging between 0.1-10 μm, expected to come from

units 2 and 3 based on their $^{134}Cs/^{137}Cs$ activity ratio. On the other hand, type B CsMPs are larger, of about 50-400 μm, and of diverse shapes not necessarily spherical, in this case suspected to be originated from the initial Unit 1 explosion. These are more porous in general, with 3.7–34% to 0.78–53% measured porosity in type A versus B respectively, and it has been suggested that, even their composition with respect to type A CsMPs is very similar, their elemental distribution is not homogeneous.[3]

As previously mentioned, the smaller type A particles present radioactivity values up to 10^4 Bq/mm^3 higher than those larger from type B, in which case the activity is also unevenly distributed due to their morphology. Nevertheless, the general activity emitted from a single type B particle (10^1-10^4 Bq/particle) is higher than one from type A (10^{-2}-10^2 Bq/particle), due to their larger size and subsequent higher content in radiocesium.[3]

CsMPs are thought to be formed upon condensation of fission-born [$^{134+137}$Cs]CsOH and [$^{134+137}$Cs]Cs Cl products, and Zn/Fe oxide nanoparticle aggregates, into SiO_2 between reactor fuel and concrete. The accumulation of molten fuel in the reactors lead to the rupture of the reactor pressure vessels (RPVs), which put fuel in contact with the surface underlying the RPVs. CsMPs were generated in Units 1, 2 and 3 from molten core and concrete interactions (MCCIs).

Most CsMPs have been found to be of a spherical shape and composed of 1.0-1.9% cesium content (percentage by weight) present as Cs_2O. They are also able of encapsulating heavier radioactive uranium traces, which also associates them with the emission of alpha (α) radiation.[1] Since CsMPs are essentially glass microparticles with embeddedcesium-134 and cesium-137, their solubility rates are somehow poor as seen for silicate-based glasses, which makes them prone to remaining in the environment and biological organisms over decades.[2]

Apart from their Cs content and SiO_2-based structure, CsMPs present a wide variety of constituent elements, which are dissolved in the glass matrix. Among these are Fe and Mn, components of the RPVs; Zn, constituent continuously added to the water of the reactor to form a barrier layer that prevented radioactive corrosion; Rb, Pb, Sn as these are common fission products, with the addition of Sn also incorporated from the melting of the Zr/Sn alloy of the fuel rods that were filled with the fuel pellets; Cl, present in the seawater that impacted the prefecture; W, as an impurity of the Zr/Sn

alloy rods; and uranium, an important fuel constituent that is present in CsMPs in trace amounts.[1,21]

Uranium was incorporated into CsMPs as the presence of O within the reaction fuel allows for the oxidation of uranium, which facilitates its volatility at lower temperatures. Studies regarding $^{235}U/^{238}U$ ratios of studied CsMPs have proved that these remain homogeneous among type A CsMPs, indicating that they were likely incorporated from the formation of melted fuel in the RPVs.[1,21] The incorporation of U CsMPs may be very significant as it also makes them an α radiation hazard of extremely long half-lives (7.04×10^8 years and 4.5×10^9 years for uranium-235 and uranium-238)[19] that otherwise would not have been distributed as widely.[2] However, the possibility of CsMPs effectively emitting α radiation is reduced by the low penetrating range of α particles in the surrounding borosilicate matrix.

The physicochemical properties, activity, and size discrepancies between CsMP types has been explained based on their formation mechanisms, as type A particles were likely formed through condensation of gas species, mainly SiO vapor that was able to incorporate higher volatile cesium-134 and cesium-137 amounts, whereas type B were born from the solidification of MCCIs composites. Further examination shows that spherical particles among those of type B seem to belong to an intermediate situation between both classes. It has been suggested that in their case, the release of forementioned volatile radioactive compounds was prevented through a much faster cooling rate, which in turn resulted in higher activity concentration values than those of typical type B CsMPs.[3]

2.1.3 Consequences of the FDNPP accident

Citizens within a 20 km radius of the site were evacuated March 11-13 upon nuclear emergency state declaration from the Japanese Government. Such fast measure resulted in zero recorded deaths directly caused by the nuclear accident, the initial tsunami being the principal responsible of the counted fatalities. Nevertheless, the high volatility of produced CsMPs involved their high distribution throughout the area. The presence of CsMPs several kilometers away from the facility has been demonstrated through superficial soil measurements. CsMPs have also been detected on air filters, as far as to reaching the capital Tokyo, which is 230 km away from the site, suggesting their distribution through air mass convection mechanisms.[4]

Transport of CsMPs has been drawn upon nine radioactive plumes, recorded in **Figure 2**, whereas deposition took place due to precipitation events. Soil sample analytical studies have proven that the presence of CsMPs is mainly focused northwest and southwest of the FDNPP. Based on the quantification of the radioactive fraction of CsMPs, it has been shown that these were likely deposited outside a 30 km radius from the facility whereas soluble species containing cesium-134 and cesium-137 remained in the nearby soil. CsMPs are still suspected to undergo further transport over the years due to mechanisms like saltation or suspension.[4]

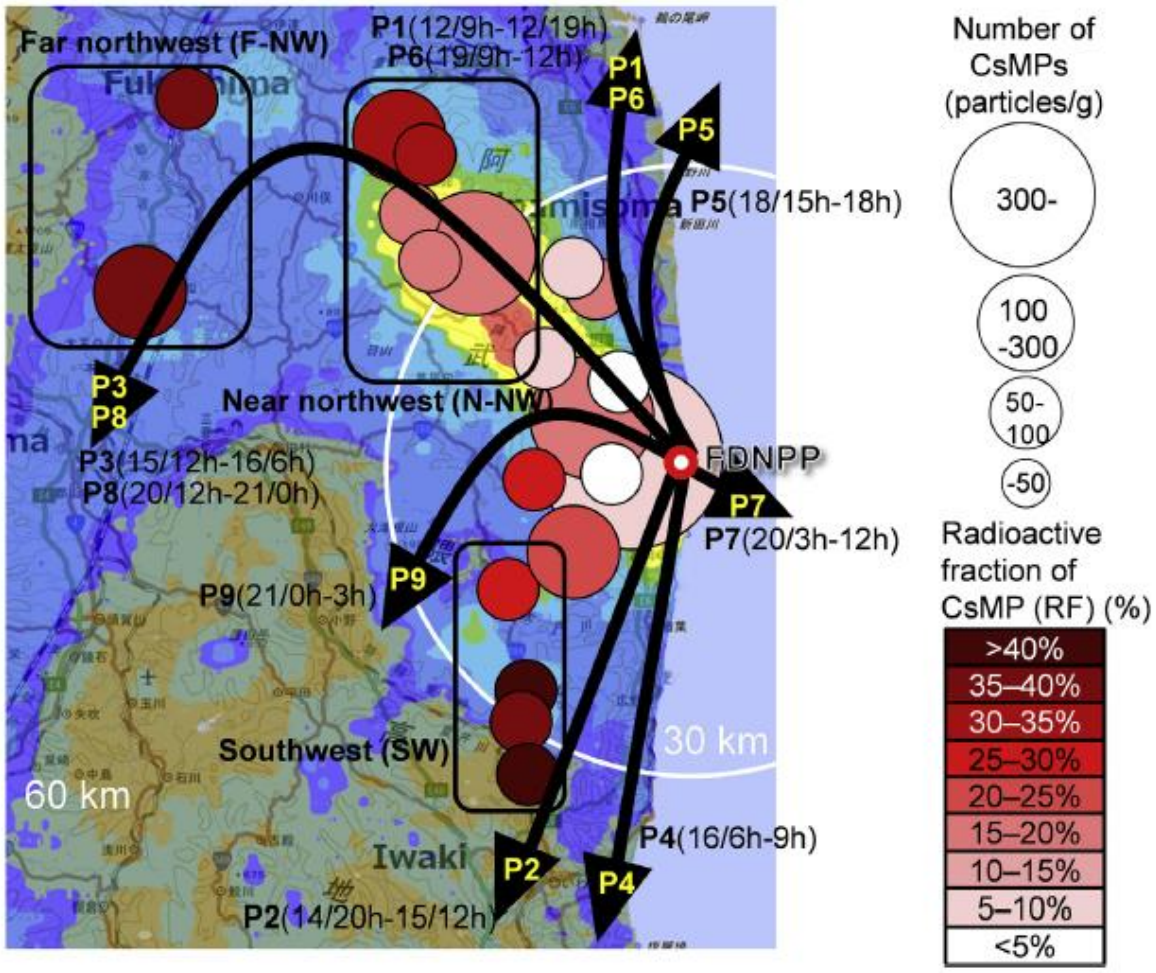

Figure 2. Distribution and trajectory maps of emitted CsMPs and major transportation plumes, respectively. Particle amount and radioactivity values of CsMPs by regions is represented coloured circles as according to legend. Two 30 and 60 km circumference can be distinguished in white. Plumes are indicated with an arrow as Plume(P) number (Day in March 2011/time of start-Day in March 2011/end time). Reprinted with permission from "Abundance and distribution of radioactive cesium-rich microparticles released from the Fukushima Daiichi Nuclear Power Plant into the environment" by R. Ikehara, et al. © 2019 Elsevier Ltd .[4]

The small size of the CsMPs poses them as an inhalation threat as they can easily penetrate into the airways of organisms, exposing tissue and fluids to beta and gamma, and even to α radiation in the case the particles have incorporated U traces onto their

structure.[2] Their wide distribution outside the Fukushima prefecture expands the issue to a much greater area than that initially evaluated, and subsequently extending the problem to a larger number of exposed populations. The exact radiobiological health effects related to the inhalation of CsMPs remain unknown but still represent an important area of study based on the long half-lives of cesium radioisotopes.

Several studies have approached the mortality and morbidity effects related to exposure of radionuclides. These are mainly based on Linear Non Threshold (LNT) human models based on the assumption that the probabilities of radionuclide disintegration and cell transformation are equivalent, and that those transformed cells present, at the same time, equal probability of developing into cancer. In the FDNPP accident, about 2200 people received a radiation dose of 100–500 mSv, which is an alarming number considering that historically, 100 mSv has been the referential dose for the development of significant cancer risks. Even though no deaths were directly associated to the nuclear accident, it has been estimated that about 730–1260 fatalities were related to the aftermath, either because of cancer, worker exposure, or course of the evacuation order. Future cancer mortality and morbidity cases are expected to be of 1500 and 1800 at maximum, respectively, although this digit may vary significantly as different references fail to agree on a common number.[22]

Marine biota was not significantly affected by the accident as ^{137}Cs concentrations were rapidly diluted. Even though FDNPP accident-related doses were recorded in zooplankton and mesopelagic fish, it was estimated that ^{137}Cs concentrations in seafood did not imply relevant radiation risks for consumers, though the industry was extremely subjected to criticism, regulation, and overall population fear. On the other hand, significant effects have been recorded along the terrestrial ecosystem, from cell aberrations associated to hereditary random mutations observed in *Zizeeria maha* grass butterflies; decreased blood cell counts and higher ^{137}C levels in wild monkeys in comparison to populations located far away from the accident; reduced number of bird, cicada and butterfly species related as observed after the release of radioactive contaminants on the Chernobyl accident; and worsened reproductive performance of birds as seen in *Accipiter gentilis* goshawks, with added difficulties related to the incubation and hatching of offspring growing in contaminated nests. Furthermore, radiobiological effects are also suspected to have an effect on the surrounding flora, as

morphological abnormalities, similar to those observed in pine trees affected by the Chernobyl accident, have been reported for *Abies firma* fir trees.[22]

2.2 Biological effects of inhaled micro and nanoparticles

The possible biological routes of inhaled CsMPs must be studied in order to estimate the associated radiobiological health effects derived from accumulated radiation dose.

2.2.1 Destination of inhaled particles

Micro and nanomaterials can be incorporated into biological systems through inhalation thanks to their small size. Toxicological effects of inhaled particles are assessed based on the relationship between exposure, radioactive dose, and biological response.[23]

Exogenous nanoparticles can interact with biomacromolecules like nucleic acids or proteins due to their similarity in size, whereas microparticles are more likely to interact with cells for the same reason. In contact with tissue, interactions like adhesion or encapsulation, will take place depending on the chemical composition, lipophilicity, size, shape, aggregation and physico-kinetic properties of inhaled particles.[5] Intrinsic characteristics of the affected organism, like breathing pattern and lung morphology, can influence the biological destination of inhaled particles along the organism.[6]

The human body prevents the penetration of nano and microparticles through internal and external surfaces with an effective epithelial barrier sitting on top of connective tissue. Goblet (GC) and Clara (C) cells produce a protective mucus membrane along bronchi and bronchioles, respectively. Bronchi and bronchioles are also covered with epithelial ciliated cells (BC). Further down along the respiratory track, the epithelia lining covering alveolar cells is the thinnest (0.1–0.2 μm) and most permeable barrier of the body. These are in contact with the endothelial layer that protects blood vessels conforming what is known as the “air-blood barrier”... [7,24]The air-blood barrier is the most permeable barrier in humans. It consists of alveolar epithelial type I (AT-I) cells and surfactant-producing alveolar type II (AT-II) cells, as well as capillary endothelial cells and alveolar macrophages. Endothelial cells are

found at the base of the alveolar epithelium, while macrophages are located on top of the layer, as can be seen in **Figure 3**.[7]

Upon inhalation, microparticles tend to harmlessly collide with the upper respiratory tract like the throat or mouth. Large foreign particles can become entrapped in the mucosa lining and can be expelled by ciliated cells, process known as "mucociliary clearance". Smaller microparticles can reach the alveoli and become phagocytized by macrophages, process known as "macrophage uptake", which is represented along **Figure 3**. [6,7]

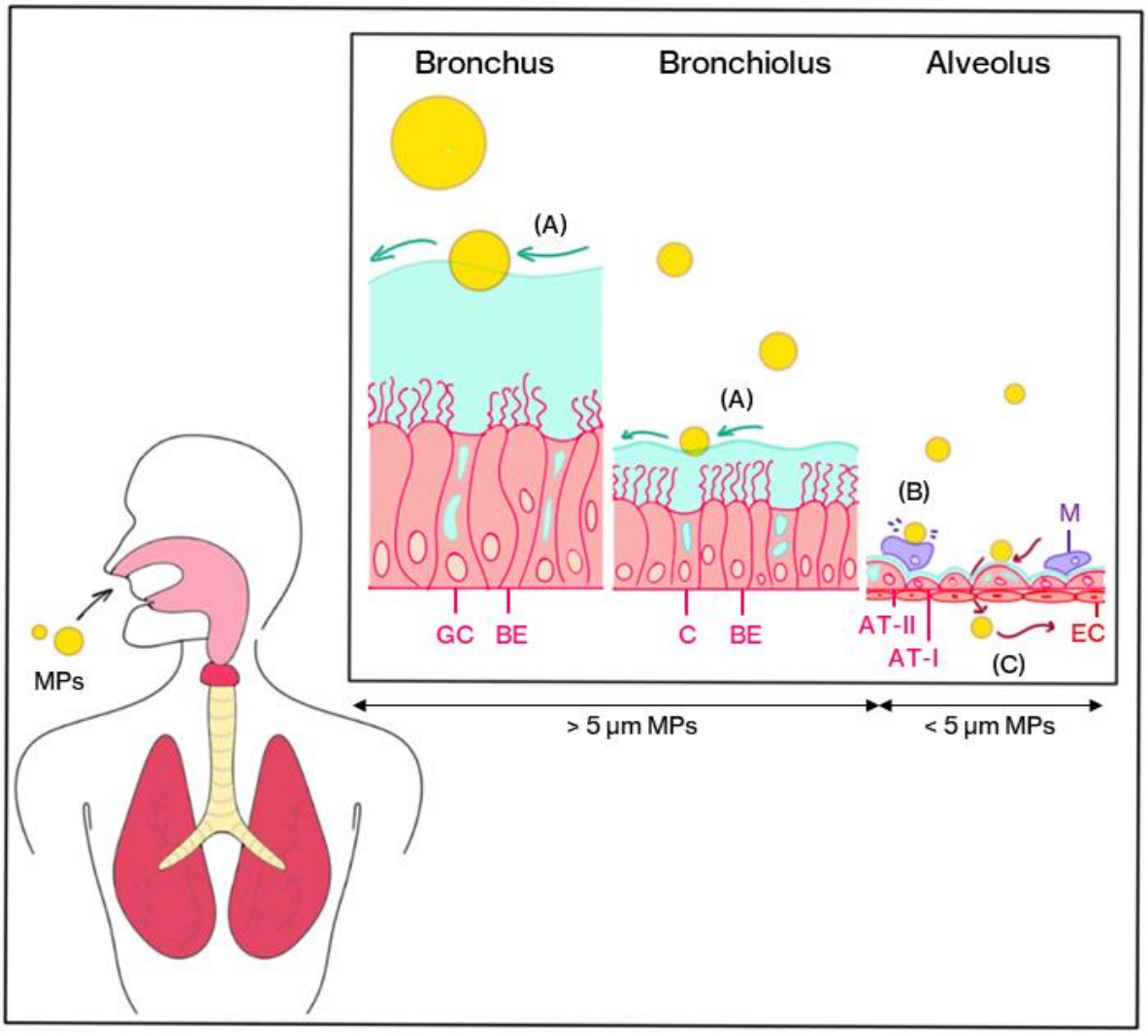

Figure 3. Schematic representation of the distribution of microparticles (MPs) along the respiratory track of humans. Three processes have been differentiated, which are (A) mucociliary clearance, (B) macrophage uptake and (C) penetration of the air-blood barrier. Smaller particles remain in the bronchus and bronchioles, whereas smaller particles can reach the alveolus. Indications stand for bronchial epithelial cells with cilia (BE), goblet cells (GC), Clara cells (C), macrophages (M), endothelial cells (EC), alveolar epithelial type I cells (AT-I) and alveolar epithelial type II cells (AT-II), Mucus is represented in blue. This drawing has been elaborated using the indicated literature as references.[7,24]

However, when small foreign particles within 1-5 μm can reach the alveoli through inhalation, they will likely undergo gravitational sedimentation and could incorporate into the systemic circulation by diffusion. These could therefore affect the organism, and, in extreme situations, potentially increase disease and mortality. In contrast, if particles happen to be extremely small (< 0.5-1 μm), they could be dragged again outside of the body by the inhalation pattern up to exhalation, avoiding lung sedimentation or being randomly deposited along unspecific parts of the respiratory track.[6]

Upon deposition along the respiratory track, insoluble particles can be further translocated to the gastrointestinal track, spleen, liver, kidney, among others. Exogenous microparticles can also reach the foetus in the case of pregnant animals. It has also been observed that migration from the olfactory bulb to the brain can take place upon absorption of the microparticles in the olfactory mucosa, which is found in the nose. This represents an important contribution to take into consideration in mice used for experimentation, as this effect is significantly higher in rodents than humans. Ultimately, particle clearance in humans has shown to be occasionally achieved through translocation onto the gastrointestinal track.[5]

2.2.2 Inhalation studies regarding particle distribution

Toxicological effects of inhaled nano and microparticles in living organisms is proportional to their exposure as well as hazardous properties. Toxicity in organisms can be determined based on *in vitro*, *ex vivo*, *in vivo* and *in silico* models.[7]

In vitro systems are mainly based on the study of adverse effects over different body tissues. Cytotoxicity is evaluated by development of a cell culture system, where a specific cell line representing a concrete tissue is set to grow in a proper medium with relatable conditions. The most representative methods for studying the cytotoxicity of respiratory cells are air-liquid interface (ALI) cultures, where cells are exposed to air while being supplied nutrients from the basolateral edge. Co-culture methods among two or more cell types have further been successfully developed with trans-well membrane systems that enable further understanding of the realistic processes taking place in the organism.[25] For ALI studies, incorporation of the foreign particles into the cellular system must be done in an aerosol sprayed-fashion.[7]

In vitro assessments of the alveolar barrier are mainly done with the A549 and H441 cell lines but are still far from the realistic barrier behaviour of alveoli. Diverse co-culture methods of lung tissue cell lines that include macrophages (basolateral and apical compartments, respectively) have proved to be crucial to determine inhalation cytotoxicity. Endothelial models are mainly based on the use of primary cells, directly taken from living tissue like umbilical vein endothelium.[25] EAhy926 cell line has already been used in co-culture studies of the respiratory system for the evaluation of PM10 intake.[26]

The use of *in vivo* systems is also fundamental in particle distribution inhalation studies, which are normally tested on mice or rats. Different exposure methods are normally used, like whole-body exposure, where the particles are sprayed evenly as aerosol for a certain amount of time over a big chamber where animals are; nose/head only exposure, in which mice are placed inside an extended-hole chamber where the aerosol is specifically directed towards the nose of the rodent; or lung-only exposure. The latter one is a method that is normally based in intratracheal instillation or oropharyngeal aspiration of the contaminant into mice or rats. In the former one, a particle delivery device is placed into the trachea of the rodent, and sprays the particles in a pulsated fashion, whereas in oropharyngeal aspiration, the material is deposited over the base of the tongue and becomes inhaled upon inspiration. Lung-only exposure methods are the most widely employed as they can be performed under anaesthesia, whereas whole-body and nose-only exposure methods can cause animal stress and result in chamber suffocation.[7]

Nevertheless, the main problem associated with the use of rodents as *in vivo* models is that they are what is called “obligate nasal breathers”, which means that only air directly taken by the nose will reach their lower respiratory track, as opposed to that taken by the mouth.[7,27] This normally calls for experimentation with different types of animals like non-human primates, which can be challenging as these are often subject to higher costs and stricter regulations. However, extrapolation to human studies can be made based on intratracheal instillation studies of rodents, as the PK of inhaled nanoparticles upon lung absorption are supposed to be identical in both organisms.[28]

Ex vivo models are based on the evaluation of particle effects after exposure and excision of real tissue. Regarding inhalation studies, isolated lungs along with the

trachea and the heart of an animal are placed in an artificial thoracic system, which is kept at 37ºC while lungs are ventilated with warm humidified air containing CO_2. However, this approach is the least reliable as the absence of hemodynamics and lymphatic flow represent non-realistic models, and since lungs can only survive a couple of hours under these conditions before cell death starts taking place.[7]

Finally, *in silico* computational approaches have further been developed over the last years. These evaluate the possible pathways of particles along nasal and oral cavities, airway conducts, and alveoli. Simulations can be optimized depending on particle size and diffusion and deposition mechanisms. Simulations can be obtained as unidimensional prototypes or tridimensional models where fluid dynamics can also be included. [6,29]

2.3 Nuclear imaging studies

This study aims to non-invasively track the fate of CsMPs through the airways of mice or rats, using different methodical models. These are all based on the dynamic observation of the inhaled microparticles under Positron Emission Tomography (PET), using radionuclides with an intermediate half-life of hours to days. One of the main principles of radiopharmaceutical chemistry is the microdosing principle, in essence, the production of highly radioactive tracers that allow for the lowest possible dose for patient administration.[30]

The main goal of radiopharmaceutical chemistry is to design radiotracers that can either target a specific site in the host body (e.g. a tumour), and/or that can replicate the biodistribution (BD), pharmacodynamics (PD) and pharmacokinetics (PK) of a model molecule. If these are based on positron emitting radionuclides, PET imaging could then provide information about the acting site of the radiopharmaceutical as well as its distribution mechanisms along the organism (e.g. tumour location, biological endpoint of a compound). To achieve these functions, PET radiopharmaceuticals must be as similar as possible to the non-radioactive molecules that they trace.[15]

When developing radiotracers, the ideal situation is to use moieties that already contain non-radioactive atoms of the desired radionuclide that will be used for radiolabeling. This would allow to, for example, substituting natural fluorine-19 atoms

already present in the original pharmaceutical, with fluorine-18, with minimal alteration of the original molecule. This would conform what is called an "isotopologue" of the original molecule.[15] Nevertheless, sometimes it is not possible or feasible to create said isotopologues since not all available pharmaceuticals are modified with the desired non-radioactive atoms. In this case, radiopharmaceutical design calls for the incorporation of radionuclides into molecules either through the substitution of already existing groups, or through coordination with stable chelator moieties.[15,16]

2.3.1 PET imaging

Nowadays, Positron Emission Tomography (PET) is one the main techniques used in nuclear medicine diagnostics. PET relies in the observation of the annihilation rays resulting from positron emission.

$$ {}^{A}_{Z}X \rightarrow {}_{Z-1}{}^{A}Y + {}_{+1}{}^{0}\beta + \nu \qquad (1) $$

Radioactive proton-rich nuclei decay to more stable isotopes through the conversion of a proton into a neutron, which involves the production of a positron ($_{+1}^{0}\beta$ or β^{+}) and a neutrino (ν), as shown in equation (1). Positrons are antiparticles of electrons and therefore present the same properties, except for a positive charge. Upon electron and positron interaction, a process called annihilation takes place where the masses of said particles are fully converted into energy, and two annihilation gamma rays of 511 keV each are produced, oriented at a 180º angle that draws a straight path.[17,31]

PET instrumentation is based in the simultaneous detection of these annihilation gamma rays with a circular shaped system conformed of, generally, many independent small bismuth germanium oxide (BGO) crystal detectors that, upon signal processing and 3D image reconstruction, are able to identify the exact place where the radiation has been originated. The construction that defines the path between two detectors is known as "line of response" (LOR), and it allows for detecting where the tracers are located in the body.[17,31] The high density and stopping power, as well as the short scintillation decay time of BGO crystals enhances the detection of true coincidence gamma rays while preventing the recording of secondary coincidence effects, like scattered or random coincidence. Ideal PET systems should present high

detection efficiencies, that allow for optimum recordings of coincidence events with minimized noise, as well as high spatial resolution, which is dependent on the size of the crystals (**Figure 4**).[32]

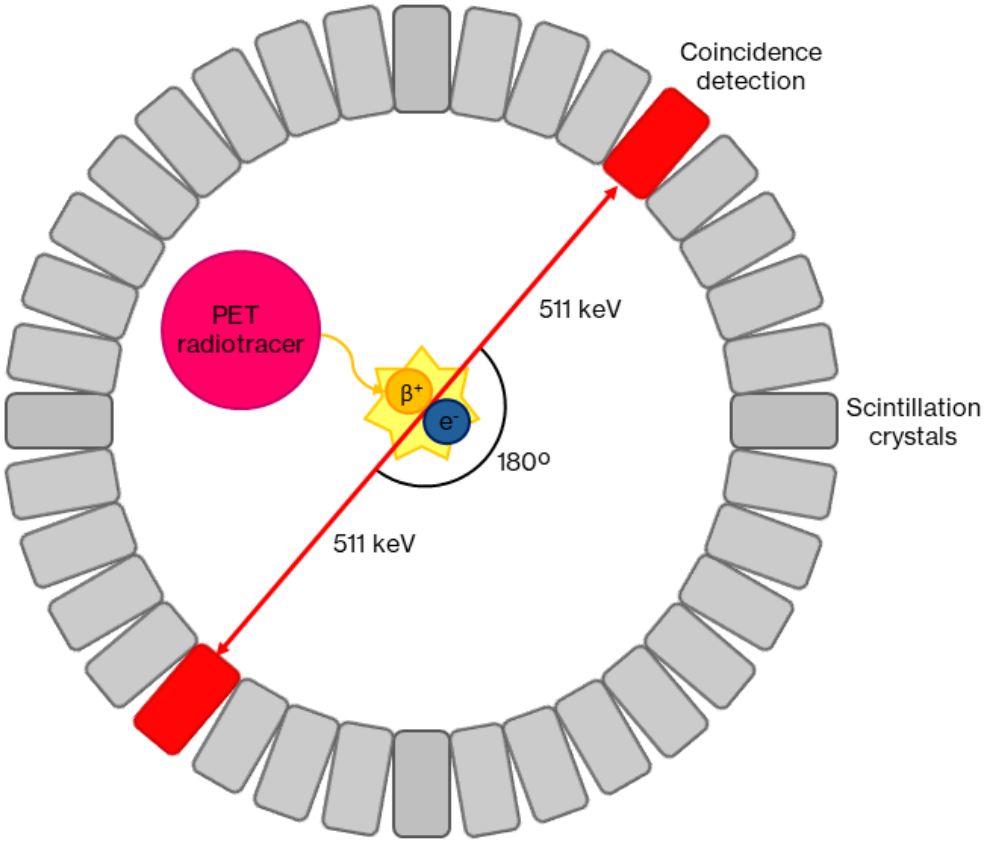

Figure 4. PET imaging overview. Schematic representation of the annihilation gamma rays produced upon positron and electron interaction. Scintillation crystals used in nuclear medicine conform a capsule where patients can lay down during specific measurement times. **T**he positron source is a PET radiotracer previously administered to the patient. Scheme designed taking Wagner et al. and Jiang et al. as template references.[17,33]

Positrons present an intermediate Linear Energy Transfer (LET) value, which means that a major part of their energy is deposited within small distance, and they will only penetrate at maximum a few millimetres in tissue before encountering an electron. On the contrary, annihilation gamma rays have a high LET and can easily reach the outside detectors. When pharmaceuticals are modified with positron emitting radionuclides, designing radiotracers that can specifically target moieties such as tumors, images provided by a PET camera can help identify where the malign cells are located within the host body.[31,34]

2.3.2 Radiometal-chelator chemistry

Radioactive isotopes of metallic elements have been widely used for radiopharmaceutical applications, being referred to as “radiometals”. Different radiometals present different properties that are interesting for either targeted radiotherapy (α and β^- emitters) and/or diagnostic (γ and β^+ radiation) applications. Bifunctional radionuclides or radioisotope pairs for both diagnostic and radiotherapy use are referred to as *theranostics*. Biological routes of inhaled microparticles can be followed by labeling them with PET diagnostic radionuclides.

Preparing radiometals for molecular labeling involves separation of ions from aqueous solutions, which requires the use of coordinating moieties known as chelators. Chelators acts as ligands that covalently link to targeted biomolecules in pharmaceutical studies, forming a radiopharmaceutical agent. Careful selection of a suitable chelator must be made in order to ensure minimal radiometal loss, which would otherwise result in an erroneous interpretation of PET images. Chelator-radiometal affinity is dependent on the coordination number of the chelator, the ionic charge of the radiometal, and a coordination geometry that matches the ionic radius of the metallic radioisotope as nicely as possible.[35]

Radiometals suitable for biological applications should present half-lives comparable to the targeted biomolecules under study. As an example, metallic radioisotopes used for the fate determination of inhaled particles in organisms should be trackable long enough so that a typical intake-to-excretion processing pathway could be observed. For this reason, gallium-68 and zirconium-89, with half lives of 67.629*(24)* minutes and 78.41*(12)* hours, respectively,[19] represent suitable imaging candidates for quantitative, sensitive, and non-invasive PET diagnostics.[35] Alternative non-metallic radionuclides suitable for PET tracking in biodistribution studies include bromine-76 or iodine-124, with relatively long half-lives of 16.2*(2)* hours and 4.1760*(3)* days.[19,36]

Gallium-68 is a widely used positron emitting radiometal in radiopharmaceutical chemistry for PET imaging purposes. It decays mainly via positron (β^+) emission with 88.0*(4)*% probability and positron energy of 1899.1 keV,[19] and its chemistry in aqueous form is dominated by its [^{68}Ga]Ga^{3+} oxidation state, with

a 62 pm ionic radius prone to forming octahedral six-coordination complexes providing the best *in vivo* stability.[9,10]

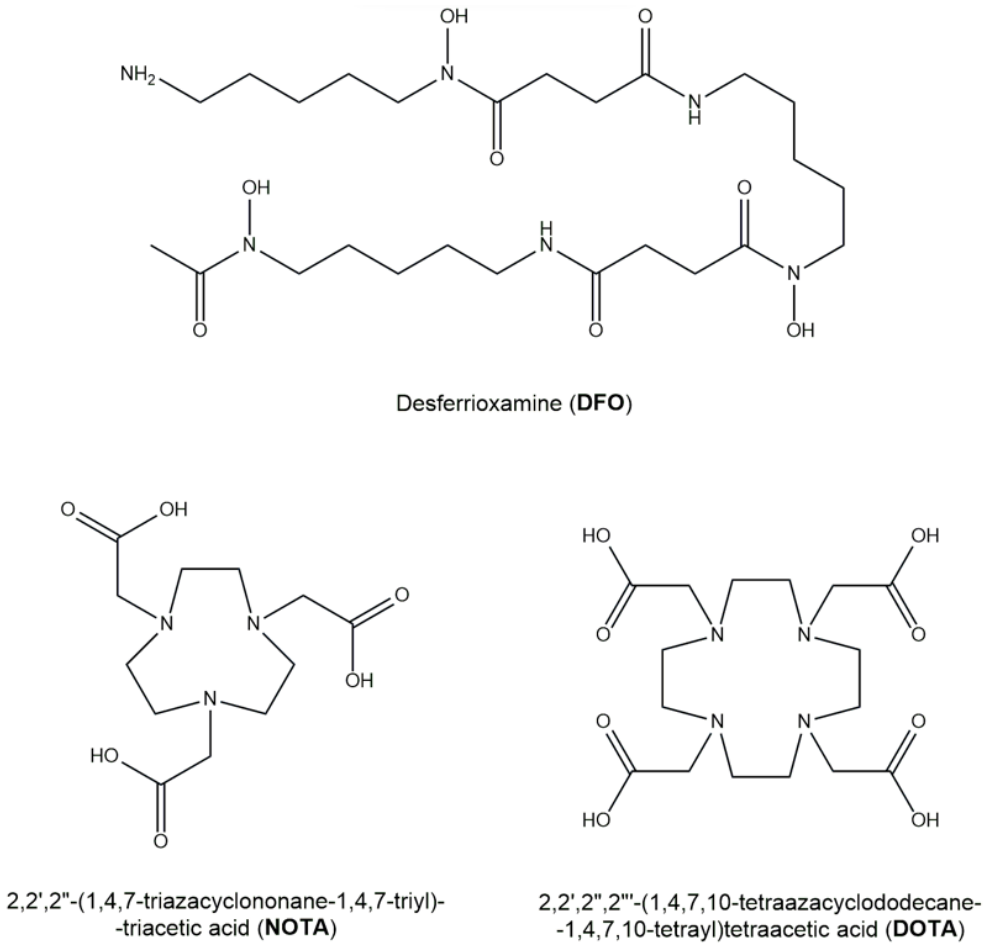

Figure 5. Chelator structures. Molecular structures of desferrioxamine (DFO), 2,2',2''-(1,4,7-triazacyclononane-1,4,7-triyl)triacetic acid (NOTA) and 2,2',2'',2'''-(1,4,7,10-tetraazacyclododecane-1,4,7,10-tetrayl)tetraacetic acid (DOTA).

Three possible matching chelators were initially proposed for [^{68}Ga]Ga^{3+} ion coordination to CsMPs, one of them with an acyclic structure based on desferrioxamine (DFO), and two of them macrocyclic. These were derived from the structures (**Figure 5**) of desferrioxamine (DFO) 2,2′,2”,2”'-(1,4,7,10-tetraazacyclododecane-1,4,7,10-tetrayl)tetraacetic acid (DOTA) and 2,2′,2”-(1,4,7-triazacyclononane-1,4,7-triyl)triacetic acid (NOTA), with radiometal to chelator affinity constants (log K_s) of 28.65, 26.05 and 29.63, respectively)[10].

Ultimately, chelator 2,2′-(7-(1-carboxy-4-((4-isothiocyanatobenzyl)amino)-4-oxobutyl)-1,4,7-triazonane-1,4-diyl)diacetic acid (*p*-NCS-Benzyl-NODAGA, **Figure 6**) derived from NOTA was chosen based on its high affinity constant value and accurately fitting cavity size of the NOTA moiety towards the radiometal ion.[37]

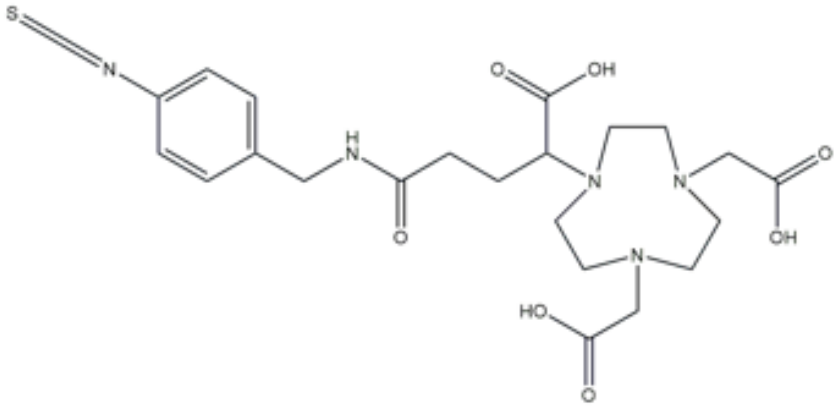

Figure 6. Chemical structure of p-SCN-Bn-NODAGA chelator. Full chemical name being 2,2′-(7-(1-carboxy-4-((4-isothiocyanatobenzyl)amino) -4-oxobutyl)-1,4,7-triazonane-1,4-diyl)diacetic acid.

Alternatively, zirconium-89 is another PET radionuclide which decays to yttrium-89m, a metastable isomer, via electron capture (EC) and positron emission with probabilities of 77% and 23%, respectively, with a positron emission energy of 902*(3)* keV. Yttrium-89m further decays to stable yttrium-89 emitting two 908.97*(3)* keV and 511 keV (annihilation) gamma rays.[19,38] It has been extensively used for the labeling of antibodies as its relatively long half-life matches the biological half-life of immunoglobulins.[11] It is present in aqueous form as a $[^{89}Zr]Zr^{4+}$ ion with 74–84 pm ionic radius with a tendency of forming octahedral six-coordination and dodecahedral eight-coordination complexes.[9,11]

Gallium-68 is most commonly obtained from a $^{68}Ge/^{68}Ga$ generator, in which the parent radionuclide germanium-68 is trapped in the sorbent matrix of a column. Gallium-68 can thereafter be eluted as $[^{68}Ga]GaCl_3$ with dilute hydrochloric acid while germanium-68 remains adhered into the solid phase matrix of the generator (usually based on TiO_2, SiO_2, CeO_2 or SnO_2). The use of $^{68}Ge/^{68}Ga$ generators is highly convenient as the long half-life of 270.8*(3)* days of germanium-68 guarantees a yearly sufficient gallium-68 production source.[19,39,40] Zirconium-89 is generally produced via proton irradiation (13–16 MeV beam energies) in a cyclotron, of a stable yttrium-89 target in a $^{89}Y(p,n)^{89}Zr$ reaction. Said target is then dissolved in HCl, followed by zirconium-89 entrapment in a hydroxamate-modified cation exchange resin and ultimate elution with oxalic acid.[41]

2.3.3 Radiofluorination chemistry

Fluorine-18 is a radioactive isotope of natural fluorine-19. It has a half-life of 109.77*(5)* minutes and decays to stable oxygen-18 mainly via positron emission, with a positron energy of 633.5 keV and 96.73*(4)*% emission probability. It can also decay via electron capture with a maximum radiation energy of 1655.5 keV and 3.27*(4)*% probability.[19] Its low positron energy provides excellent image resolution for PET imaging, whereas its relatively long half-life allows for the performance of synthetic multi-step transformations and later transportation to medical sites. Furthermore, it can be produced in house and in large quantities in an medical-based cyclotron, as well as it yields ^{18}F-labeled radiopharmaceuticals with very high molar activities that allow for microdosing.[15]

Radiofluorine is most commonly used as nucleophilic $[^{18}F]F^-$, which can be produced in cyclotron, linear accelerator, and nuclear reactors. The most widely extended production process is performed with a cyclotron by proton beam irradiation of enriched $[^{18}O]H_2O$ through the $^{18}O(p,n)^{18}F$ reaction. Obtained $[^{18}F]F^-$is then trapped in an ion-exchange chromatography column in order to separate it from H_2O, which deactivates its nucleophilic properties through solvation of the $[^{18}F]F^-$ ion and becomes eluted as [^{18}F]KF with acetonitrile (AcN) and a weak base such as K_2CO_3 or Cs_2CO_3. Potassium is then coordinated to a phase transfer catalyst like 4,7,13,16,21,24-Hexaoxa-1,10-diazabicyclo[8.8.8]hexacosane, commonly known as Kryptofix 2.2.2 (K222), which activates $[^{18}F]F^-$ for nucleophilic substitution. Finally, the AcN/H_2O media is evaporated via azeotropic distillation and $[^{18}F]F^-$can readily be used in synthetic steps for radiopharmaceutical preparation.[16]

The most widely used method for the incorporation of fluorine-18 into molecules is through the substitution of already present hydroxyl (OH) groups. The similar Van der Waals radius of fluorine (1.47 Å) and hydrogen (1.20 Å) diminishes steric hinderance problems, as well as the capability of fluorine of forming hydrogen bonds. This makes fluorine-18 an excellent candidate for hydroxyl group substitution of targeted molecules. Even though this strategy will always imply lipophilicity, BD, PD and PK alteration of the radiopharmaceutical versus the original molecule, undesired effects will be mitigated.[15,16]

Fluorine-18 can react both as a nucleophile ($[^{18}F]F^-$) through nucleophilic substitution reactions via S_N2 and S_NAr mechanisms, and as an electrophile ($[^{18}F]F^+$), mainly through S_EAr reactions. Nucleophilic radiofluorination normally involves the ejection of large, polarized leaving groups, like tosylates and mesylates in aliphatic substitutions, and $-Ar^+I^-$, $-NEt_3$, $-NO_2$ groups in aromatic. In S_NAr reactions, the insertion position of the fluorine group must be activated with electron withdrawing groups (EWG) like carbonyl or nitro, localized in *ortho* or *para* positions in the aromatic ring. On the other hand, S_EAr reactions preferably take place through ^{18}F-fluorodemetallation mechanisms that promote $-SnR_3$, Ag or $-GeR_3$ as optimum leaving groups. In this case, the substitution position of the aromatic ring must be previously activated with electron donating groups (EDG), such as hydroxyl or amines, through *ortho/para* directing effects.[42,43]

According to the silica-based matrix of the synthetic glass microparticles used in this study, direct radiofluorination could be achieved by creation of a new Si-^{18}F bond. Silicon-fluoride chemistry has been widely studied, due to the increased strength of the Si-F bond with respect to that of C-F, with bond energies of 480 and 570 kJ/mol, respectively. However, the main inconvenience of this method is the high tendency of the Si-^{18}F bond to undergo hydrolysis in physiological media. This is extremely inconvenient for *in vivo* studies, which has led to the development of Silicon Fluoride Acceptors (SiFAs). Such approach is based in the design of stable Si-^{19}F compounds, which can achieved with the use of large substituents onto the Si atom (like *tert*-butyl or aryl groups), that prevent the hydrolysis of Si-F through steric hindrance. After SiFA-based pharmaceuticals have been synthesized, ^{18}F can be easily introduced through isotopic exchange with the already present ^{19}F atom. Unfortunately, the high hydrophobicity of these moieties gives place to very lipophilic radiotracers that are likely to accumulate in the liver, which is highly undesired.[17]

Nevertheless, direct radiofluorination onto the surface of the glass particles is still possible, and furthermore, silanol groups, which are already present in the surface of the glass microparticles, have already proved to be decent radiolabeling precursors. Therefore the main challenge of this approach would be to evaluate the stability of the formed $[^{18}F]$Si-^{18}F bond over time and/or in biological media.[17]

2.3.4 Surface modification of borosilicate samples

Conventional glass particles are composed of silica and metal oxide traces in different compositions. Normally, these are structurally arranged exposing their silanol (Si-OH) groups on their surface.[12] According to conventional radiometal-chelator chemical procedures, hydroxyl group reactive chelators attachable onto the glass surfaces could have been used for radiometal coordination, but this could result in extreme surface functionalization of the sample, which is highly undesired for biodistribution studies.

Surface alteration of materials has been widely employed throughout the years to obtain modified samples derived for different purposes. Borosilicate glasses have been previously proven to be successfully amine-end functionalized with (3-amino-propyl)triethoxysilane (APTES) through a silanization reaction.[12,13,44–46] It has been demonstrated that the thickness of the grafted organosilane compound is dependent on substrate chemistry and reaction conditions, like time and temperature.[47] Attachment of macrochelators can then be easily achieved through reaction with the exposed free amine ends.

Activation of the superficial silanol groups of the glass microparticles must be performed prior to any surface modification processes. This can be achieved using acidic or basic conditions, like immersion in piranha solution (H_2O_2:H_2SO_4 (1:3 (v/v)), in HNO_3, in NaOH or in HCl. Although different performances have been reported along literature, NaOH and HCl activation seem to provide best activation results of borosilicate glass matrixes.[14,48]

Silanization and subsequent amine functionalization with APTES takes place through a condensation mechanism where the reagent bonds to free silanol groups at the surface of glass particles. Nevertheless, in order for this reaction to take place, APTES must previously hydrolyze its ethoxy groups, which can be easily achieved under presence of low amounts of water (e.g. using EtOH 95% as a solvent). On the other hand, this process should be controlled as its hydrolyzed derivative, (3-Aminopropyl)silanetriol, can easily undergo self-polycondensation forming a polymeric gel network either unavailable for surface grafting, or providing bulky moieties that could greatly modify the surface of the particles and therefore impact their natural biodistribution studies (**Figure 7**). For these reasons, water content,

reaction temperature and process time of the grafting reaction must be previously optimized or fitted to reference values. Furthermore, silanization cannot be performed in normal glass flasks as their chemical composition is similar to that of the studied microparticles and therefore, their functionalization could in turn be unspecific.[49]

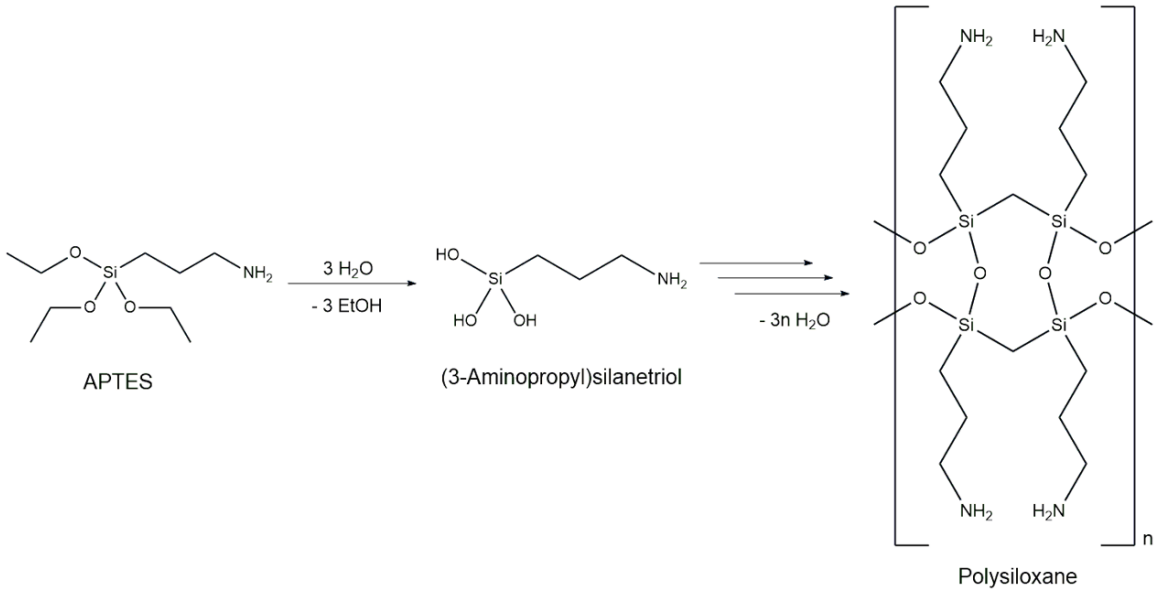

Figure 7. APTES hydrolysis and self-polycondensation. Reaction overview and final suggested gel network.[49]

APTES grafting of glass surfaces has experimentally shown to take place forming isolated and non-uniform regions along the spherical microparticles. An alternative, homogeneous, amine-end surface functionalization method has also provided great results using ethanolamine hydrochloride as a silanization reagent. Due to the short length of the ethanolamine molecule, a secondary NHS-PEG$_n$-COOH moiety has to be priorly attached to the free amine groups before radiometal chelator insertion, in order to prevent an excessive blocking of the studied samples. The macrochelator of choice would then be inserted into the prepared system through a reaction with the free carboxylic acid ends of the polymeric linker.[14,50] Comparisons between isolated and homogeneous glass particle functionalization have not been made yet regarding biological distribution upon inhalation studies.

3 Experimental procedures

The experimental part of this thesis work was directed towards the radiolabeling of synthetic borosilicate glass particles with positron-emitting radionuclides like gallium-68. This was based in the surface modification of the synthetic microparticles with a grafting agent presenting reactive amine end. Amine groups were needed as linkers for the subsequent grafting of chelator structures capable of coordinating $[^{68}Ga]Ga^{3+}$. Alternative functionalization strategies were also tested to address potential differences between grafting agents. Direct radiofluorination of the borosilicates was also considered for as a possible radiolabeling strategy.

3.1 Materials

All materials and solvents used along this project were purchased from Merck Life Science (St. Louis, Missouri, USA) unless stated otherwise. Ethanolamine hydrochloride was provided by TCI (Tokyo, Japan). NHS-PEG_5-$COOH_{MW435.4}$ was purchased from BroadPharm (San Diego, California, USA). p-SCN-Bn-DFO was purchased from Macrocyclics (Plano, Texas, USA). p-SCN-Bn-NODAGA was purchased from CheMatech (Dijon, France). Simulated lung fluid (SLF) used in stability assays was provided by internal collaborators. Plasma was acquired from a human donor (FFP 24) from the Finnish Red Cross Service (Helsinki, Finland) with an ethical approval for research purposes. Lo-Bind 1.5 mL Eppendorf tubes were obtained from Eppendorf (Hamburg, Germany). Chromatography sheets impregnated with silicic acid (SA) and silica gel (SG) were purchased from Agilent Technologies (Santa Clara, California, USA).

Metal trace-free Chelex H_2O was used when handling chelators to prevent the coordination of undesired metallic impurities. It was prepared in house by incubation of Chelex resin (10 g) obtained from Merk Life Science (St. Louis, Missouri, USA) with deionized H_2O (2 L), and filtration after 24 hours.

Spherical and white powder-like synthetic borosilicate microparticles were purchased from Thermoscientific (Waltham, Massachusetts, USA) in a 2.2 ± 0.3 μm diameter. Chemical composition by weight was of 52.5% SiO_2, 22.5% CaO, 14.5% Al_2O_3, 8.6% B_2O_3, 1.2% MgO, 0.3% Na_2O, 0.2% FeO/Fe_2O_3, and 0.2% K_2O, which agrees with that described as for the matrix of observed FDNPP-originated type A CsMPs.

Additional properties of these synthetic microparticles were a Young Modulus of 10.5 × 10^6 psi, hardness of 6.5 Moh, dielectric constant of 5.8 × 10^6 Hz at 22ºC, and softening point of 846 ºC. According to the manufacturer, composition and properties of the material have been estimated and should not be used as calibration values.

A different set of borosilicate particles with a 44-µm estimated diameter size, custom designed by MO-SCI (Rolla, Missouri, USA), was also subjected for functionalization. Chemical composition by weight ranged among 75-85% SiO_2, 12-16% B_2O_3, 2-6% Na_2O and 2-5% Al_2O_3. Intrinsic particle properties were a specific gravity value of 2.2 g/cm^3, a bulk density of 1.2 g/cm^3 with respect to the dry material, refraction index of 1.47-1.47, a coefficient of thermal expansion of 32 × 10^{-7} ºC^{-1} within a 30-300 ºC temperature range, and a softening temperature of 830 ± 10 ºC.

The instrumentation IRTracer-100 from Shimadzu (San Jose, California, USA). Zetasizer Nano ZS and DTS1070 cuvettes were from Malvern Panalytical (Malvern, United Kingdom). STA 449 F3 Jupiter was from NETZSCH Analyzing & Testing (Selb, Germany). Vario microcube elemental analyzer was from Elementar (Langenselbold, Germany). Argus photoelectron energy analyzer was from Scienta Omicron (Uppsala, Sweden and Taunusstein, Germany).

All materials and instruments can be found recorded along **Table 1** for an easier visualization.

Table 1. Materials and instruments used along this thesis. Specification of provider, city and country.

Material, instrument or chemical compound	Provider	Location
All chemicals and solvents *(unless stated otherwise)*	Merck Life Sciences	St. Louis, Missouri, USA
Ethanolamine hydrochloride	TCI	Tokyo, Japan
NHS-PEG_5-$COOH_{MW435.4}$	BroadPharm	San Diego, California, USA
p-SCN-Bn-DFO	Macrocyclics	Plano, Texas, USA
p-SCN-Bn-NODAGA	CheMatech	Dijon, France
Human plasma	Finnish Red Cross Service	Helsinki, Finland
Lo-Bind Eppendorf 1.5 mL tubes	Eppendorf	Hamburg, Germany
2.2-µm borosilicate microparticles	Thermoscientific	Whaltman, Massachusetts, USA
44-µm borosilicate microparticles	MO-SCI	Rolla, Missouri, USA
IRTracer-100	Shimadzu	San Jose, California, USA
Zetasizer Nano ZS, DTS 1070 cuvette	Malvern Panalytical	Malvern, United Kingdom
STA 449 F3 Jupiter	NETZSCH Analyzing & Testing	Selb, Germany

Material, instrument or chemical compound	Provider	Location
Argus photoelectron energy analyzer	Scienta Omicron	Uppsala, Sweden/Taunusstein, Germany
Vario MICRO cube elemental analyzer	Elementar	Langenselbold, Germany
Fuji FLA 5100, Fuji BAS-TR2025	Raytek Scientific Limited	Sheffield, United Kingdom
SA and SG impregnated chromatograhy sheets	Agilent Technologies	Santa Clara, California, USA

Continuation of **Table 1**.

3.2 Surface modification of borosilicate microparticles

3.2.1 Surface silanol activation of borosilicate microparticles

Silanol groups present in the surface of the 44-µm and 2.2-µm glass microparticles were initially activated by either acid or basic washing prior further modifications.[14,48]

- HCl cleaning Superficial silanol groups were activated by immersion of the synthetic microparticles in 10% HCl for 2 hours at 90 ºC under constant stirring. Acidic supernatant was then removed upon sedimentation of the microparticles by centrifugation (3 minutes, 4 ºC, 14000 rpm). The microparticles were finally washed three times with deionized H_2O in an ultrasonic bath (5 minutes, room temperature) followed by centrifugation (3 minutes, 14000 rpm). Particles were left to dry for 24 hours at 100 ºC in an oven.

- NaOH cleaning. Particles were incubated in NaOH solution (2 M) for 24 hours at room temperature under constant stirring. Supernatant was then removed upon sedimentation in a centrifuge (3 minutes, 4 ºC, 14000 rpm). Particles were washed three times with deionized H_2O in an ultrasonic bath (5 minutes, room temperature) followed by centrifugation (3 minutes, 14000 rpm). Particles were dried for 24 hours at 100 ºC in an oven.

3.2.2 Superficial functionalization of borosilicate microparticles with APTES

The superficial functionalization of the glass microparticles was achieved using APTES as a silanization agent, following a two-step procedure as illustrated along **Figure 8**. Concentrations of the APTES solutions used along these functionalization

procedures were of 2 mM for the 2.2-µm microparticles; and of 0.5 mM, 1 mM, 2 mM, 5 mM and 10 mM for the 44-µm microparticles.[12,13]

1) Washing step. Activated synthetic borosilicate glass particles (about 10 mg) were cleaned first one time with 95% acetone and then two times with deionized H_2O in an ultrasonic bath (5 minutes, room temperature) followed by centrifugation (3 minutes, 4 ºC, 14000 rpm), in order to ensure the proper superficial hydrolyzation of the glass microparticles prior functionalization. Particles were then left to dry in an oven for 1 hour at 100 ºC to remove possibly remaining solvent.

2) Grafting step. Silanization of the activated microparticles was achieved through incubation in an APTES solution in 95% EtOH. The reaction was to recur in a revolver tube rotator for 24 hours at room temperature. A final washing step to remove unbound excess of reagent was performed three times with 95% EtOH on the dry sample in an ultrasonic bath (5 minutes, room temperature) followed by centrifugation (3 minutes, 4 ºC, 14000 rpm). Samples were finally set to dry in an oven for 24 hours at 100 ºC for consolidation of the bond between the grafted molecules and the surface of the glass microparticles.

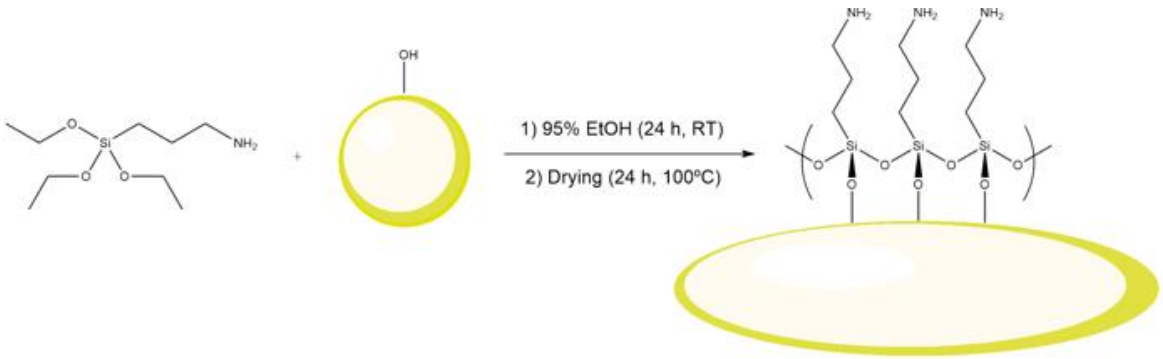

Figure 8. Functionalization of borosilicates with APTES. Representation of the followed reaction pathway. The surface of the glass particles is represented in yellow.[12,13]

3.2.3 Conjugation of p-SCN-Bn-DFO onto APTES functionalized borosilicate microparticles

p-SCN-Bn-DFO (752.9 g/mol) chelator was conjugated to APTES (2 mM) functionalized borosilicate particles, according to the next described reaction scheme (**Figure 9**) and steps. Only 2.2-µm microparticles were functionalized with *p*-SCN-Bn-DFO:

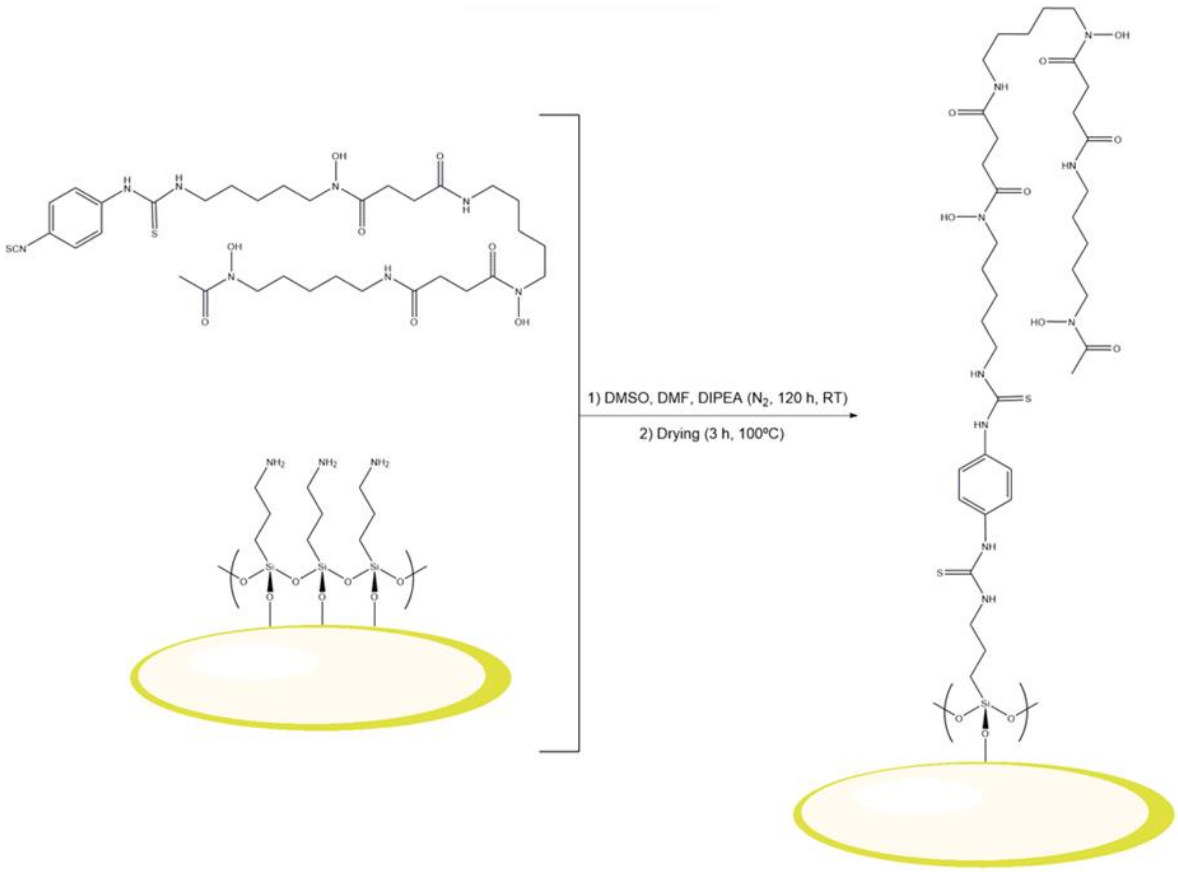

Figure 9. Reaction of p-NCS-Benzyl-DFO chelator with APTES functionalized borosilicate. Synthetic reaction scheme representation. Yellow curve represents the surface of the original borosilicate particle.

1) Functionalization. APTES functionalized borosilicate particles (1.0 mg) were dissolved in DMF (50 µL). A mixture of *p*-SCN-Bn-DFO (2.0 mg, 0.0026 mmol, 1 eq) and DIPEA (2 µL, 0.013 mmol, 5 eq) dissolved in DMSO (150 µL) was added drop by drop to the solution containing the borosilicates. Reaction took place under inert N_2 atmosphere and proceeded for 120 hours at room temperature under constant stirring.

2) Washing. Solvent excess was removed after reaction completion upon sedimentation of the microparticles by centrifugation (3 minutes, 4 ºC, 14000 rpm). The functionalized product was cleaned three times with Chelex H_2O in an ultrasonic bath (5 minutes, room temperature) followed by centrifugation (3 minutes, 4 ºC, 14000 rpm). Particles were then left to dry in an oven for 3 hours at 100 ºC.

3.2.4 Conjugation of *p*-SCN-Bn-NODAGA onto APTES functionalized borosilicate microparticles

APTES (2 mM) functionalized borosilicate particles were further conjugated to *p*-NCS-Benzyl-NODAGA (593.15 g/mol) chelator for the coordination of $[^{68}Ga]Ga^{3+}$ ions. The ultimate election of *p*-NCS-Bn-NODAGA was based on the excellent size matching of the chelator cavity with the ionic radius of $[^{68}Ga]Ga^{3+}$, which allows for the formation of an stable octahedral six-coordinate complex. Chelator conjugation of the 44-µm and 2.2-µm borosilicates was performed under different reaction conditions.

The reaction scheme for the functionalization of the 44-µm microparticles can be found along **Figure 10**, consisting of the following steps:[51]

1) Functionalization. APTES-functionalized borosilicate particles (5.0 mg) were mixed with *p*-NCS-Bn-NODAGA (10.0 mg, 0.0017 mmol) dissolved in anhydrous DMF (2 mL). Addition of triethylamine (12 µL, 0.09 mmol) was added dropwise and under constant stirring to the borosilicate solution. Reaction proceeded for 20 hours at room temperature and under ambient atmosphere under constant stirring.

2) Washing. Solvent was removed after reaction completion upon sedimentation of the microparticles by centrifugation (3 minutes, 4 ºC, 14000 rpm). The functionalized product was washed three times with metal trace free Chelex H_2O in an ultrasonic bath (5 minutes, room temperature) followed by centrifugation (3 minutes, 4 ºC, 14000 rpm). Particles were then left to dry in an oven for 3 hours at 100 ºC.

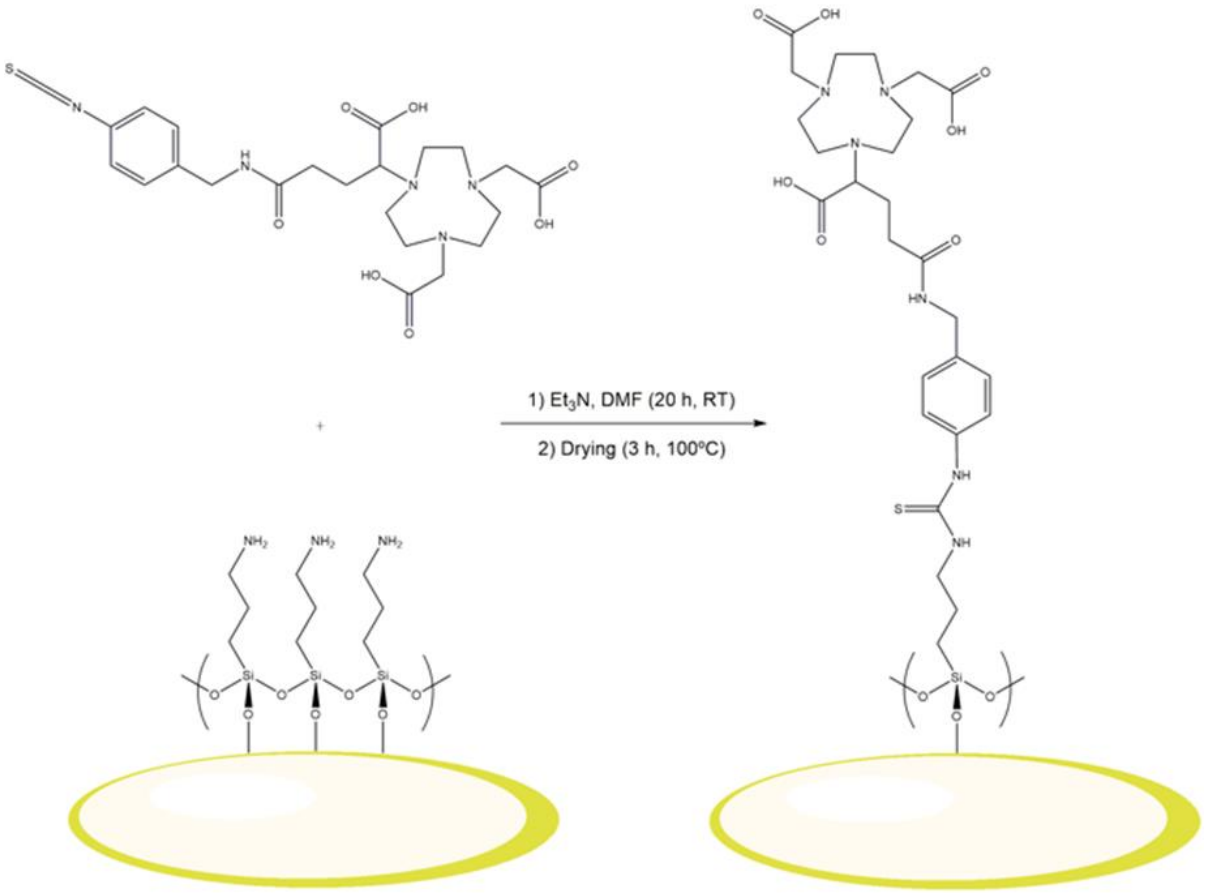

Figure 10. *p*-NCS-Benzyl-NODAGA chelation of APTES functionalized borosilicate. Synthetic reaction scheme representation. Yellow curve represents the surface of the original borosilicate particle.

Simultaneously, the different reaction conditions followed with the 2.2 µm microparticles are shown in **Figure 11**. These consisted on the following steps:

1) Functionalization. APTES-functionalized borosilicate particles (7.0 mg) were dissolved in DMF (500 µL). A mixture of *p*-NCS-Bn-NODAGA (10.0 mg, 0.0017 mmol, 1 eq), DMSO (500 µL) and DIPEA (14.68 µL, 0.0066 mmol, 5 eq) was added dropwise and under constant stirring to the borosilicate solution. Reaction took place in an inert N_2 atmosphere and proceeded for 72 hours at 25 ºC under constant stirring. This reaction was always performed satisfying a (1:1.4-1.6) mass relationship between borosilicate and chelator, respectively.

2) Washing. Solvent excess was removed by centrifugation (3 minutes, 4 ºC, 14000 rpm). The functionalized product was cleaned three times with Chelex H_2O in an ultrasonic bath (5 minutes, room temperature) followed by centrifugation (3 minutes, 4 ºC, 14000 rpm). Particles were then dried in an oven for 3 hours at 100 ºC.

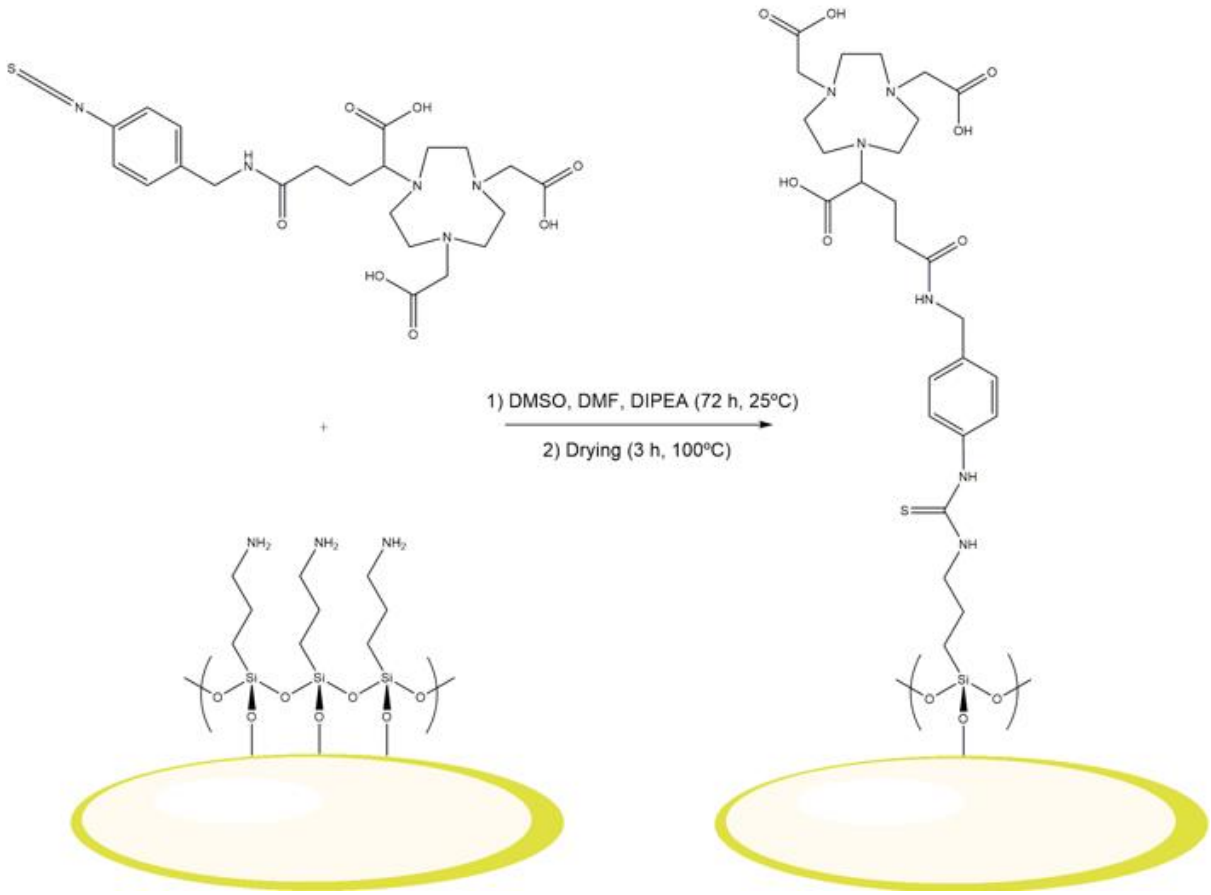

Figure 11. p-NCS-Benzyl-NODAGA chelation of APTES functionalized borosilicate. Synthetic reaction scheme representation. Yellow curve represents the surface of the original borosilicate particle.

3.2.5 Functionalization of borosilicates with ethanolamine hydrochloride

The superficial functionalization of the glass microparticles is performed following a two-step procedure as can be seen in **Figure 12**. Only the 2.2-µm microparticles were functionalized with ethanolamine hydrochloride:[14,50]

1) Washing step. Synthetic borosilicate glasses (10.4 mg) were initially cleaned with 95% acetone in an ultrasonic bath followed by centrifugation. The glass particles were then rinsed in an ultrasonic bath (5 minutes, room temperature) with deionized H_2O three times, supernatant being removed upon centrifugation (3 minutes, 4 °C, 14000 rpm). Particles were then left to dry in an oven for 1 h at 100 °C to remove possibly remaining solvent.

2) Grafting step. Amine-end functionalization of the borosilicate was achieved by incubation of the glass microparticles in 6.6 mL of a 5 M ethanolamine hydrochloride solution in DMSO. The reaction takes place in a heating block with integrated mixing (24 hours, 25 °C, constant stirring). Three washing steps

were with DMSO were performed on the particles by activation in an ultrasonic bath (5 minutes, room temperature) and solvent removal by centrifugation (3 minutes, 22 ºC, 7000 rpm). Three more washing steps were performed with EtOH absolute, by activation in an ultrasonic bath (5 minutes, room temperature) and solvent removal by centrifugation (3 minutes, 4 ºC, 7000 rpm). Samples were finally set to dry in an oven for 24 hours at 100 ºC.

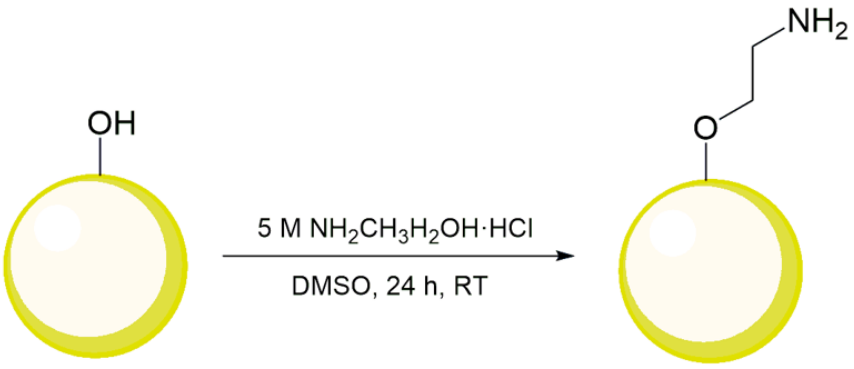

Figure 12. Functionalization of borosilicates with ethanolamine hydrochloride. Synthetic reaction scheme representation. Functionalized product is represented according to [Janissen et al., 2009].[14]

3.2.6 PEG functionalization of ethanolamine surface modified borosilicates

Ethanolamine functionalized particles were then subjected to further modification via the conjugation of a NHS-PEG_5-$COOHMW_{435.4}$ linker, as described along **Figure 13** in reference to literature:[14]

1) Reaction. Previously prepared Ethanolamine-functionalized borosilicate particles (10.4 mg) were incubated in a NHS-PEG_5-COOH solution (1 mL, 2 mM) in anhydrous $CHCl_3$ with Et3N (0.5% (v/v)). Reaction took place in a revolver tube rotator (24 hours, room temperature).

2) Washing step. Solvent was removed by centrifugation (3 minutes, 4 ºC, 14000 rpm). Three washing steps were then performed with deionized H_2O on the particles consisting of activation in an ultrasonic bath (5 minutes, room temperature) and solvent removal by centrifugation (3 minutes, 4 ºC, 14000 rpm). Particles were left to dry (3 hours, 100ºC).

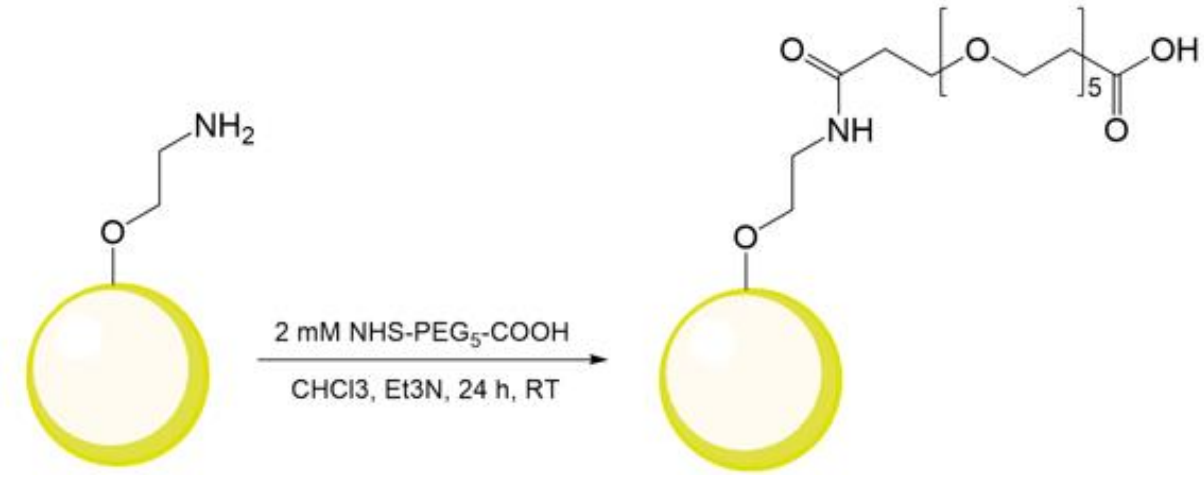

Figure 13. Polymer linker insertion into Ethanolamine-functionalized borosilicate particles. Synthetic reaction scheme representation. Glass particles are represented with a brown colour.

3.2.7 DFO conjugation to PEG-Ethanolamine functionalized borosilicate microparticles

Formerly obtained PEG-Ethanolamine functionalized borosilicate particles were further functionalized with DFO mesylate salt (656.8 g/mol). The followed reaction scheme can be found along **Figure 14**, consisting of the following steps:

1) Functionalization. PEG-Ethanolamine functionalized borosilicate particles (3.0 mg), DFO mesylate salt (5.0 mg, 0.007 mmol, 2 eq) and EDC hydrochloride (2.1 mg, 0.011 mmol, 3 eq) were dissolved in DMF (600 µL) at 45ºC. After dissolution of the reagents, reaction took place in an inert N_2 atmosphere (120 hours, room temperature, constant stirring).

2) Washing. Solvent was removed after reaction completion upon sedimentation of the microparticles by centrifugation (3 minutes, 4 ºC, 14000 rpm). The functionalized product was cleaned three times with Chelex H_2O in an ultrasonic bath (5 minutes, room temperature) followed by centrifugation (3 minutes, 4 ºC, 14000 rpm). Particles were then left to dry in an oven for 3 hours at 100 ºC.

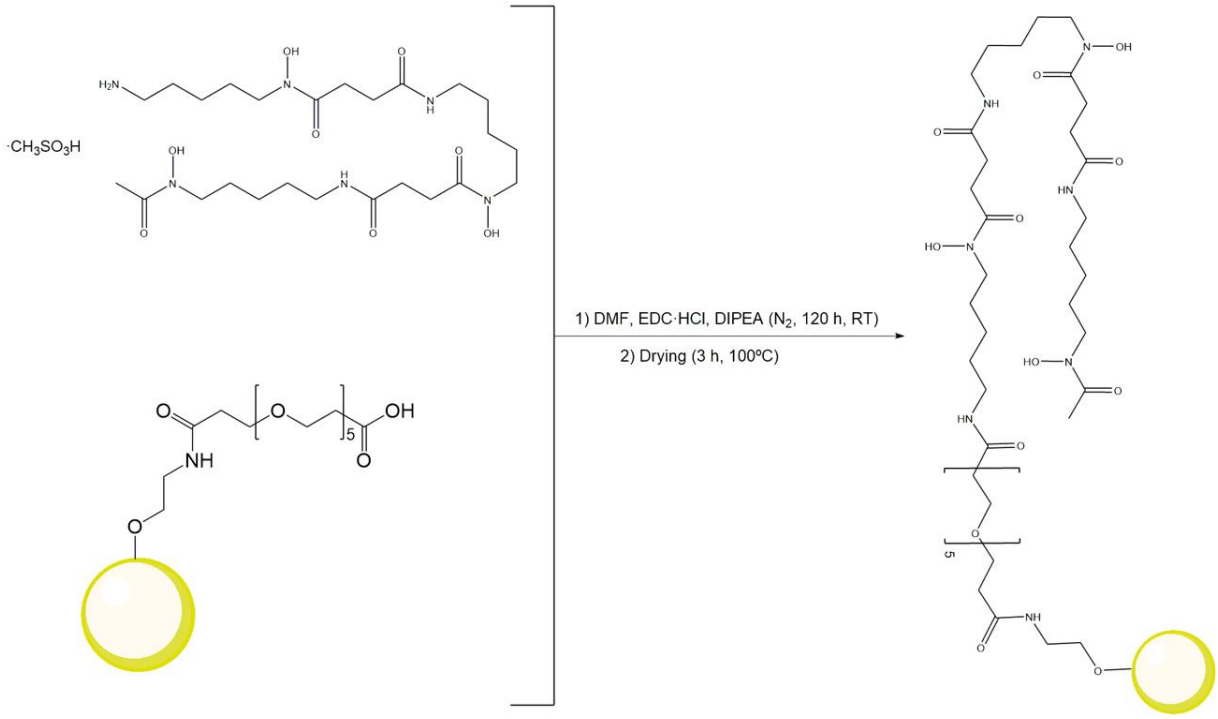

Figure 14. Conjugation of DFO mesylate salt to PEG-Ethanolamine functionalized borosilicate. Synthetic reaction scheme representation. Glass particles are represented with a brown colour.

3.3 Characterization methods

A wide variety of analytical techniques was used for the characterization of surface functionalization in the different borosilicate samples prepared.

3.3.1 Fourier Transform Infrared Spectroscopy (FTIR)

FITR is a widely used and reliable technique that allows for the characterization of samples under irradiation with infrared light (IR). Upon exposure to IR radiation, samples absorb a fraction of the incident radiation while the remaining amount becomes transmitted, defining characteristic percentages. Absorbed radiation is employed for bond vibration or angle deformation based on analyte structure, which gives place to the fingerprint spectra of the studied material.[52]

Fourier Transform Infrared Spectroscopy (FTIR) is a spectroscopy method based in the irradiation of a sample with infrared light through a system composed of at least an IR source, two mirrors (fixed and mobile), a beam splitter and a detector.[52] This system is referred to as a Michelson interferometer able of providing an interferogram whose maxima obey equation (2):

$$m\lambda = 2nd \cdot cos\theta \qquad (2)$$

where λ is the wavelength of the incident radiation, d is the distance between fixed and mobile mirrors with respect to the beam splitter, n is the environmental refractive index (generally n=1 is considered) and θ is the angle between incident and reflected radiation. The acronym m, which is dependent on d, is a value to which the studied maximum is generally associated. Obtained IR spectra are obtained after calculation of the Fourier transformation on the obtained interferogram.[53]

The characterization of the synthetised samples was done with an ATR (Attenuated Total Reflection) FTIR spectrometer that allows for the direct analysis of solid samples, minimizing sample recuperation as well as humidity absorption interferences associated to the conventional IR spectrometry with KBr tablet preparations.[54]

FTIR spectra were obtained with a IRTracer-100 consisting of a diamond sample holder and an auxiliar point for pressure application on the sample. Spectra were obtained among 4000-600 cm^{-1} with a 4 cm^{-1} resolution and background corrections were applied.

3.3.2 Zeta potential

Zeta potential is a measure of the electrostatic attraction or repulsion experienced upon interaction of particles with a fluid. It is mainly used for the prediction of particle behaviour and stability, as well as associated interactions.[55–57]

When a polar liquid like water interacts with an electrically charged surface, a difference in potential can be observed at their interface due to dipole orientation. There are two defined regions between particle and fluid, which are referred to as inner or Stern, and outer or diffuse layers. In the inner region, ions strongly bind to the surface of the charged particles, whereas this interaction is weaker in the outer layers. An stable moiety is formed within a range of the outer layer, and the potential measured at its surface is called zeta potential.[55,57]

Zeta potential provides information about the stability and dispersive behaviour of particles, since high positive or negative potentials (-30 mV to +30 mV) imply that the repulsion experienced between them will be strong enough to prevent their aggregation. Zeta potential depends on different parameters such as pH, compound concentration and conductivity of the solution. The isoelectric point of a solution is

recorded as the pH value where zeta potential is of 0 mV, and it theoretically corresponds to the point where electrostatic repulsion is the lowest possible.[55]

Measured zeta potential values provide an estimation of superficial electrostatic charge. If negative potentials are recorded, it is deduced that particles are negatively charged, and H_3O^+ species and cations will be found surrounding the inner and outer layers. This can directly provide information about the chemical composition of particles at their surface.[55]

Surface zeta potential of the 2.2-µm microparticles was recorded by dispersion of the microparticles (~0.5 mg) in deionized H_2O (1.5 mL). Solutions were injected in a zeta potential DTS1070 cuvette with a 1 mL syringe. Experiments were conducted at 25°C in a Zetasizer Nano ZS from Malvern Panalytical (Malvern, United Kingdom). Equilibrium time before starting of the experiments was of 120 seconds. Measurements were performed in triplicate with a minimum to maximum number of scans of 20 to 100, respectively.

44-µm borosilicates were not measured under zeta potential since they undergo precipitation in H_2O due to their large size. Only measurement of 2.2-µm functionalized borosilicates under zeta potential was possible thanks to their dispersity in H_2O, possibly thanks to their smaller particle size.

3.3.3 Thermogravimetric Analysis (TGA)

Thermogravimetric analysis is a technique used in the evaluation of weight variations upon temperature increase. TGA instrumentation is composed by a thermally isolated scale placed inside a furnace. Measurements can be done under controlled gas flow or vacuum.[58,59]

In TGA, sample weight is constantly monitored, and data acquisition is obtained upon application of a temperature program. Measuring atmosphere is controlled with a purge gas. TGA can provide information about sample composition and moisture adsorption based on detectable mass shifts.[58,59]

Measurements were performed in an STA 449 F3 Jupiter equipment compatible with a wide range of materials and non-homogeneous samples. Sample weight was of about 3-4 mg per evaluation. Minimal amount of recommended sample was of about

10 mg, and deviations related to the analysis of lower amounts should be acknowledged. [60]

44-µm borosilicates were measured in a dynamic heating program at 25–800°C (10 °C/min), whereas 2.2-µm particles were subjected to a dynamic heating program at 25–1000 °C (40 °C/min). Gas flow during the experiments was of 20 mL/min for purge 1 (air 80/20), purge 2 (nitrogen) and protective mass flow controller. Measurements were recorded by the NETZSCH Proteus Thermal analyzer. Weight was calibrated to 100% for all samples.

3.3.4 Scanning Electron Microscopy (SEM)

SEM is a technique used to obtain of high-resolution images. It is based in a superficial scanning of samples with a thin electron beam. Incident electrons interact with superficial atoms for the generation of signals providing information about sample geometry. SEM resolution is usually in the nanometre range.[61–63]

Possible signals born from incident electron beam and sample interaction include secondary electrons, backscattered electrons, or photons, among other. Image acquisition is made possible thanks to the first two mentioned interactions. Secondary electron interaction provides information about sample morphology and topography, whereas backscattered electrons are responsible for image contrasts.[61–63]

Borosilicate samples (~0.5 mg) were dispersed in deionized H_2O and mixed in vortex. An aliquot (10 µL) was spotted on carbon tape placed on top of a metallic holder. Samples were let to dry for about 24 hours and then carbon coated for better conductivity. Carbon coating was of 10 and 20 nm for 44-µm and 2.2-µm microparticles, respectively.

3.3.5 Energy Dispersive Spectroscopy (EDS)

EDS is a microanalytical technique used for the quantification of the elemental composition of a sample. EDS is usually performed alongside SEM or TEM. EDS is based on the interpretation of emitted X-rays upon exposure to a light ion beam. Emitted X-rays are characteristic for every element, which allows for the determination of sample composition.[64]

X-ray detection is achieved with help of a silicon drift detector. Identification is then further assessed with an associated software.[64] Samples evaluated under SEM/EDS must be stable at low vacuum conditions. Normally EDS detectors are not capable of detecting lighter elements like hydrogen. The lower sensitivity of EDS equipment limits the detection of elements present in lower concentrations.[62]

Sample preparation was identical for both SEM and EDS techniques as measurements were performed with the same instrumentation. EDS measurements were always performed in cooperation with SEM.

3.3.6 Elemental analysis

Elemental analysis is a technique based on the determination of sample composition upon combustion in a furnace. Samples are placed in a crucible placed on top of a combustion tube filled with WO_3 that acts as a catalyst in the delivery of oxygen used in the combustion process. The combustion tube is heated up to 1150 °C under oxygen administration for the formation of oxygenated gaseous compounds. Gases are then transferred to a reduction tube at 850 °C where SO_3 is reduced to SO_2 and nitrogen oxides to N_2.[65]

In elemental analysis, carbon, hydrogen, nitrogen, and sulphur are determined as CO_2, H_2O, N_2 and SO_2. CO_2, H_2O and SO_2 gas are desorbed from an adsorption column at 60°C, 140 °C, and 210 °C and transferred to a thermal conductivity detector (TCD) where they become measured. Nitrogen does not become adsorbed into any columns as it is already directed to the TCD. Elemental concentrations are calculated according to equation (3):

$$Elemental\ concentration\ (\%) = \frac{Absolute\ element\ content \cdot f}{Weight} 100 \qquad (3)$$

Where f is the daily factor used for calibration of the instrument with respect to the measured elements.[65]

Elemental analysis results were obtained with a vario MICRO cube elemental analyzer. About a total of 0.5–6.0 mg of sample was analyzed. Minimum amount requested by the operator was of 2.0 mg, which could not be collected in some cases and should therefore be considered as a source of deviations. Measurements were performed in triplicate in CHNS mode with the method Graphite120s.

3.3.7 X-Ray Photoelectron Spectroscopy (XPS)

XPS is a very sensitive technique used for the analysis of material surfaces. It is based in the superficial excitation of materials with a mono energetic X-ray source responsible for the emission of superficial photoelectrons. The energy of the emitted photoelectrons is measured with an electron energy analyzer. Average measurement depth of XPS instruments is of 5 nm. Understanding of XPS results provides information about chemical disposition and bonding in surfaces.[66,67]

Photoelectron emission is based in the emission of electrons upon irradiation with photons. Emission takes place if the energy of the incident beam is higher than their binding energy along the material. XPS measured the kinetic energy of the emitted photons, which is proportional of their binding energy. This obeys equation (4):

$$E_{kinetic} = E_{photon\ (hv)} - E_{binding} - \varphi \qquad (4)$$

Where φ is a work function equal to the difference inner between vacuum energy and the Fermi levels of a solid.[67]

Powder samples are not usually typical in XPS analysis. Immobilization must take place to prevent obstruction of the instrument. Kapton® film was the preferred adhesive for XPS due to its stability under high vacuum conditions.

Samples were prepared by immobilization of borosilicate particles (~0.5 mg) in a Kapton polyimide film coated with an adhesive silicone cured layer. Samples were then covered with an aluminium foil for immobilization of the Kapton tape and placed in a sample holder of approximately 1 cm x 1 cm dimensions. Unbounded excess from the aluminium cover was removed with ethanol if considered necessary.

XPS measurements were performed in an XPS instrument from Hidden Analytical Ltd. Data acquisition was performed with an Argus photoelectron energy analyzer (Omicron Nano Technology GmbG) using a standard Mg source of Kα of 1253.6 eV photon energy.

3.3.8 Elastic Recoil Detection Analysis (ERDA)

ERDA is characterization technique based in the elastic scattering experienced between target and projectile atoms. Elastic scattering is born from short distance Coulomb interactions taking place when these units contact each other. Recoil atoms born from the scattered interaction are detected with a time of flight (ToF) detector allowing for their identification.[68]

ERDA allows for the acquisition of detailed elemental analysis and depth profiles upon incidence of an ion beam over a target sample. Elemental content is directly proportional to the yield of the recoiled atoms.[68]

However, ERDA is not the best technique for the analysis of powder samples due to its high sensitivity to changes in geometry, but it can provide acceptable results if a constant thickness of the sample is previously assumed.[68]

In this work, ERDA measurements were done using 40 MeV ^{127}I ions obtained from a 5 MV (megaVolt) tandem accelerator. Analysis was performed using a ToF-E telescope set up placed 40º from the detection of the ion beam. Angle between sample and ion beam was set at 70º. Flight path was 648 mm. Carbon foils of associated timing gates presented a surface density of 3.0 μg/cm^2 and 9.8 μg/cm^2.

3.4 Radiolabeling studies

3.4.1 Radioactive parameters

Radioactive parameters are used in radiolabeling experiments for the assessment of the amount of radioactivity lost during the procedure. These are used as indexes for the characterization of the final radiolabeled product. Radioactive parameters must be decay corrected ($t_{1/2}(^{18}F)$ = 109.77 min and $t_{1/2}(^{68}Ga)$ = 67.629 min) to a specific timepoint, which along this work it has always been the Start Of Synthesis (SOS) point.

Radioactivity concentration represents the amount of activity, measured for the final purified product, present per volume of reaction. It is obtained according to reaction (5):

$$Radioactivity\ concentration\ (MBq/mL) = \frac{Activity_{Final\ product}\ (MBq)}{Reaction\ volume\ (mL)} \qquad (5)$$

Radiochemical yield (RCY) addresses the amount of radioactivity measured in the final product with respect to that originally added to the sample. It estimates the percentage of radioactive element that has been successfully coordinated, as seen in equation (6).

$$RCY(\%) = \frac{Product\ activity_{Decay\ corrected\ to\ SOS}\ (MBq)}{Initial\ activity_{SOS}\ (MBq)} \cdot 100\ \% \qquad (6)$$

Specific activity indicates the amount of sample that has been radiolabeled per weight of precursor. Since the exact molecular mass of the studied particles is unknown, molar activity in MBq/mol could not be assessed along this work. This parameter must also be expressed with respect to the measured activity of the final purified product. Associated formula can be found in equation (7).

$$A_S = \frac{Product\ activity_{Final\ product}\ (MBq)}{Sample\ weight\ (mg)} \qquad (7)$$

3.4.2 Quality control

Quality control was based on the exposure of eluted instant Thin Layer Chromatography plates (iTLCs), spotted with the purified product, onto an autoradiography imaging plate. Evaluation of iTLCs under autoradiography allows for the determination of the radiochemical purity (RCP) of the radiolabeled product.

iTLC is a method based on the elution of samples along a permeable chromatography paper using an appropriate eluent for the characteristics of the sample. With respect to the products studied along this project, the high mass of the borosilicates is responsible for their retention at spotted position, whereas dissolved impurities and unbound elements are eluted to the front of the plate.

During radiolabeling experiments, reaction or product aliquots (5 µL) were spotted into glass microfibre chromatography paper serving as iTLC plates. ^{68}Ga-labeling studies required using heat activated glass microfibre chromatography paper impregnated with silicic acid (SA), and sodium citrate (0.1 M, pH 5.0) as eluent. ^{18}F-fluorination studies used glass microfibre chromatography paper impregnated with silica gel (SG) using acidified NaCl (0.9%) as eluent. Spotted iTLCs were left to dry before measuring them under autoradiography.

Autoradiography is a radiation imaging technique where radiation is detected with an autoradiographic film than can be later developed. Autoradiographic films are coated with elements that undergo excitation upon exposure to radiation. Images analyzed by digital autoradiography are processed by a computational software. Digital autoradiography presents about 50 to 100 more sensitive than classical methods based on the excitation of silver halide photographic emulsions.[69]

Autoradiography evaluations were done with Fluoro Image Analyzer, Fuji FLA 5100, where light emission is detected with a photomultiplier tube (PMT) and converted into a digital signal, to provide an image of the exposed iTLCs. Measurements were performed in IP-Standard mode. Exposed autoradiography imaging plates (IPs) were Fuji BAS-TR2025, made of barium fluorohalide phosphor crystals doped with europium. Upon exposure to radiation, an active layer becomes excited in the imaging plate (IP). Deexcitation of the IP can be achieved with a 620 nm laser. Digital autoradiography is composed of three main steps:[69]

1) Screen Exposure. Upon exposure to radiation, the Eu^{2+} atoms from the IP are excited to Eu^{3+} by releasing an electron ($Eu^{2+} \rightarrow Eu^{3+} + e^-$). The deposition of radiation energy into the IP leaves it in an stable high energy state which can then be analyzed.

2) Laser scan. An image for the distribution of radiation can be obtained by developing the IP with a autoradiography scan. This scanner uses a 620 nm red laser (generally a He-Ne laser) that excites the IP, so that the Eu^{3+} ions can return to Eu^{2+} emitting a photon. Depending on the amount of radioactivity of the sample, exposure time of the plates could be reduced or increased.

3) Detection of photoemission. Emitted photons are detected and amplified by PMT. Information is then translated into a computational signal that provides a grey coloured map of the affected spots. In essence, the darker the detected maps are, the more Eu^{3+} have returned to their Eu^{2+} state emitting photons and therefore, the more radiation is found in that spot.

To avoid the appearance of residual images, IPs are cleaned for the deletion of residual traces by 20 min irradiation under a source of white light. This allows for the reuse of the IP by allowing molecules to go back to their original state.[69]

The purity the spotted iTLCs was analyzed under autoradiography. Eluted iTLC strips were dried and placed against an imaging plate (IP) for 5 minutes while protected from background radiation. Exposed plates were then analyzed using a FLA image analyzer and interpreted using AIDA software.

Evaluation of iTLC plates upon exposure under autoradiography gives place to a shows a series of radioactive "spots" along the chromatography strips. When spotting a radioactive solution containing a radioactive agent, like $[^{68}Ga]GaCl_3$, dissolved compound will migrate top of the iTLC plates exactly as the used eluent, leaving a tail of radioactivity behind. However, since the borosilicate microparticles used along this work do not dissolve completely in aqueous or organic media, and they will remain in the bottom of the iTLC plate and will not migrate with the eluent. This could help defining what is called the retention factor orR_f, described as in equation (8).

$$R_f = \frac{Distance\ traveled\ by\ measured\ compound\ (cm)}{Distant\ traveled\ by\ eluent\ (cm)} \quad (8)$$

For this reason, and in all of radiolabeling experiments, borosilicate microparticles will remain at the bottom of the iTLC plates (Rf ~ 0). The rest of dissolved radioactive compounds will migrate with the eluent to the top (Rf ~ 1). Since there are no reaction intermediates, estimation of the Rf is not essential for this work, as every radioactivity trace observed with Rf > 0 will not correspond to the radiolabeled borosilicate particles. Evaluation of the measured activity under autradiography can provide an estimated area for each of the recorded spots. In essence, this represents the RCP of the radiolabeled products.

Images corresponding to iTLCs plates and their correspondent autoradiography interpretations have not been recorded along this work. The total amount of iTLC plates evaluated throughout radiolabeling experiments, including stability assays may be over 100, which is an excessive number. In essence, the importance of iTLCs is the estimation of the RCP of the final radiolabeled products, which can be simply represented in a table. However, additionally, and exclusively for the interest of the reader, real examples for each of the conducted radiolabeling experiments have been collected altogether in **Appendix 1**.

3.4.3 ^{68}Ga-labeling

An overview of the radiolabeling reaction scheme can be found along **Figure 15**. The general protocol for ^{68}Ga-labeling of formerly functionalized borosilicate samples is achieved according to the following steps:

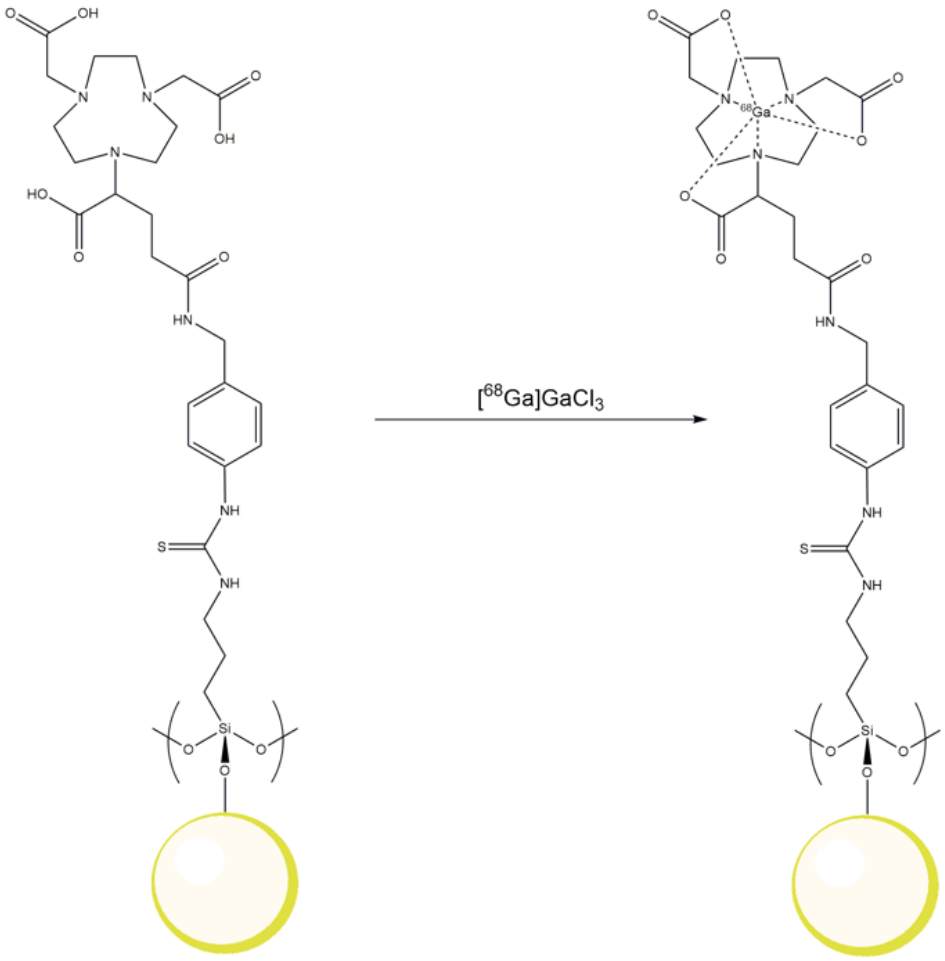

Figure 15. General reaction scheme for ^{68}Ga-labeling. This scheme represents the specific radiolabeling of NODAGA-APTES functionalized borosilicates. Borosilicates are represented in yellow.

1) [^{68}Ga]$GaCl_3$ elution from a ^{68}Ge/^{68}Ga generator. Gallium-68 was eluted from the ^{68}Ge/^{68}Ga generator as [^{68}Ga]$GaCl_3$ using a metal free 0.1 M HCl solution (10 mL). The produced [^{68}Ga]$GaCl_3$ eluate was concentrated in a Bond Elut SCX SPE column and subsequently eluted with acidified NaCl (0.5 – 1.0 mL). Acidified NaCl was previously prepared by dilution of HCl (12.5 µL, 5.5 M) in NaCl (500 µL, 5 M). The amount of radioactivity of the [^{68}Ga]$GaCl_3$ eluate varied between experiments, but it normally ranged between 140-220 MBq with. The highest activity of the [^{68}Ga]$GaCl_3$ eluate was of 430 MBq, and it was only achieved when an alternative generator was used.

2) Radiolabeling reaction. Functionalized borosilicates and precursors (**Table 2**) were dissolved in 0.2 M sodium acetate (CH_3COONa) buffer (0.909 mL, pH 4.0), ascorbic acid (0.1 mL) used as a reaction stabilizer, concentrated [^{68}Ga]$GaCl_3$ (0.1 mL, 20-40 MBq) and Chelex H_2O used for adjustment of the reaction volume to 1.5 mL (0.391 mL).

   The mixture was vigorously stirred with vortex, and then set to react in a dry bath incubator. Reaction was quenched with the addition of DTPA (48 µM, 2 µL), and the pH of the crude mixture was measured at 4.0-4.4. Crude mixture aliquots (5 µL) were spotted on iTLC paper and further eluted.

3) Product purification. Solvent was removed after reaction completion upon sedimentation of the microparticles by centrifugation (3 minutes, room temperature, 14000 rpm). The radiolabeled product was cleaned two times with an appropriate solution as stated along **Table 2**. Purified product aliquots (5 µL) were spotted on iTLC paper that was later eluted.

4) Quality control. Purity of final radiolabeled products was analyzed under autoradiography by exposure of the spotted iTLC strips.

Table 2. Conditions for ^{68}Ga-labeling of surface functionalized borosilicates. Detailed comments have been disclaimed when convenient.

^{68}Ga-labeled product	Weight (mg)	Reaction conditions	Washing steps	Comments
NODAGA-APTES borosilicate (44-µm)	1.0	15 minutes, 95 ºC	Chelex H_2O (1000 µL)	Only 2 washing steps were done
DFO-APTES borosilicate (2.2-µm)	0.6	15 minutes, room temperature	1 × PBS (500 µL)	-
DFO-PEG-Etthanolamine borosilicate (2.2-µm)	0.6	15 minutes, room temperature	1 × PBS (500 µL)	0.2 µL [^{68}Ga]$GaCl_3$ were added to 1 replica
NODAGA-APTES borosilicate (2.2-µm)	1.5	15 minutes , 95 ºC	Optimization from using 1 × PBS (500 µL) to EDTA solution (500 µL, 2 mM)	Experiments were continued with stability assays

The structures of the final [^{68}Ga]Ga-DFO-APTES, [^{68}Ga]Ga-DFO-PEG-Ethanolamine and [^{68}Ga]Ga-NODAGA-APTES labeled products are reported in **Figure *16*Figure 16**.

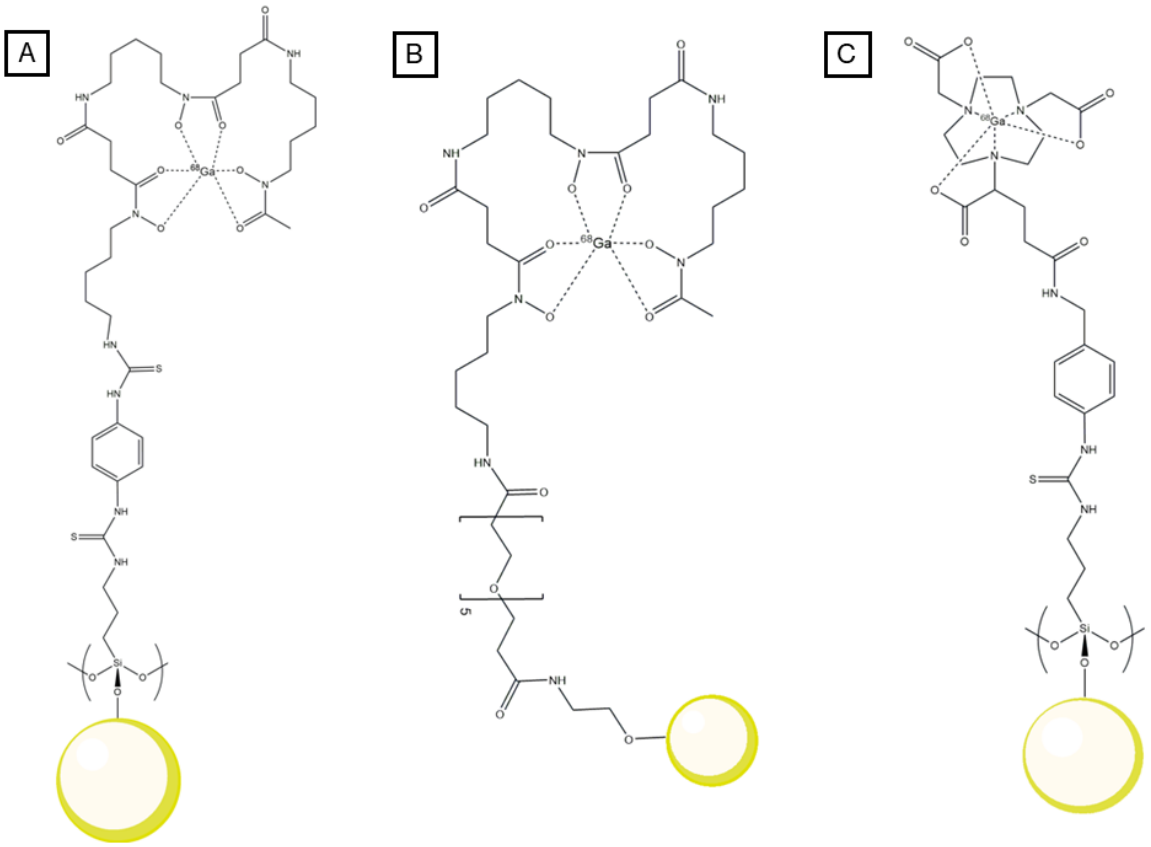

Figure 16. ^{68}Ga-labeling. Final structures of labeled [^{68}Ga]Ga-DFO-APTES, [^{68}Ga]Ga-DFO-PEG-Ethanolamine and [^{68}Ga]Ga-NODAGA-APTES final products.

3.4.4 ^{18}F-Fluorination

Unmodified and silanol activated HCl cleaned borosilicate microparticles were radiolabeled with [^{18}F]F$^-$ according to the next described reaction steps. Overall reaction scheme can be found in **Figure 17**.

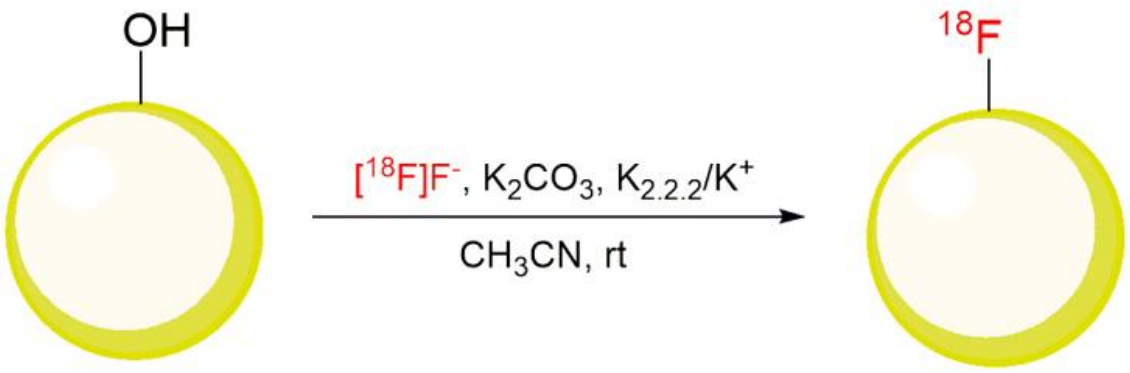

Figure 17. Radiofluorination of borosilicate microparticles. Glass particles are represented in yellow color.

1) Target irradiation. $[^{18}F]F^-$ was produced upon proton bombardment of a enriched $[^{18}O]H_2O$ target in a IBA Cyclone 10/5 cyclotron with a 10 MeV proton beam and an integrated current of 0.8 μA. Produced $[^{18}F]F^-$ was transferred into a Waters Accell QMA Light Sep-Pak cartridge preconditioned with K_2CO_3 (0.5 M, 10 mL) and washed with deionized H_2O (15 mL).

2) Elution from QMA cartridge. $[^{18}F]F^-$ was eluted with a eluent mix of Kryptofix 2.2.2 (9.5 mg), K_2CO_3 (1.7 mg) and deionized H_2O (80 μL) dissolved in anhydrous CH_3CN (1.92 mL). Eluted $[^{18}F]F^-$ was transferred to a new vial using a gas flow of 20 mL/min.

3) Azeotropic distillation. The CH_3CN and H_2O solution containing $[^{18}F]F^-$ was brought to evaporation at 100ºC with a controlled gas flow of 40-70 mL/min. $[^{18}F]$KF/K2.2.2 is cooled down to 15 ºC and finally dissolved in CH_3CN (1 mL). Measured activity was of about 380 MBq.

4) Radiolabeling reaction. Four sets of unmodified and HCl cleaned 2.2-μm borosilicates had been previously dissolved in anhydrous CH_3CN (200 μL). Addition of the dissolved $[^{18}F]$KF/K2.2.2 (100 μL) into each reaction vial was then performed.

   The mixture was vigorously mixed with vortex, and then set to react. For different sets of reactions were performed, those being Set 1 (15 minutes, room temperature), Set 2 (30 minutes, room temperature), Set 3 (15 minutes, 60ºC) and Set 4 (30 minutes, 60ºC). Reaction was quenched through the addition of deionized H_2O. Crude mixture aliquots (5 μL) were spotted Purified product aliquots (5 μL) were spotted on iTLC paper and then eluted.

5) Product purification. Solvent excess was removed after reaction completion upon sedimentation of the microparticles by centrifugation (3 minutes, room temperature, 14000 rpm). The radiolabeled products were cleaned two times with deionized H_2O (500 μL) through centrifugation (15 minutes, room temperature, 14000 rpm). Purified product aliquots (5 μL) were spotted oniTLC paper and then eluted.

6) Quality control. Purity of final radiolabeled products was analyzed under autoradiography Upon exposure of the spotted iTLCs.

3.5 Stability assays

Stability assays were conducted to determine the amount of intact radiolabeled particle observable in different media over an intermediate amount of time. The main idea of stability assays is to determine the percentage of intact radiotracer over time. These were only performed in [^{68}Ga]Ga-NODAGA-APTES 2.2-µm borosilicates.

Stability assays need to be done prior in vivo experiments. For this reason, they must be carried out in close to physiological conditions (37 ºC, physiological media). Different media evaluated were 1 × PBS, 50% human plasma in 1 × PBS, 0.2 mM $FeCl_3$, 2 mM EDTA and SLF. PBS is used as a buffer system that replicates serum conditions (excluding proteins) by stabilizing samples to a physiological pH, similar ionic composition, and a similar osmotic pressure in order to prevent cell rupture. Stability in donor human plasma is also necessary for stability assays of tracers directed for human studies $FeCl_3$ was assessed as a solution simulating an increased iron content than that naturally present in the human body (10-30 × 10^{-6} M) .[70] Stability in EDTA was evaluated due to its complexing agent behaviour. SLF was a solution that simulated the chemical behaviour of fluid in the lungs. Stability over a 0-3 h period was assessed for final ^{68}Ga-labeled products.

The SLF solution was prepared by dissolving the chemicals stated along **Table 3** in descending order, in deionized H_2O (1L) warmed at 37 ºC and adjusted to pH 7.5.

Table 3. SLF composition. Chemicals were added successively, in the descending order shown along this table.

Compound name	Chemical formula	Proportion (g)
Sodium chloride	NaCl	6.802
Disodium hydrogen phosphate	$N_2HPO_4 \cdot 12H_2O$	5.084
Calcium chloride dihydrate	$CaCl_2 \cdot 2H_2O$	0.291
Sodium acetate	CH_3COONa	0.578
Sodium hydrogen carbonate	$NaHCO_3$	2.302
Citric acid	$C_6H_8O_7$	0.420
Glycine hydrochloride	$C_2H_5NO_2 \cdot HCl$	0.667
Ammonium chloride	NH_4Cl	5.296
Phosphoric acid	H_3PO_4	1.196
Sodium carbonate	Na_2CO_3	0.629
Potassium acid phtalate	C_8H5KO_4	0.202
Sulfuric acid	H_2SO_4	0.508
Sodium citrate dihydrate	$Na_3C_6H5O_7 \bullet 2H_2O$	0.591
Sodium acid trihydrate	$C_6H_{11}Na_3O_{10}$	0-630

The general procedure for performing stability assays in radiolabeled products can be described as following:

1) Incubation in physiological media. Overtime stability of the purified product was checked every. Incubation took place in 100% 1 × Phosphate Buffered Saline (PBS, 200 μL), 50% human plasma (100 μL) in 1 × PBS (100 μL), 0.2 mM $FeCl_3$ (200 μL), 2 mM EDTA (200 μL) and Simulated Lung Fluid (SLF, 200 μL) for 3 hours at 37 ºC under low stirring (350 rpm) in a heating block with integrated mixing. Aliquots (5 μL) were spotted on a a heat-activated glass microfibre chromatography paper impregnated with SA for quality control through iTLC evaluation, using sodium citrate (0.1 M, pH 5.0) as eluent.

2) Quality control. Purity of final radiolabeled products was analyzed under autoradiography upon exposure of the spotted iTLC strips.

4 Results and discussion

The discussion of surface modification procedures was based on the characterization of functionalized borosilicate microparticles. Radiolabeling performance was discussed based on radioactivity concentration, RCY and A_s results. Stability over time was evaluated upon radiolabeling stability assays.

4.1 Surface silanol group activation

The confirmation of a successful activation of the surface silanol groups was only evaluated under FTIR. FTIR spectra for the understanding of surface silanol activation upon acid and basic washing are recorded in **Figure 18.** Associated band assignment can be found along **Table 4**.

Silanol group activation in HCl washed 2.2-µm glass particles is evident due to the formation of a broad band centered at 3319 cm^{-1} corresponding to the stretching vibrations of O-H and Si-OH groups, and the band present at 1632 cm^{-1} corresponding to the bending vibration of O-H.[48,71,72] Further reaffirmation can be obtained from the band observed at 799 cm^{-1} corresponding to Si-OH stretching.[73] This confirms that silanol groups were successfully activated upon acid washing.

However, this is not the case for the 44-µm modified particles, as their FTIR vibration profile remains identical to that observed for the unmodified borosilicates. Band shape, position and intensity remains unaltered with respect to the unmodified sample. The only evidence of silanol activation could be based off the band centered at 1680 cm^{-1} coincident with O-H bending vibrations, but the intensity of this band is not high enough to confirm the activation of silanol groups.[71,72] This is likely due to the increased surface area of larger particles, which limits the possibility of successfully achieving significant surface modifications to an extent detectable by most techniques.

In essence, evidence showcased that HCl cleaning of the borosilicate particles was the preferred method for activation of the superficial silanol groups.[14,50] No significant effect was observed upon basic washing of the particles based on their FTIR spectra, as opposed to that recorded for activation with HCl.

A

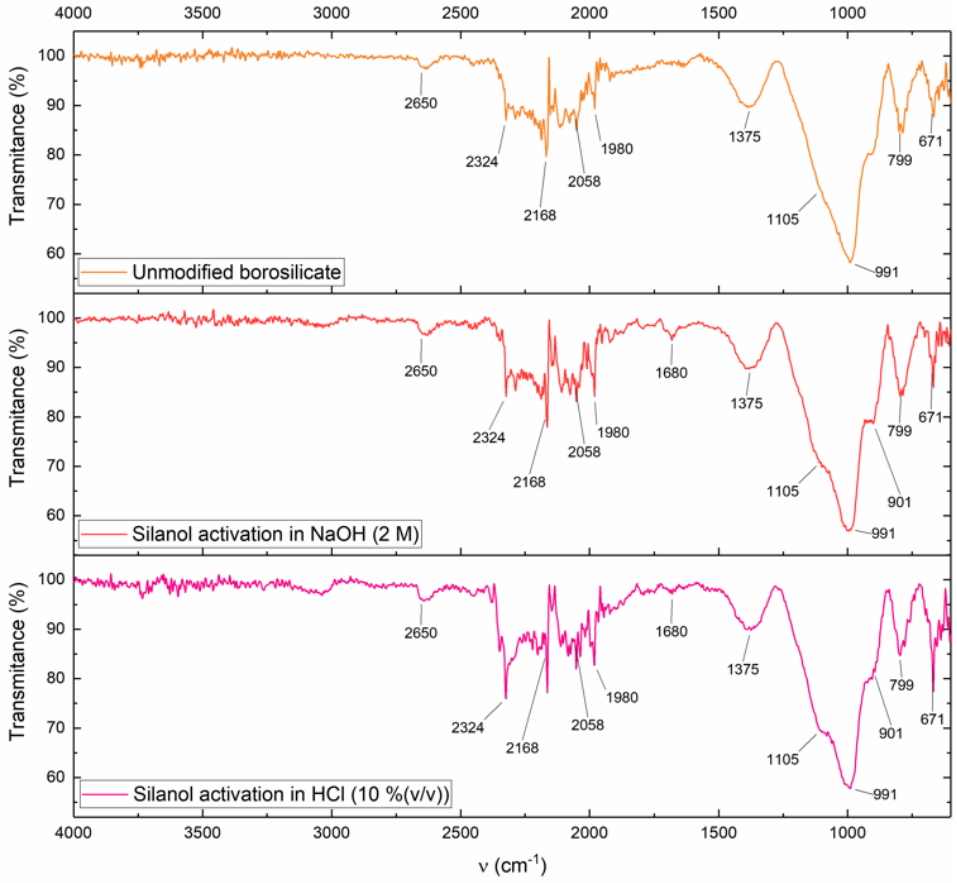

B

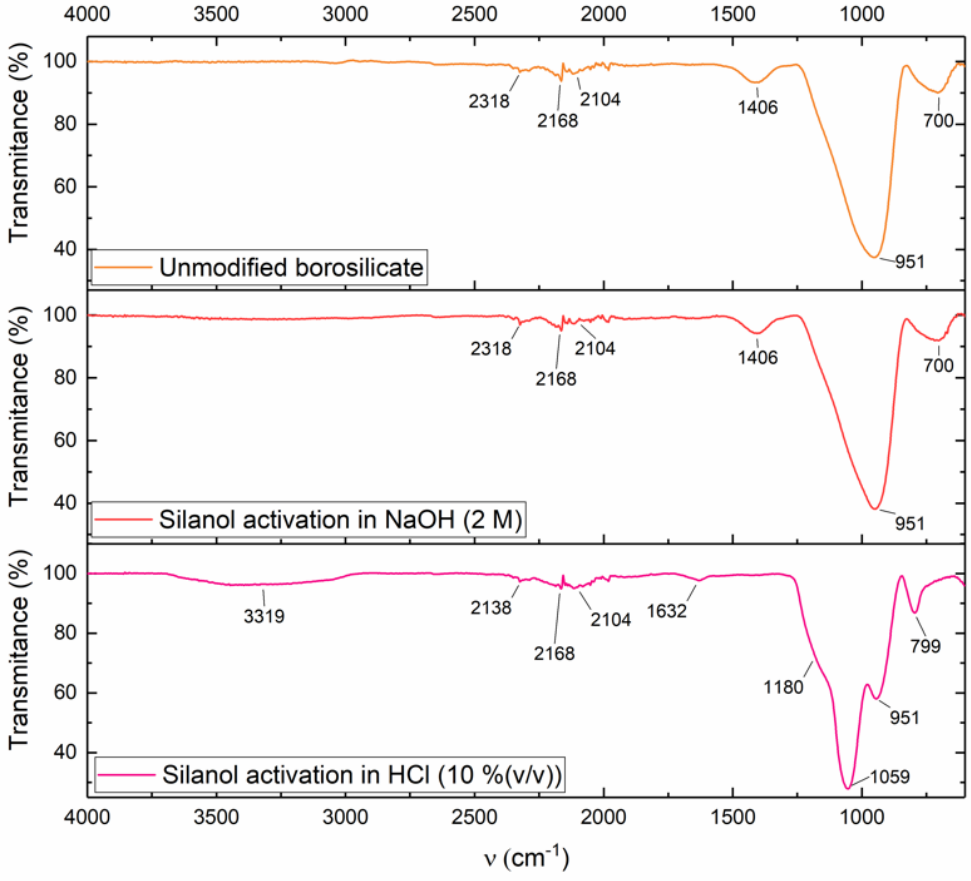

Figure 18. ATR FTIR spectra of unmodified and silanol activated borosilicate particles. Recorded frequency of significant vibration bands is indicated with an arrow. Borosilicates with (A) 44-µm and (B) 2.2--µm mean diameter size.

Table 4. Assignation of FTIR band vibrations observed in the FTIR spectra of silanol activated microparticles. Symbols "ν" and "δ" represent stretching and bending vibrations, respectively.

		44-µm borosilicate microparticles		
Vibration mode	Band intensity	Unmodified	Silanol activation in NaOH (2 M)	Silanol activation in HCl (10% (v/v))
		Frequency (cm^{-1})		
δ[BO_3]	Medium	671	671	671
ν(Si-OH)	Medium	799	799	799
ν(Si-O-Si)	Intense	901	901	901
ν(Si-O-Si)$_{as}$, ν[BO_4]	Very intense	991	991	991
ν(Si-O-Si)	Intense	1105	1105	1105
ν[BO_3]	Medium	1375	1375	1375
δ(O-H)	Very weak	-	1680	1680
Glass matrix	Medium/Intense	1980	1980	1980
Glass matrix	Medium/Intense	2058	2058	2058
Glass matrix	Medium/Intense	2168	2168	2168
Glass matrix	Medium/Intense	2324	2324	2324
ν(O-H), ν(Si-OH)	Weak	2650	2650	2650

		44-µm borosilicate microparticles		
Vibration mode	Band intensity	Unmodified	Silanol activation in NaOH (2 M)	Silanol activation in HCl (10% (v/v))
		Frequency (cm^{-1})		
δ[BO_3]	Medium	700	700	-
ν(Si-OH)	Medium	-	-	799
ν(Si-O-Si)	Intense	951	951	951
ν(Si-O-Si)$_{as}$, ν[BO_4]	Very intense	-	-	1059
ν(Si-O-Si)	Medium	-	-	1180
ν[BO_3]	Medium/Weak	1406	1406	-
δ(O-H)	Very weak	-	-	1632
Glass matrix	Weak	2104	2104	2104
Glass matrix	Weak	2168	2168	2168
Glass matrix	Weak	2318	2318	2318
ν(O-H), ν(Si-OH)	Weak *(broad)*	-	-	3319

The rest of the bands have been assigned as well. Bands between 900-1100 cm^{-1} correspond to Si-O-Si stretching vibration modes. In the 44-µm particles these are the bands centered at 901 cm^{-1}, 991 cm^{-1}, and shoulder band found at 1105 cm^{-1}. The 991 cm^{-1} antisymmetric vibration band of [BO_4], and the 671 cm^{-1} and 1375 cm^{-1} bands, respectively correspondent to the bending and antisymmetric stretching vibrations of [BO_3] trihedra, appear to be constant in both HCl treated and unmodified borosilicate spectra.[72,74,75] Remaining vibration bands were concordant with those assigned for the 44-µm sized microparticles.

In the 2.2-µm particles these bands are slightly shifted to higher frequency values due to the compositional differences, centered at 951 cm^{-1}, 1059 cm^{-1}, as well as the shoulder found at 1180 cm^{-1}.[72,74,75] The 951 cm^{-1} vibration band is also visible in the unmodified borosilicate material with a similar intensity. The 1059 cm^{-1} vibration

band, correspondent to the antisymmetric Si-O-Si stretching vibration, is also coincident with the antisymmetric vibration band of [BO_4].[73,76] An increased intensity of this band can be associated to the transformation of [BO_3] trihedra into [BO_4] tetrahedra upon hydrolyzation of the glass matrix and combination with the silicate network. This is evidenced with the disappearance of the 700 cm^{-1} and 1406 cm^{-1} bands corresponding to the bending and antisymmetric stretching vibrations of [BO_3] trihedra, respectively.[71,77,78]

Intrinsic matrix vibrations of the microparticles are found between 1300-2800 cm^{-1}. These are centered at exactly 1980 cm^{-1}, 2058 cm^{-1}, 2168 cm^{-1} and 2324 cm^{-1} for the 44-µm borosilicates, and at 2104 cm^{-1}, 2168 cm^{-1} and 2318 cm^{-1} for the 2.2-µm borosilicates. The assignment of these bands can be uncertain due to their weak intensity, as well as to the variable composition of the synthetic microparticles. Similar vibration profiles have been found in literature regarding borosilicate glasses with a significant Al_2O_3 content, though band assignation is not discussed.[48,74]

Overall, FTIR analysis of 2.2-µm and 44-µm borosilicates showcases the similarity in composition between both particles, based on their vibration profiles. Silanol group activation of the 2.2-µm particles is proved successful upon the application of an HCl (10%(v/v)) treatment. This was considered more attractive regarding functionalization approaches. The absence of confirmation for silanol group activation under FTIR served as one of the main reasons for the discontinuation of experiments with the 44-µm borosilicates. In essence, although the aim of the project was to induce minimal surface alterations of the studied borosilicate microparticles, an extremely low number of superficial silanol groups could greatly limit following functionalization procedures.

4.2 Surface functionalization of borosilicates with APTES

4.2.1 Characterization techniques

Experimental results for the functionalization of borosilicate microparticles with APTES are shown in chronological order. Not all APTES concentrations could be measured in every technique for the 44-µm particles, therefore these will always be specified. As explained in the experimental protocol, 2.2-µm microparticles were only functionalized with 2 mM APTES, so this will be omitted throughout.

4.2.1.1 FTIR

FTIR spectra of APTES functionalized 2.2-µm and 44-µm microparticles are as observed in **Figure 19**. Characteristic vibration bands are recorded along **Table 5**.

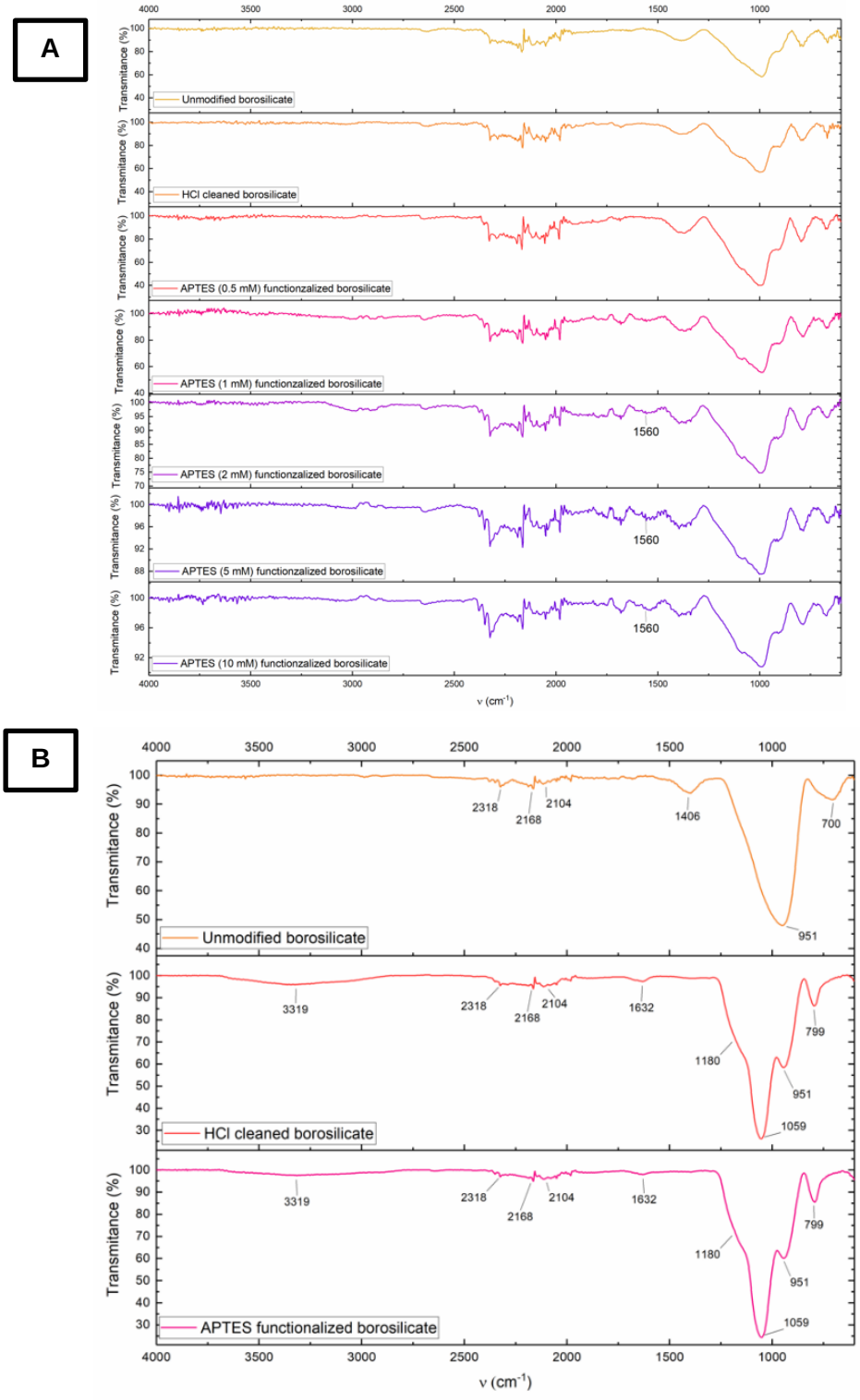

Figure 19. ATR FTIR spectra for surface functionalization with APTES. (A) 44-µm and (B) 2.2-µm borosilicates**.** Spectra of samples had to be normalized because of alterations performed in the spectral parameters of the instrument. Recorded transmittance of APTES functionalized 44-µm samples (2 mM, 5 mM and 10 mM) illustrates lower values due to the small amount of sample available for characterization.

Table 5. Assignation of FTIR band vibrations observed in the FTIR spectra of APTES functionalized microparticles. Symbols "ν" and "δ" represent stretching and bending vibrations, respectively. Borosilicate with 44-µm mean diameter size.

		44-µm borosilicate microparticles						
		Unmodified	HCl cleaned	APTES (0.5 mM)	APTES (1 mM)	APTES (2 mM)	APTES (5 mM)	APTES (10 mM)
Vibration mode	Band intensity	Frequency (cm^{-1})						
$\delta[BO_3]$	Medium	671	671	671	671	671	671	671
ν(Si-OH)	Medium	799	799	799	799	799	799	799
ν(Si-O-Si)	Intense	901	901	901	901	901	901	901
$\nu(Si\text{-}O\text{-}Si)_{as}$, $\nu[BO_4]$	Intense	991	991	991	991	991	991	991
ν(Si-O-Si)	Intense	1105	1105	1105	1105	1105	1105	1105
$\nu[BO_3]$	Medium	1375	1375	1375	1375	1375	1375	1375
$\delta(NH_2)$	Weak	-	-	-	-	1650	1650	1650
δ(O-H)	Very weak	-	1680	1680	1680	1680	1680	1680
Glass matrix	Medium	1980	1980	1980	1980	1980	1980	1980
Glass matrix	Medium	2058	2058	2058	2058	2058	2058	2058
Glass matrix	Medium	2168	2168	2168	2168	2168	2168	2168
Glass matrix	Medium/Intense	2324	2324	2324	2324	2324	2324	2324

		2.2-µm borosilicate microparticles		
		Unmodified	HCl cleaned	APTES
Vibration mode	Band intensity	Frequency (cm^{-1})		
		700	-	-
$\delta[BO_3]$	Medium	-	799	799
ν(Si-OH)	Medium	951	951	951
ν(Si-O-Si)	Intense	-	1059	1059
$\nu(Si\text{-}O\text{-}Si)_{as}$, $\nu[BO_4]$	Very intense	-	1180	1180
ν(Si-O-Si)	Medium	1406	-	-
$\nu[BO_3]$	Medium/Weak	-	1632	1632
δ(O-H)	Very weak	2104	2104	2104
Glass matrix	Weak	2168	2168	2168
Glass matrix	Weak	2318	2318	2318
Glass matrix	Weak	-	3319	3319

The overall profiles of the functionalized borosilicates remains the same as that reviewed for the unmodified and HCl cleaned borosilicate microparticles. Identical FTIR profiles of both HCl cleaned and APTES functionalized borosilicates showcase that APTES functionalization cannot be observed upon FTIR. The interpretation of the bands is therefore exactly as that described along the characterization of silanol activated particles. No new vibration bands can be attributed to either NH_2 stretching (3450 – 3300 cm^{-1}), NH_2 bending (1650 – 1400 cm^{-1}) or hydrocarbon stretching (3000 – 2900 cm^{-1}).[72]

A new band at 1560 cm^{-1} seems to appear with higher APTES concentrations only in the 44-µm particles, possibly corresponding to NH_2 bending.[72,79] This could be attributed to the detection of amine groups present in the APTES molecules.

However, this contribution was uncertain. At the time of evaluation, FTIR spectra were suspected to be contaminated with cleaning products embedded in the measurement plate. Bands located at 1550 cm^{-1} were also being recorded in replicas of

unmodified and HCl cleaned borosilicates, amongst others. Furthermore, APTES grafting into borosilicate materials should mainly be confirmed through more sensitive techniques such as XPS, as suggested by literature.

44-µm microparticles were not very interesting for the development of radiotracers resembling CsMPs as the size of these was larger than that of type A CsMPs. However, experimentation with them was mainly used for testing suitable APTES concentrations for surface modification. Still, experiments with 44-µm microparticles were still conducted until their final discontinuation based on their radiolabeling performance.

FTIR is therefore not a suitable technique for the assessment of superficial functionalization of borosilicate microparticles with any of the studied agents, since surface modifications are performed with very small concentrations of APTES. FTIR does not have enough sensitivity for detecting functional groups present in such a small extent.

4.2.1.2 TGA

TGA profiles of APTES functionalized 2.2-µm and 44-µm borosilicates can be found in **Figure 20** and **Table 6**. Only the highest concentration of APTES (10 mM) was evaluated for the 44-µm borosilicate particles.

TGA was initially performed on different functionalized samples to assess if the presence of the organic grafting molecules could be detected. If slight mass variations were to be observed, it could confirm that the functionalizing agent was lost upon evaporation. Borosilicate microparticles were expected to remain solidified due to their high meting point, of about 1250 ºC for conventional borosilicate glasses.[80]

Discussion of results obtained by TGA becomes challenging without performance of a simultaneous Differential Scanning Calorimetry (DSC) evaluation. DSC evaluates energy changes in the sample, which can help provide a more detailed insight on the type of process taking place, whereas TGA only evaluates property changes upon an increase in temperature. No supporting DSC evaluations were performed along this work since TGA was only momentarily employed as a survey technique.[81]

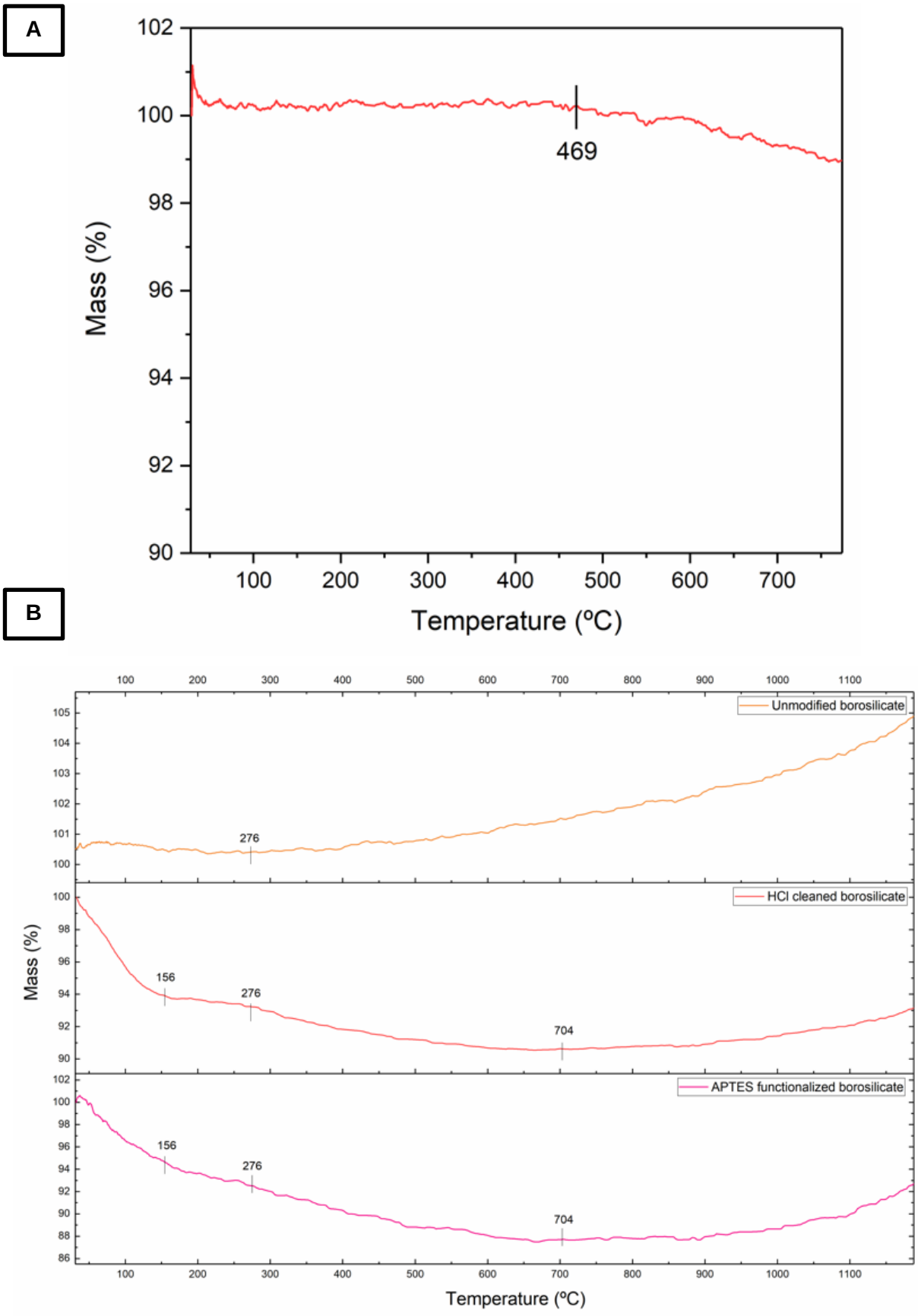

Figure 20. TGA profiles of APTES functionalized borosilicate particles. Borosilicate with (A) 44-µm and (B) 2.2-µm mean diameter size.

Table 6. Assignation of TGA steps of APTES functionalized microparticles. Borosilicates with 44-µm and 2.2-µm mean diameter size.

44-µm borosilicate microparticles				
APTES (10 mM)				
Stage name	Temperature range (ºC)	Percentage range of weight loss (%)	Net percentage of weight loss (%)	Assignation
Step 1	25 – 469	100.00 – 100.2	-0.2	Stability range
Step 2	469 – 800	100.2 – 99.0	1.2	Glass transition

2.2-µm borosilicate microparticles				
Unmodified				
Stage name	Temperature range (ºC)	Percentage range of weight loss (%)	Net percentage of weight loss (%)	Assignation
Step 1	25 – 276	100.0 – 100.4	-0.5	Stability range
Step 2	276 – 1200	100.4 – 104.9	-4.6	Sample oxidation
HCl cleaned				
Stage name	Temperature range (ºC)	Percentage range of weight loss (%)	Net percentage of weight loss (%)	Assignation
Step 1	25 – 156	100.0 – 93.9	6.1	Moisture release
Step 2	156 – 276	93.9 – 93.2	0.7	Stability range
Step 3	276 – 704	93.3 – 90.6	2.7	Glass transition
Step 4	704 – 1200	90.6 – 92.9	-2.3	Sample oxidation
APTES				
Stage name	Temperature range (ºC)	Percentage range of weight loss (%)	Net percentage of weight loss (%)	Assignation
Step 1	25 – 156	100.0 – 94.5	5.5	Moisture release
Step 2	156 – 276	94.5 – 92.5	2.1	Stability range
Step 3	276 – 704	92.5 – 87.7	4.8	Glass transition
Step 4	704 – 1200	87.7 – 92.8	5.1	Sample oxidation

Discussion of the different borosilicate samples is different based on the recorded profiles. In the 44-µm borosilicate, mass percentage remains constant over a wide temperature range of 25 – 469 ºC indicating particle stability. Weight percentage loss is recorded as of -0.21%, representing fluctuations in the recordings of the instrument. No real loss of compound is taking place along this step. Upon reaching 469 ºC, mass percentage appears to slowly decrease until a minimal weight loss of 1.1 % is recorded. This is concordant with the glass transition temperature (T_g) of borosilicate glass, which is normally considered to be of about 460 ºC.[82–84] This value can vary depending on the composition of the studied material. T_g represents the point where an amorphous material starts to gradually transition from a rigid to a flexible state, and it can serve as an indicator for structural degradation.[85–87]

However, for the 2.2-µm borosilicates, different steps and temperature ranges can be observed. Initially, the TGA profile of the unmodified borosilicate can be described through only two different stages. Between 25 – 276 ºC, the sample appears

to be stable with slight instrumental fluctuations. No lost of absorbed moisture is recorded, as the unmodified particles are commercially stored with a moisture absorber. From 276 – 1200 ºC, a mass increase is observed, attributed superficial oxidation reactions of silicon with oxygen or other gaseous contaminants within the purge gas, forming SiO_x.[88]

In both HCl cleaned and APTES functionalized 2.2-µm samples, four different stages are observed instead. A first step from 25 – 156 ºC represents a weight loss of 6.1 and 5.5 %, respectively, associated to the volatilization of absorbed water.[82] The second stage shows an almost isothermal plateau, where the sample appears to be stable with a minimal weight loss of about 1-2 %. This effect becomes more evident for the HCl cleaned sample. However, this behaviour could also be explained as an additional extension of the former evaporation step. Along the third step, a noticeable weight loss of 2.7 and 4.8 %, respectively, is detected, correspondent to the glass transition region.[82,84] The recorded T_g of 276 ºC is lower to what is generally reported for borosilicate glasses. Although T_g may vary depending on the composition of the glass particles, this association cannot be confirmed in the absence of DSC evaluation. Alternative assignations have not been discussed in referred literature.[82,83] The fourth step represents sample oxidation taking place between 704 – 1200 ºC.[88]

Based on the profiles recorded for both types of particles, no effects associated to the functionalization of the borosilicates can be observed. This confirms that TGA is not a suitable technique for the confirmation of surface functionalization. For this reason, no further evaluations were performed under TGA. Furthermore, TGA analysis of borosilicates seems to be very imprecise without simultaneous DSC evaluations. If possible, it would also be recommended to perform measurements under vacuum or purified purge gas.

4.2.1.3 EDS

EDS analysis was performed in order to evaluate the overall composition of the microparticles. Nitrogen content was also examined in aims of estimating the amount of superficial amine ends inserted upon APTES grafting. unmodified, HCl cleaned an APTES (0.5 mM and 10 mM) functionalized borosilicate 44-µm particles were performed for estimation of their composition.

Unmodified and APTES functionalized 2.2-µm particles were also measured. In this case, and exceptionally throughout the extent of this thesis, a reference sample functionalized with a higher concentration of APTES (10 mM) than that described in the experimental procedure (2 mM), was analyzed instead. This was done exclusively to determine if nitrogen content could be observed in an over-modified sample under EDS, in order to determine if it was a suitable technique for the confirmation of surface functionalization, before continuing analysis. Measured sections and sample composition results can be found along **Figure 21** and **Table 7**, respectively.

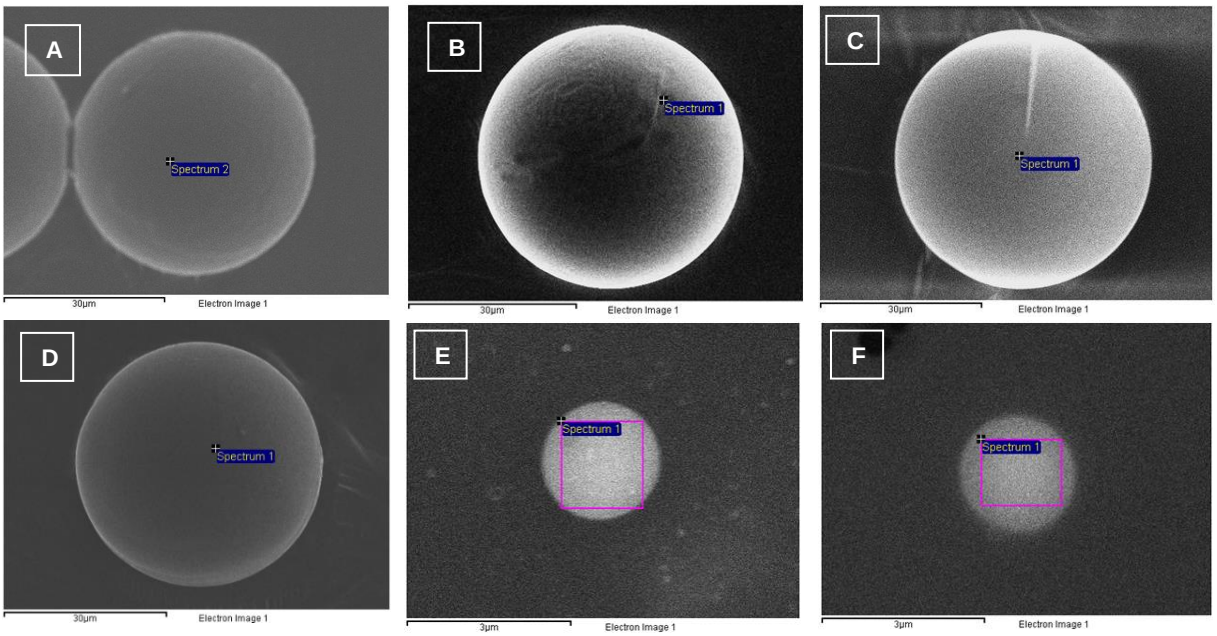

Figure 21. Particle sections subjected to EDS analysis. Unmodified **(A)**, HCl cleaned **(B)** and APTES functionalized (10 mM) **(C)** and (0.5 mM) **(D)** 44-µm borosilicate. Unmodified **(E)** and APTES functionalized (10 mM) **(F)** 44-µm borosilicate.

Table 7. Composition results obtained by EDS. 44-µm and 2.2-µm borosilicates.

	44-µm borosilicate microparticles			
	Unmodified			
Element	Weight (%)	Atomic (%)	Compound (%)	Formula
Na K	2.47	2.16	3.33	Na_2O
Al K	2.16	1.61	4.09	Al_2O_3
Si K	43.28	30.91	92.58	SiO_2
O	52.09	65.32		
Totals	100.00			

	HCl cleaned			
Element	Weight (%)	Atomic (%)	Compound (%)	Formula
Na K	2.18	1.90	2.94	Na_2O
Al K	1.60	1.19	3.03	Al_2O_3
Si K	43.95	31.39	94.03	SiO_2
O	52.26	65.52		
Totals	100.00			

	APTES (0.5 mM)			
Element	Weight (%)	Atomic (%)	Compound (%)	Formula
Al K	2.28	1.69	4.30	Al_2O_3
Si K	44.73	31.92	95.70	SiO_2
O	52.99	66.38		
Totals	100.00			

	APTES (10 mM)			
Element	Weight (%)	Atomic (%)	Compound (%)	Formula
Na K	1.58	1.37	2.12	Na_2O
Al K	2.23	1.66	4.21	Al_2O_3
Si K	43.79	31.27	93.67	SiO_2
O	52.41	65.70		
Totals	100.00			

	2.2-µm borosilicate microparticles			
	Unmodified			
Element	Weight (%)	Atomic (%)	Compound (%)	Formula
Al K	8.00	6.36	15.12	Al_2O_3
Si K	29.29	22.37	62.66	SiO_2
Ca K	15.88	8.50	22.23	CaO
O	46.83	62.77		
Totals	100.00			

	APTES (10 mM)			
Element	Weight (%)	Atomic (%)	Compound (%)	Formula
Al K	8.09	6.37	15.29	Al_2O_3
Si K	30.73	23.24	65.75	SiO_2
Ca K	13.55	7.18	18.96	CaO
O	47.62	63.21		
Totals	100.00			

Continuation of **Table *7***.

Results indicate that the overall sample composition between 44-µm and 2.2-µm particles is not the same, which agree with the indications form the manufacturer. Composition by weight (%) of 44-µm borosilicates agrees with that provided by the manufacturer, of of 2-6% Na_2O, 2-5% Al_2O_3, and 75-85% SiO_2. Na_2O, Al_2O_3, SiO_2 and O weight, atomic and compound percentages deviations among samples do not exceed 1% in any case. This was considered acceptable due to the limited sensitivity of the technique. Boron content, estimated by weight to range between 12–16% B_2O_3, is not detected in any of the samples. Only the APTES (0.5 mM) functionalized sample did not present any Na_2O content, but this can be associated with the specific section subject to analysis, which specifically registered increased an Al_2O_3 content. Silicon content is found among the same levels as the rest of the sample.In the 2.2-µm borosilicates, recorded compound percentages also agree with the theoretical 14.5% Al_2O_3, 52.5% SiO_2 and 22.5% CaO composition provided by the manufacturer. The rest

of constituents recorded in the particle data sheet (8.6% B_2O_3, 1.2% MgO, 0.3% Na_2O, 0.2% FeO/Fe_2O_3, and 0.2% K_2O) are not detectable under EDS due to their small concentrations.

No alterations on the composition of the borosilicates can be observed for either of the different functionalized microparticles. No nitrogen or increased SiO_2 content are observed upon functionalization with APTES, because of the low concentrations of grafting agent employed. This suggests that EDS analysis is not a suitable technique in the confirmation surface modification, and that functionalization with APTES does not cause significant alterations in the composition of the samples.

4.2.1.4 SEM

Analysis of SEM images was performed for both 2.2-µm and 44-µm sized microparticles to ensure minimal superficial alteration upon functionalization. **Figure 22** shows the correspondent photographs and size distribution histograms for both types of particles.

As recorded in **Figure 22**, SEM images and histograms have been differentiated for unmodified (**A-C**), and APTES (0.5 mM) functionalized 44-µm particles (**D-F**); as well as for unmodified **(G-I)**, HCl cleaned **(J-L)**, APTES functionalized **(M-O)**, and NODAGA-APTES functionalized borosilicates **(P-R)**. Diameter size distribution of 44-µm and 2.2-µm borosilicates was obtained upon the measurement of 13 and 100 particles, respectively.

All samples conserve the same spherical morphology upon functionalization. The larger borosilicates show a mean diameter size of 44 ± 1 µm for both unmodified and APTES functionalized samples, agreeing with the theoretical particle size of 44-µm provided by the manufacturer. As for the smaller borosilicates, mean particle size varied slightly within samples, being of 2.1 ± 0.1 for unmodified, 2.2 ± 0.2 µm for HCl cleaned, 2.2 ± 0.2 µm for APTES functionalized, and 2.1 ± 0.2 µm for NODAGA-APTES functionalized borosilicates. These all agree with the theoretical 2.2 ± 0.3 µm diameter size of the particles provided by the manufacturer. Close-up images of the isolated microparticles illustrate the same spherical morphology in all cases.

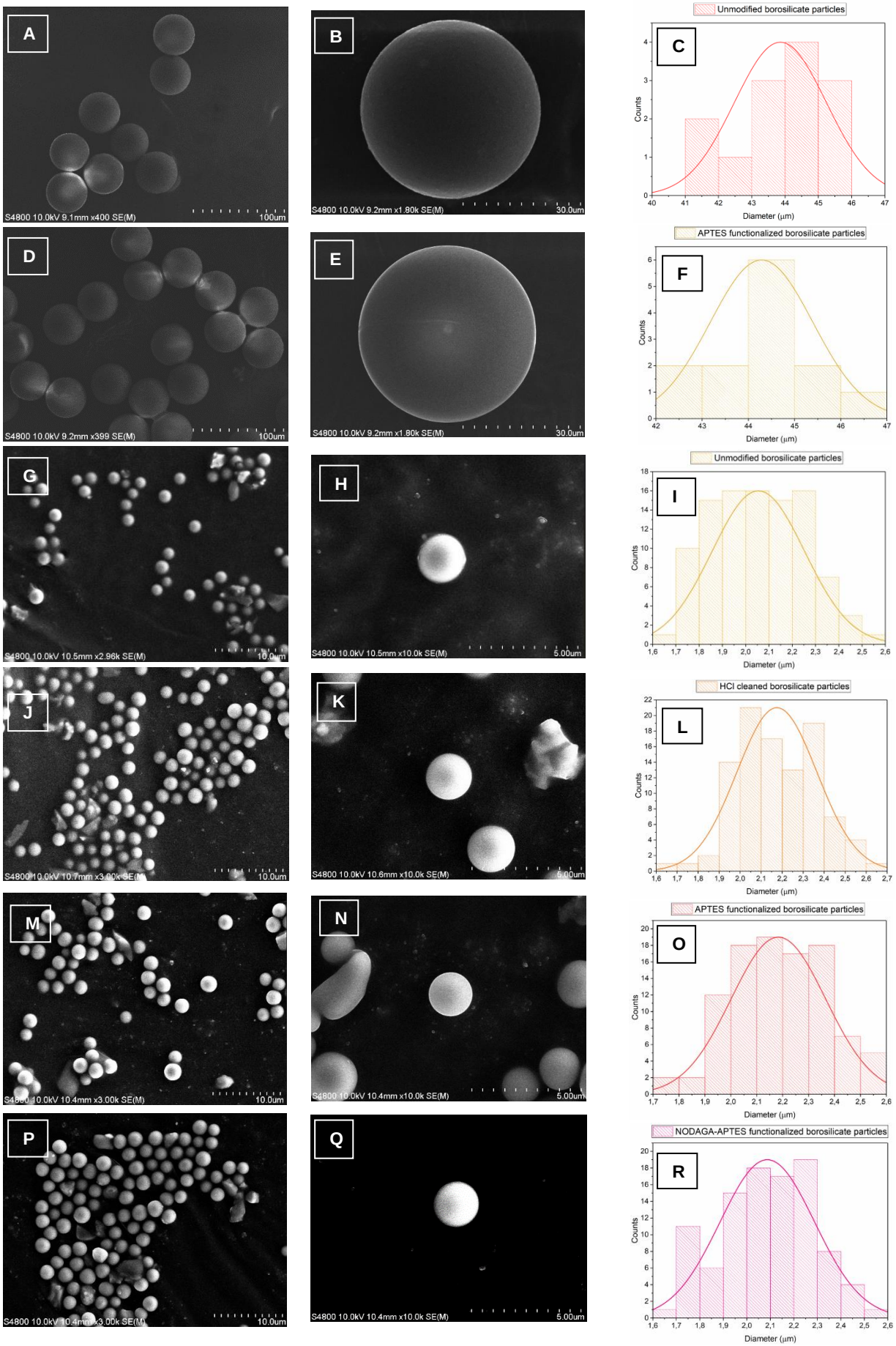

Figure 22. SEM images and size distribution histograms of 44-µm borosilicate samples. Unmodified (A-C), and APTES (0.5 mM) functionalized 44-µm particles (D-F); unmodified (G-I), HCl cleaned (J-L), APTES functionalized (M-O), and NODAGA-APTES functionalized borosilicates (P-R). Size distribution was respectively of 44 ± 1 µm (N=13), 44 ± 1 µm (N=13), 2.1 ± 0.1 µm (N=100), 2.2 ± 0.2 µm (N=100), 2.2 ± 0.2 µm (N=100) and 2.1 ± 0.2 µm (N=100). N is the number of particles measured.

SEM images confirm that superficial functionalization with APTES does not significantly alter the morphology of the synthetic borosilicates. Conjugation of p-SCN-Bn-NODAGA chelator does not show any significant morphological alterations either.

4.2.1.5 XPS

XPS served as the main technique for the confirmation of APTES grafting. Spectra of the 44-µm unmodified samples were not obtained under XPS due to the initially limited access to the technique. Only two 44-µm and 2.2-µm modified samples were preliminarily provided to the operator. Continuation with XPS evaluations only took place later, when the 44-µm samples had already been discontinued by complementary results (e.g. radiolabeling). NODAGA-APTES functionalized 2.2-µm particles were also evaluated under XPS.

All spectra were calibrated with respect to the C sp^2 band (184.5 eV), detectable in any XPS measurement. Results are fitted to Gaussian curves for the detection of multiple peak contributions to the overall band profiles.

High resolution C_{1s} spectra of the adhesive support film used for the preparation of the samples as well as of 44-µm and 2.2-µm functionalized borosilicates can be found in **Figure 23**. High resolution N_{1s} and O_{1s} spectra of the same samples are recorded in **Figure 24** and **Figure 25**, respectively. S_{2s} and S_{2p} spectra were exclusively measured for 2.2-µm functionalized microparticles, and these can be found along **Figure 26**. The peaks observed on all of these spectra have been transcripted into **Table 8**.

The adhesive support used for the preparation of the samples was only evaluated to eliminate it as a possible contamination source, due to the polyimide-based nature of Kapton film. Evaluation of the O_{1s} and C_{1s} spectra have been directly associated with that recorded in the literature for Kapton® film.[89]

Despite the polyimide nature of the support, the recorded spectra confirm that no nitrogen peaks can be observed from it. Nitrogen peaks born from the polyimide are most likely undetected due to the coating provided by the adhesive system, which based of cured silicone. It is also possible that nitrogen content of Kapton® is low enough not to be detected by XPS. The lack of detectable nitrogen signals confirms that nitrogen observed in any of the analyzed samples will not be originated from the support.[90]

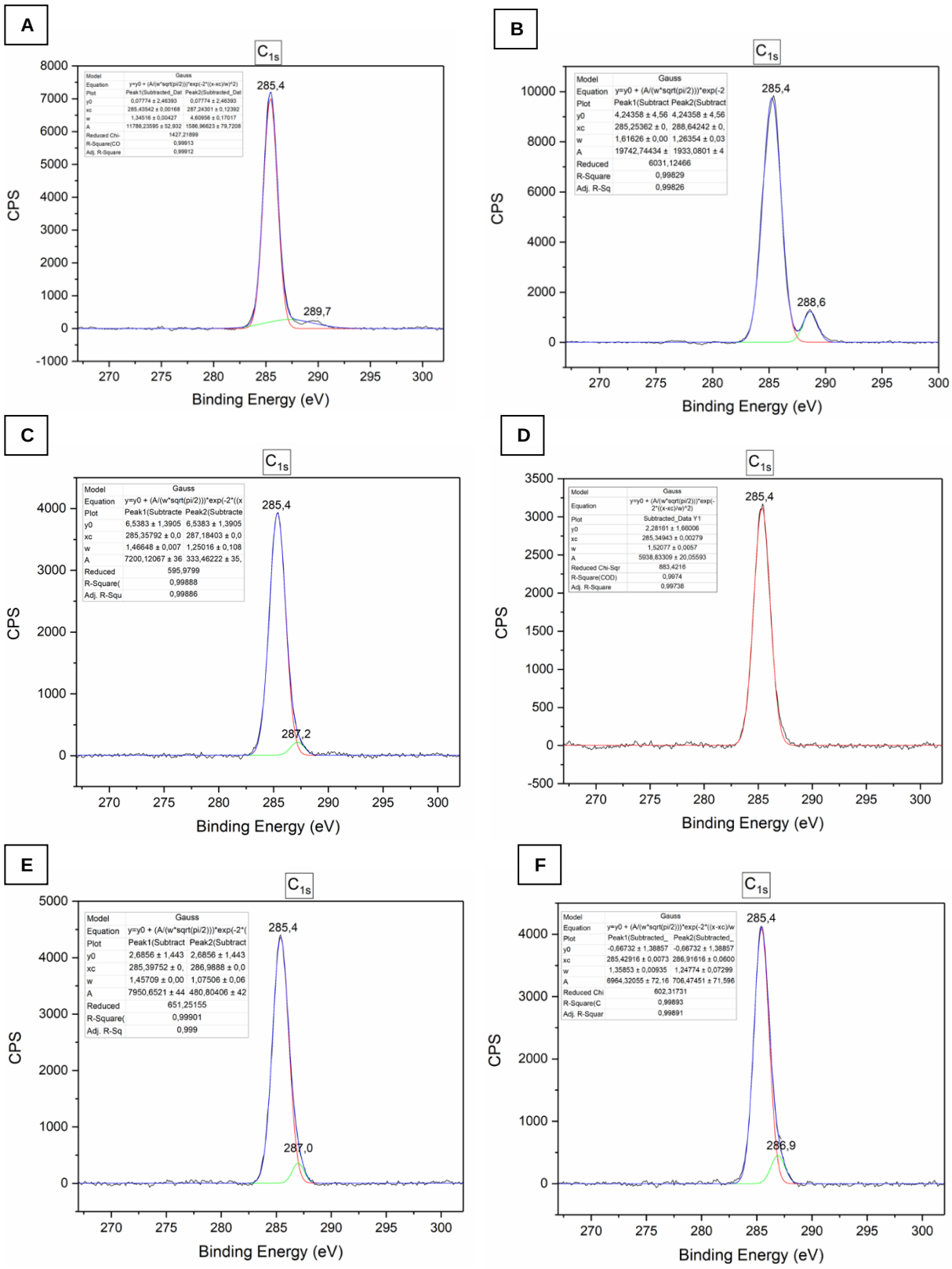

Figure 23. High resolution XPS C_{1s} spectra. (A) Adhesive layer of the Kapton® film. (B) APTES (1 mM) functionalized 44-µm borosilicate microparticles. (C) Unmodified, (D) HCl cleaned, (E) APTES and (F) NODAGA-APTES functionalized 2.2-µm borosilicate microparticles.

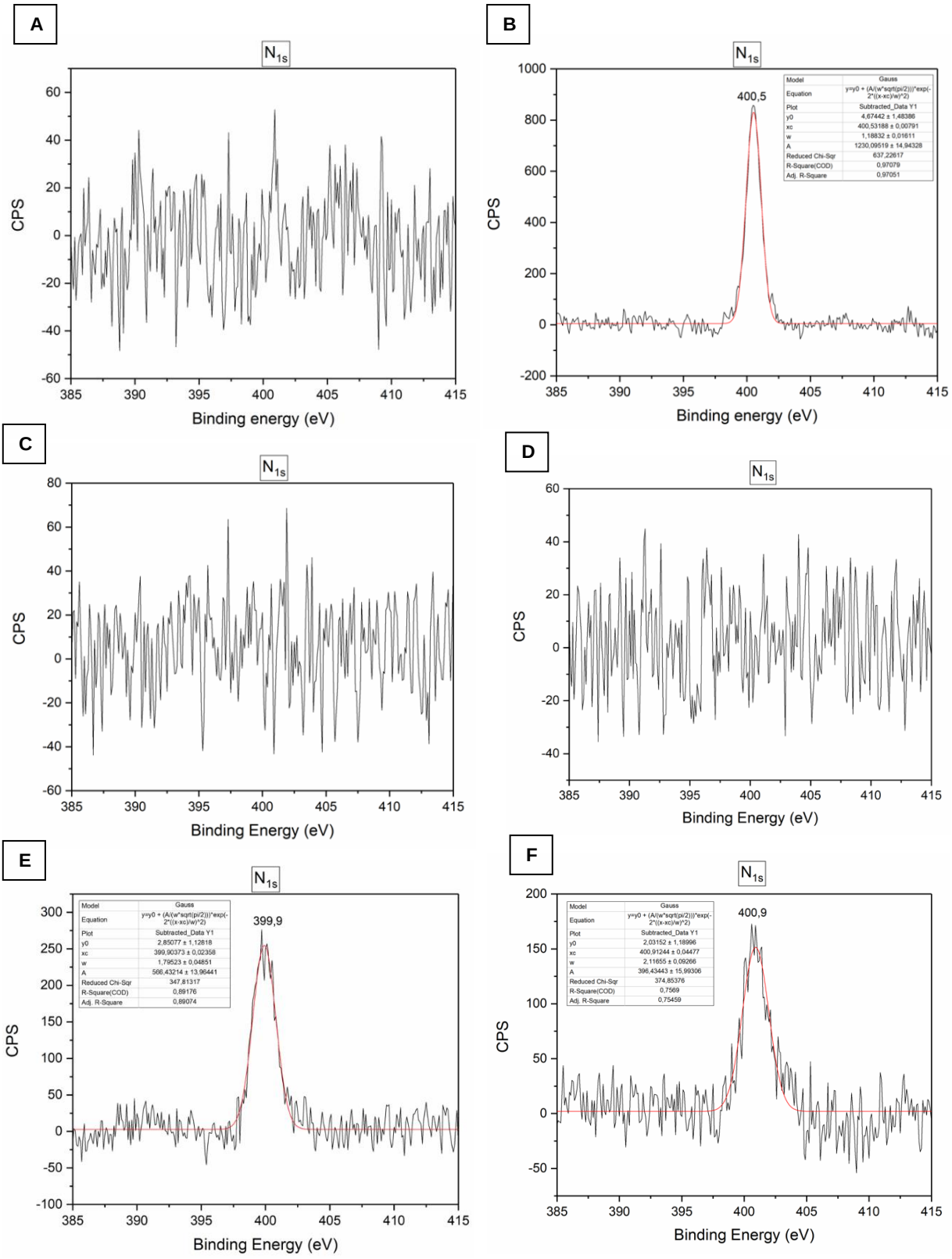

Figure 24. High resolution XPS N_{1s} spectra. (A) Adhesive layer of the Kapton® film. (B) APTES (1 mM) functionalized 44-µm borosilicate microparticles. (C) Unmodified, (D) HCl cleaned, (E) APTES and (F) NODAGA-APTES functionalized 2.2-µm borosilicate microparticles.

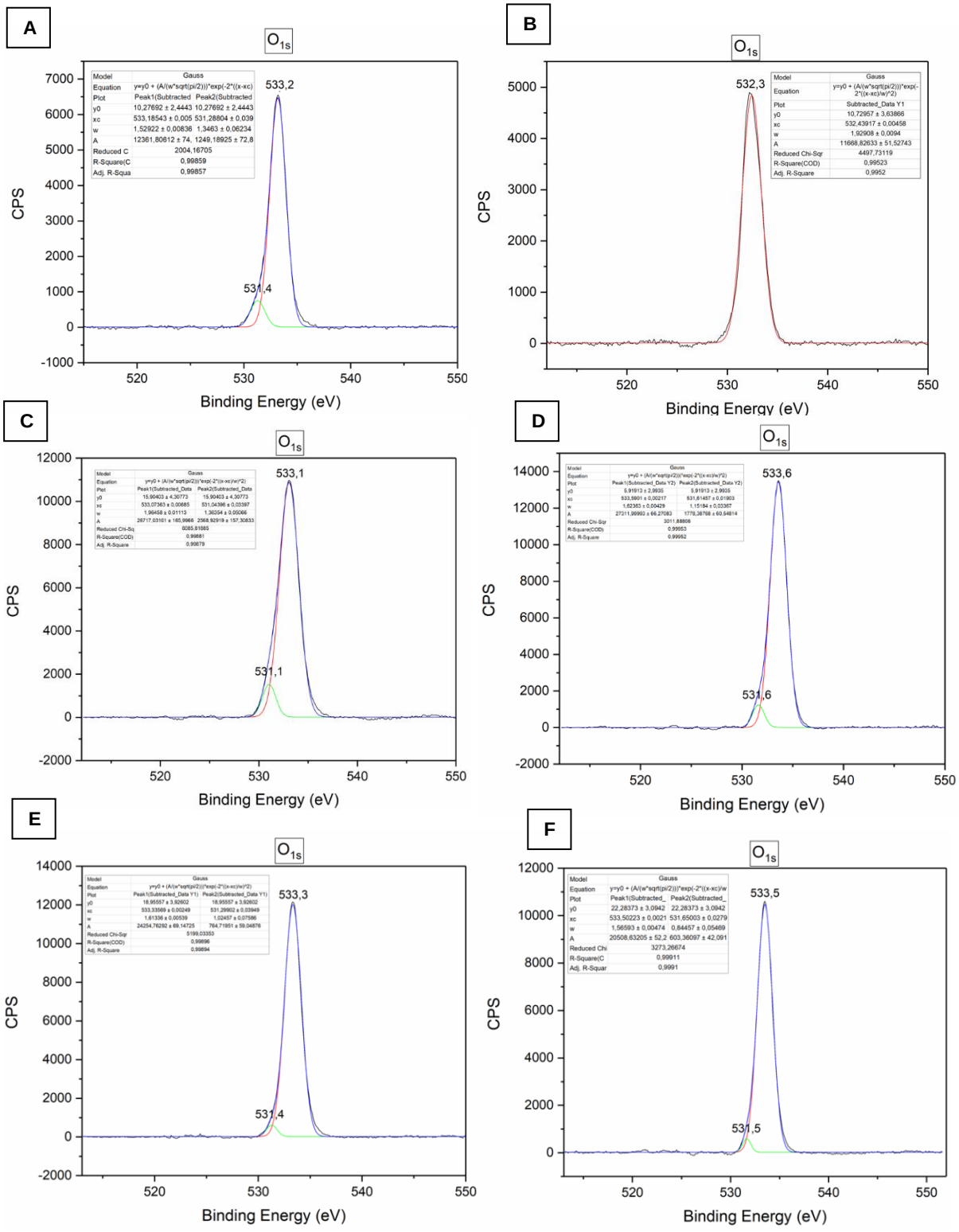

Figure 25. High resolution XPS O_{1s} spectra. (A) Adhesive layer of the Kapton® film. (B) APTES (1 mM) functionalized 44-µm borosilicate microparticles. (C) Unmodified, (D) HCl cleaned, (E) APTES and (F) NODAGA-APTES functionalized 2.2-µm borosilicate microparticles.

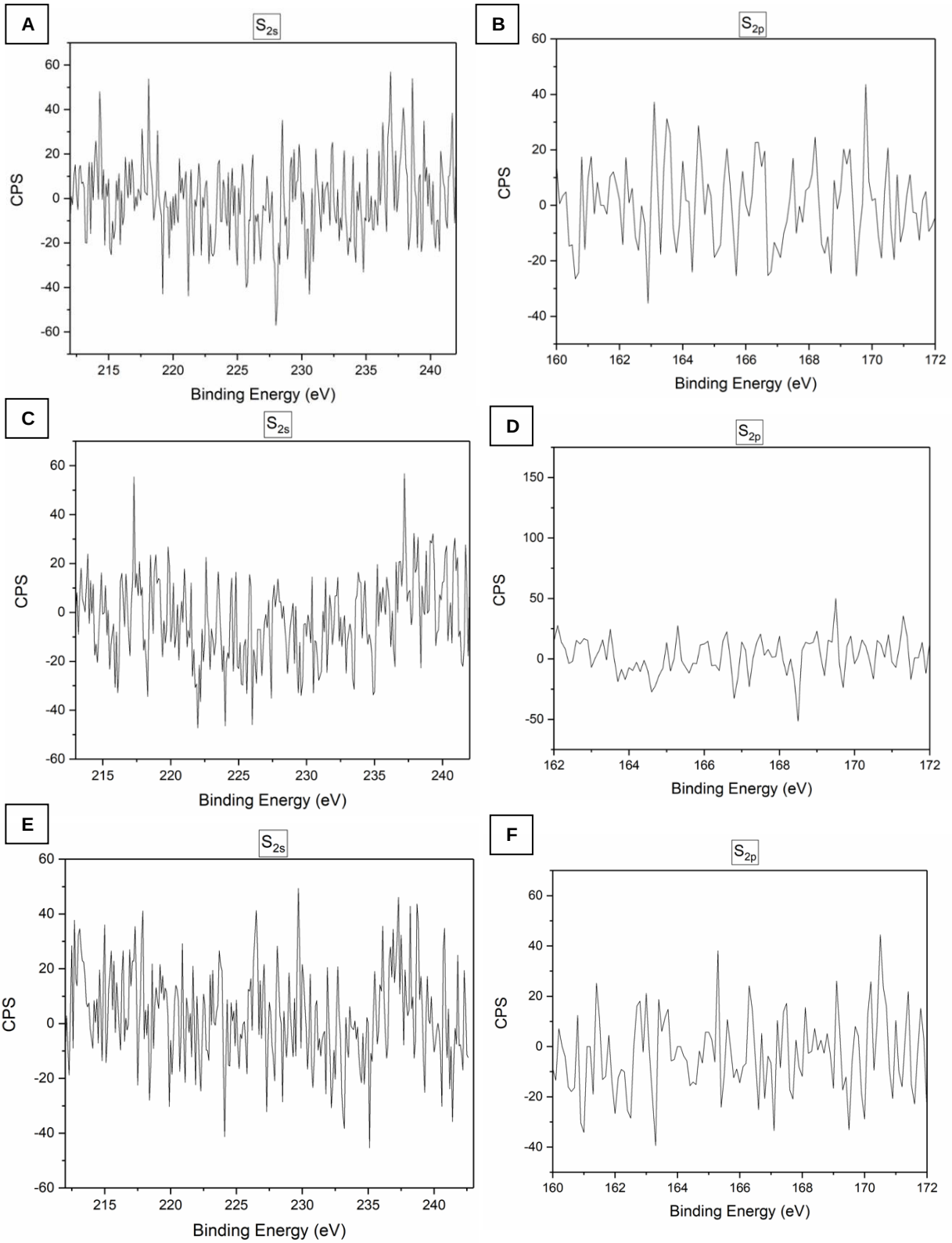

Figure 26. High resolution XPS S_{2s} (left) and S_{2p} spectra (right). (A, B) HCl cleaned, (C, D) APTES and (E, F) NODAGA-APTES functionalized 2.2-µm borosilicate microparticles.

Table 8. Peak assignation for the bands observed in the high resolution XPS C_{1s}, N_{1s}, O_{1s}, S_{2s}, and S_{2p} spectra. Adhesive layer of the Kapton® film. APTES (1 mM) functionalized 44-µm borosilicate microparticles. Unmodified, HCl cleaned, APTES and NODAGA-APTES functionalized 44-µm borosilicate microparticles.

High resolution XPS spectra of C_{1s}				
	Adhesive layer			
Peak assignation	Binding Energy (eV)			
C sp^2	285.4			
C=O	289.7			
	44-µm borosilicate microparticles			
	APTES (1 mM)			
Peak assignation	Binding Energy (eV)			
C sp^2	285.4			
C=O	288.6			
	2.2-µm borosilicate microparticles			
	Unmodified	HCl cleaned	APTES	NODAGA-APTES
Peak assignation	Binding Energy (eV)			
C sp^2	285.4	285.4	285.4	285.4
C-O	287.2	-	287.0	286.9

High resolution XPS spectra of N_{1s}				
	44-µm borosilicate microparticles			
	APTES (1 mM)			
Peak assignation	Binding Energy (eV)			
NH_2/NH_3^+	400.5			
	2.2-µm borosilicate microparticles			
	Unmodified	HCl cleaned	APTES	NODAGA-APTES
Peak assignation	Binding Energy (eV)			
NH_2/NH_3^+	-	-	399.9	-
NH_2/Tertiary amine/NH_3^+	-	-	-	400.9

High resolution XPS spectra of O_{1s}				
	Adhesive layer			
Peak assignation	Binding Energy (eV)			
O-C-O	531.4			
C=O	533.2			
	44-µm borosilicate microparticles			
	APTES (1 mM)			
Peak assignation	Binding Energy (eV)			
Si-O	532.3			
	2.2-µm borosilicate microparticles			
	Unmodified	HCl cleaned	APTES	NODAGA-APTES
Peak assignation	Binding Energy (eV)			
Si-O-Si/Si-O-M	531.1	531.6	531.4	531.5
Si-OH/OH	533.1	533.6	533.3	533.5

In the 44-µm APTES functionalized borosilicate, the presence of a nitrogen band becomes evident in the N_{1s} spectrum. Unfortunately, comparison with the unmodified borosilicate could not be possible due to the restricted access to the technique. Nitrogen band is recorded at 400.5 eV, which is in between with the theoretical assignation for NH_2 and NH_3^+ bands, of 399.4 eV and 401 eV, respectively, suggesting a contribution from both bands to the detected peak. Amine assignation is concordant with the exposed free amine ends of the grafted APTES molecule.[13] This represents the first direct confirmation of a successful superficial functionalization of the microparticles with APTES.

Its high resolution C_{1s} XPS spectrum illustrates an added contribution to the C sp^2 ambient band. The band at 288.6 eV is associated with C=O bonding, which is attributed to the absorption of a impurity due to absence of carbonyl groups in APTES, possibly originated upon initial washing with acetone.[91,92] O_{1s} spectrum contains an isolated peak at 532.3 eV, correspondent to Si-O bonds.[13]

The confirmation of surface functionalization for the 44-µm borosilicates was decisive in this project. This confirmation ensured that the functionalization procedure could be extrapolated to the smaller microparticles, which were the most relevant regarding their similarity in size to type A CsMPs. Optimization of the experimental functionalization procedure for the 2.2-µm borosilicates was based on this result: APTES (1 mM) was successfully grafted into the larger particles, therefore a slightly higher APTES (2 mM) concentration would ensure the functionalization of the smaller borosilicates. XPS became the most relevant technique for the characterization of the microparticles based on this prospect.

Evaluation of the 2.2-µm microparticles under XPS therefore becomes crucial. Their high resolution C_{1s} spectra illustrate a small C-O contribution present in both APTES and NODAGA-APTES peaks. This could be associated to the three ethoxy bonds present in the APTES molecule. This band somehow seems to be more intense in the NODAGA-APTES functionalized particle, which could be associated with an increased number of C-O bonds from the carboxylic acids present in the molecule. However, the absence of confirming C=O bands becomes detrimental for this affirmation.[91,92]

A very weak C-O contribution can be also observed in the unmodified sample.[91,92] This has been associated to a minimal contamination with ethanol during

the preparation of the samples. However, C-O bonding is not observed in the HCl cleaned borosilicate, which serves as the real precursor for the later functionalized samples. In conclusion, successful APTES functionalization cannot be confirmed only with C1s spectra, as observed C-O band could also be attributed to ethanol absorption used during the washing steps.

However, APTES functionalization becomes evident in high resolution N_{1s} XPS spectra of NODAGA-APTES and APTES functionalized samples. Neither of HCl or unmodified precursors show nitrogen traces, confirming that detected peaks correspond to NH_2 groups. The binding energy of the band recorded for the APTES functionalized borosilicate is correspondent free NH_2 groups from grafted APTES, although a small contribution from protonated NH_3^+ could be considered as previously discussed for the 44-µm borosilicate. [12,13]

A small but clear deviation of the nitrogen band in the NODAGA-APTES functionalized sample could be possibly attributed to the appearance of a tertiary amine in the NODAGA moiety, associated around 400 eV.[93] Nevertheless, it may also be built from a joint contribution of NH_2 and protonated NH_3^+ groups.[13]

All recorded high resolution O_{1s} spectra present the same profile composed of two vibration bands. The band recorded at about 533.3 eV corresponds to hydroxyl bonds, presented along the surface of the borosilicates by the silanol groups.[12,13] The band centered at about 531.5 eV is characteristic of the silica moiety, which is associated to a mixture of Si-O-Si and Si-O-Metal (M) bonds presenting oxygen bridges, with the cations present in the matrix of the borosilicate, as has been recorded for Si-O-Mg interactions in silica.[12,13,94,95] A somewhat constant binding energy value for all samples indicates that no significant changes can be appreciated in the silica matrix.

Detection of sulphur under XPS was initially planned to confirm the grafting of the NODAGA moiety into the surface of the altered microparticles through the formation of a thiourea upon reaction with the free amine ends from APTES. However, no trace of sulphur can be seen in any of the spectra recorded, for either the NODAGA-APTES functionalized sample or its precursors. Confirmation of NODAGA grafting will be assessed through radiolabeling of the final precursor.

Functionalization with APTES can therefore be confirmed for the surface modified samples, as initially expected throughout the aims of this work.

4.2.1.6 Elastic Recoil Detection Analysis (ERDA)

ERDA provides an estimation of the atomic composition of analyzed samples. The use of this technique was suggested in order to support XPS evaluations. Atomic composition and depth profiles of unmodified and APTES functionalized 44-µm and 2.2-µm borosilicates can be observed in **Table 9**. APTES concentration of the 44-µm particles was of 1 mM. NODAGA-APTES was also measured for the 2.2-µm borosilicates.

Table 9. ERDA results. Atomic composition of supporting film, Unmodified and APTES functionalized 44-µm borosilicate particles.

	44-µm borosilicate microparticles		
	Ashesive support film	Unmodified	APTES (1 mM)
Element	Concentration (at%)		
C	22.16 ± 0.18	0.29 ± 0.01	8.13 ± 0.12
O	20.88 ± 0.16	62.20 ± 0.23	54.70 ± 0.26
H	31.22 ± 0.21	1.96 ± 0.06	5.77 ± 0.13
N	0.10 ± 0.01	0.12 ± 0.01	0.59 ± 0.04
B	< 0.12	3.20 ± 0.07	2.77 ± 0.08
Na	< 0.05	1.80 ± 0.05	1.40 ± 0.05
Ca	< 0.04	0.12 ± 0.00	0.08 ± 0.00
Si	25.43 ± 0.17	30.32 ± 0.15	26.55 ± 0.17

	2.2-µm borosilicate microparticles				
	Ashesive support film	Unmodified	HCl cleaned	APTES	NODAGA-APTES
Element	Concentration (at%)				
C	22.16 ± 0.18	0.61 ± 0.01	0.28 ± 0.01	1.20 ± 0.02	1.24 ± 0.02
O	20.88 ± 0.16	59.85 ± 0.22	43.87 ± 0.16	45.12 ± 0.15	47.81 ± 0.18
H	31.22 ± 0.21	0.95 ± 0.03	1.23 ± 0.03	1.51 ± 0.02	1.62 ± 0.03
N	0.10 ± 0.01	0.16 ± 0.01	0.08 ± 0.01	0.11 ± 0.01	0.11 ± 0.01
B	< 0.12	2.80 ± 0.07	0.22 ± 0.01	0.24 ± 0.01	0.28 ± 0.02
Na	< 0.05	1.10 ± 0.04	0.13 ± 0.01	0.14 ± 0.01	0.24 ± 0.02
Ca	< 0.04	8.98 ± 0.07	1.29 ± 0.03	1.36 ± 0.03	1.58 ± 0.03
Si	25.43 ± 0.17	25.54 ± 0.13	52.89 ± 0.19	50.32 ± 0.16	47.22 ± 0.18

Technically, it the adhesive support film should not be reached by the ion beam during analysis. However, it must be analyzed for assessment of a possible contaminantion source, since borosilicate powder cannot be homogeneously deposited on the film and therefore the thickness of the sample is not constant throughout.

Analysis of the adhesive support holding the borosilicate powder suggests that it may minimally contribute to the perceived nitrogen content. This value is similar to that recorded for the unmodified borosilicates, therefore it is assumed a minimal contamination of unmodified powder by either the supporting glue or by ambient contaminants.

A clear increase in the nitrogen, carbon and hydrogen content of the APTES functionalized microparticles is evident, with respect to the unmodified borosilicates, in the 44-µm microparticles. Nitrogen, carbon and hydrogen contents content are also increased upon functionalization as well in the smaller particles, although in a much smaller extent.. In addition to XPS evaluation, it can be confirmed that APTES was succesfully grafted onto the surface of the microparticles.

In the case of the smaller particles, the concentration increase observed for nitrogen is only of about 0.03% atomic percent, in contrast with the 0.50% increase recorded for the bigger particles. This can be directly attributed to the amount of surface available for functionalization, as for spherical-like particles of 44-µm and 2.2-µm of diameter that should be[1] of 2.43×10^5 μm^2, and 60.8 μm^2, respectively, which ultimately represents an important difference.

However, the increase in carbon and hydrogen content is much more evident both cases. APTES molecules only contain one amine end and a few units conforming a short hydrocarbon chain. In essence, ERDA results pose as an additional confirmation of successful particle functionalization. Fluctuations in the Si:O ratio have been the partial incidence of the ion beam on the supporting aluminium cover needed in the preparation of the sample, as reported by the operator of the technique.

An anomaly was also appreciated in the case of the 2.2-µm microparticles, as composition shifts upon acid treatment with HCl. Silicon content greatly increases, whereas boron content is recorded to be lower. This could imply a release of boron content upon acid treatment, concordant with the disappearance of the [BO_3^-] vibrations recorded in FTIR.[71]

Associated depth profiles can be found in **Figure 27** for understanding the elemental distribution along the thickness of the analyzed sample.

[1] Available surface of spherical-like particles could be estimated with the formula correspondent to the area of a sphere, Area = $4 \pi r^2$.

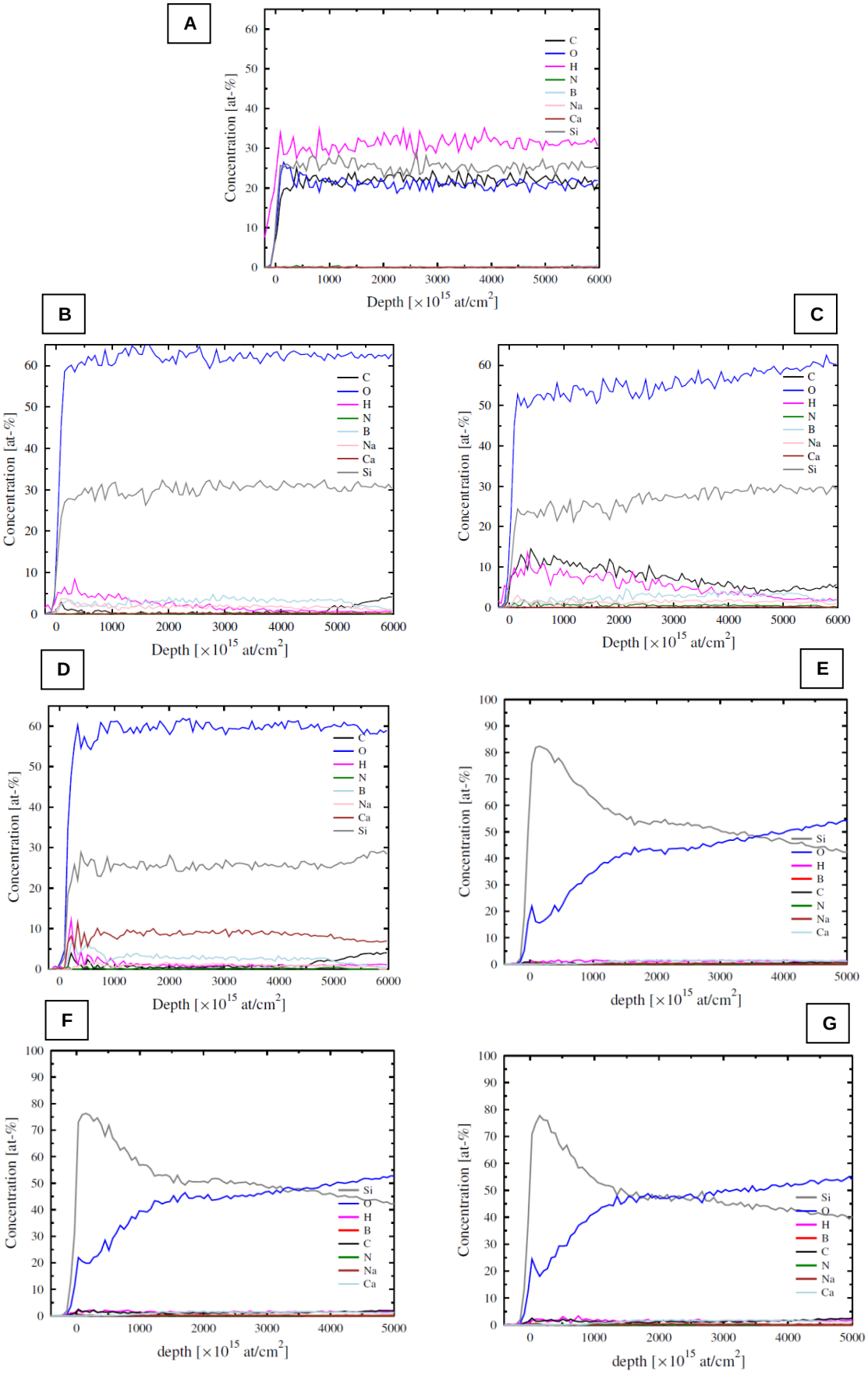

Figure 27. Atomic concentration versus depth of analyzed sample. (A) Adhesive support film. (B) Unmodified and (C) APTES (1mM) functionalized 44-µm borosilicate. (D) Unmodified, (E) HCl cleaned, and (F) APTES (and (G) NODAGA-APTES functionalized 2.2-µm borosilicate.

ERDA depht profiles demonstrate that the elemental distribution the particles is somehow uniform through the thickness of the samples in the 44-µm borosilicates. However, concentrations of carbon and hydrogen appear to be slightly decreasing with higher depth. This can be explained through the APTES functionalization process, since organic matter should be only present in the surface of the microparticles. The composition of the adhesive film remains constant throughout all of the evaluated thickness.

In the case of the the 44-µm borosilicates, an strange variation is observed in the Si:O ratio of the particles compared to that of unmodified particles. This represents an unusual situation that was accounted by the responsible operator. It is believed that the last set of samples measured by ERDA (HCl cleaned, APTES functionalized and NODAGA functionalized) records unusual readings because of interference with the aluminium support used for the preparation of the samples. Therefore, final results obtained by ERDA for the 2.2-µm functionalized microparticles are not being considered reliable.

Altogether, ERDA results in collaboration with XPS data provide a valuable confirmation of surface grafting of APTES. However, the reliability of depth profiles is strongly limited by the nature of the microparticles. Essentially, ERDA and XPS are techniques designed for the analysis of solid films. Since these are essentially packed powder supported by an adhesive film, the thickness of the samples is not homogeneous and therefore it would not be realistic to associate fluctuations in atomic concentrations with a superficial modification.

Experiments with the 44-µm borosilicate microparticles were finally discontinued at this point. This was primarily due to their radiolabeling performance, which will be discussed along the next chapters. Although the larger size of these particles was not the most appealing regarding the interests of this project, they served as ideal precursors for the optimization of reaction conditions to use with the smaller particles. The rest of the characterization techniques used for the confirmation of APTES surface functionalization were done after experiments with them were discontinued. Therefore, they will not be included in the upcoming discussion results.

4.2.1.7 Zeta potential

Surface zeta potential evaluation aimed for the examination of significant potential variations in the surface of the microparticles related to the insertion of grafting molecules.

Recorded zeta potential values of 2.2-µm APTES functionalized borosilicates can be found along **Figure 28**. Microparticles functionalized with different APTES concentrations (1 mM, 2 mM, 5 mM, 10 mM) were tested for comparison.

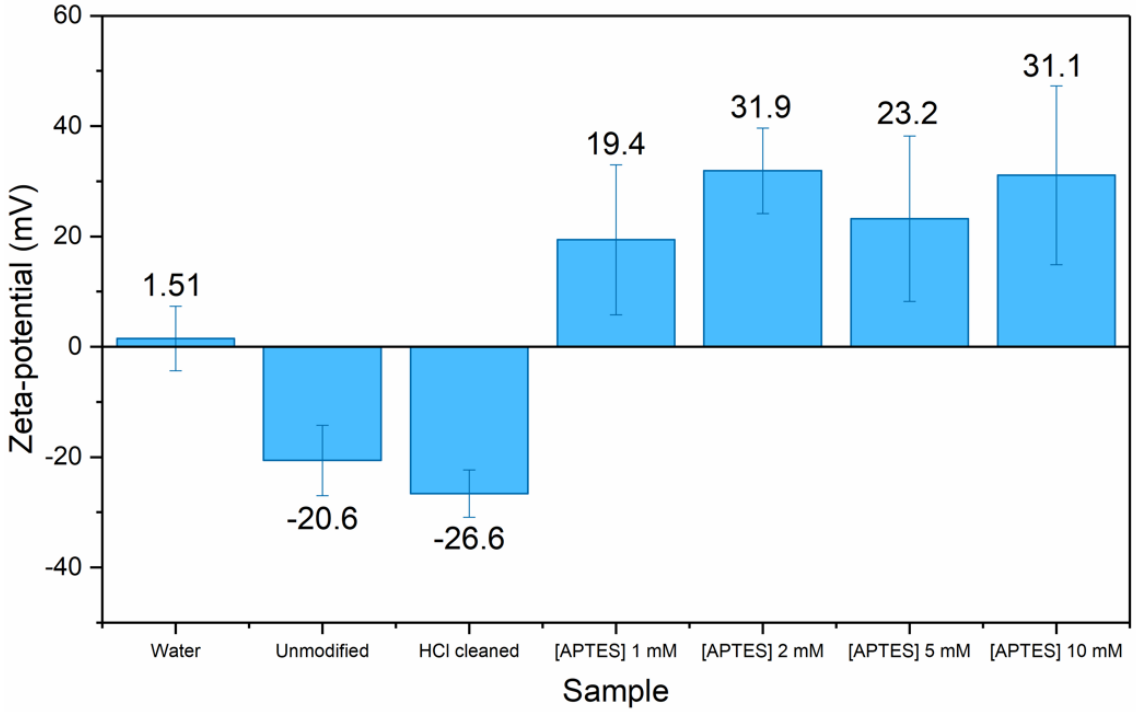

Figure 28. **Zeta potential values of APTES functionalized borosilicate particles.** Borosilicate with 2.2-µm mean diameter size.

The negative zeta potential of the unmodified sample is consistent with that observed in the literature regarding borosilicate materials. The surface of borosilicate samples is naturally negatively charged due to the presence of silanol groups. A shift to more negative potentials is evident upon activation of silanol groups through acid washing.[13]

A drastic switch to positive potential values is evident upon functionalization with APTES. This can be explained based on the superficial exposition of positively charged amine groups by the APTES molecules. Zeta potential values do not seem to directly increase with higher APTES concentrations, though a very subtle tendency

could be possibly drawn if additional grafting concentrations were to be further evaluated.[13]

APTES grafting on 2.2-µm borosilicate microparticles could be supported by zeta potential results, as the observed tendency agrees with that previously discussed in literature.[13] Dispersive behaviour of the particles fits within the theoretical instability range of -30 mV to +30 mV.[55] Unfortunately, the use of these dispersions could result in the aggregation of the particles at the bottom of the measuring cuvette forming an electrostatic gradient, which would affect the mean value of the recorded zeta potential.

4.2.1.8 Elemental analysis

Elemental analysis of surface modified borosilicates was conducted to determine the nitrogen, carbon, hydrogen, and sulphur content. Detection of these elements could confirm the grafting of APTES on 2.2-µm borosilicate microparticles. Elemental analysis was used only as a supporting technique towards the end of the project. Confirmation of APTES functionalization should mainly be based on the results provided by more sensitive techniques such as XPS.

Results obtained upon elemental analysis measurements are found listed along **Table 10**. Mean sample mass subjected to evaluation were of 1.98 ± 0.08 mg, 1.7 ± 0.5 mg and 1.9 ± 0.4 mg for unmodified, HCl cleaned and APTES functionalized borosilicate microparticles, respectively. Weight errors were obtained as the standard deviations between measured samples.

Table 10. Elemental composition of APTES functionalized borosilicate particles. Borosilicate with 2.2-µm mean diameter size. Associated errors were obtained from the recorded deviations of obtained results. Minimal error was considered to be of 0.01 % for N and C, and 0.001 % for H and S.

	2.2-µm borosilicate microparticles		
Elemental content	Unmodified	HCl cleaned	APTES
Nitrogen (%)	0.02 ± 0.01	0.02 ± 0.02	0.13 ± 0.02
Carbon (%)	0.08 ± 0.01	0.26 ± 0.10	1.1 ± 0.2
Hydrogen (%)	0.23 ± 0.01	1.59 ± 0.12	1.5 ± 0.05
Sulphur (%)	0.01 ± 0.02	0.000 ± 0.001	0.000 ± 0.001

Small differences in carbon, sulphur and hydrogen content can be observed between the unmodified and HCl cleaned borosilicates. Since acid treatment did not involve the use of any organic solvents and washing steps were just performed with deionized H_2O, the adhesion of organic traces was discarded. For this reason, the

perceived increase in hydrogen content is attributed to the absorption of H_2O by the HCl washed samples, which is also concordant with TGA evaluation. The minimal increase in carbon percentage could also be associated to moisture absorption, as it is known that ambient CO_2 dissolves in deionized H_2O. Sulphur variations were just considered measurement fluctuations. All these variations were considered to be negligible since they did not represent significant composition changes.

Evaluation of APTES functionalized borosilicates showed a clear increase in nitrogen and carbon content, of about 0.10% and 1.0%, respectively, with respect to the correspondent precursors. This is coherent with the superficial grafting of APTES organic molecules, as reported throughout the previously discussed characterization techniques. Detection of nitrogen in the functionalized particles confirms that amine end functionalization was successful. Hydrogen content remains invariant with respect to the HCl cleaned borosilicate, but it was not attributed APTES bonding as it could also be associated with the absorption of moisture.

4.2.2 Radiolabeling studies

The main idea of the thesis project was to prepare different samples for radiolabeling with gallium-68. ^{68}Ga-labeling was attempted for both APTES and PEG-ethanolamine functionalized borosilicates. The different radiolabeling experiments pursued along this work are discussed next.

4.2.2.1 Determination of radioactive parameters

As these experiments represent the main determinant for the discontinuation of some of the pursued approaches, they have been discussed according to the different conditions for the radiolabeling experiments recorded in **Table 2** from the experimental section. Said scheme is repeated again in order to clarify the sequence of experiments.

Four different ^{68}Ga-labeling experiments on APTES functionalized samples were conducted along this study, which have been denoted throughout this discussion as:

- **Experiment 1**. NODAGA-APTES 44-µm particles. Unmodified and APTES modified precursors were also evaluated.

- **Experiment 2**. NODAGA-DFO 2.2-µm particles. Unmodified, HCl cleaned and APTES modified precursors were also evaluated. Replicates were radiolabeled under the same conditions.
- **Experiment 3**. NODAGA-APTES 2.2-µm particles, washing steps with 1 × PBS. Unmodified, HCl cleaned and APTES modified precursors were also evaluated.
- **Experiment 4**. NODAGA-APTES 2.2-µm particles, washing steps with 2 mM EDTA. Unmodified, HCl cleaned and APTES modified precursors were radiolabeled as well. Several replicates were radiolabeled.

Activities values of all radiolabeled products and precursors can be found in **Table 11**, as well as its correspondent precursors. Recorded values have been decay corrected to SOS. Listed activities are those recorded for SOS and final product after purification. Results have been categorized by experiment.

Table 11. ^{68}Ga-labeling of APTES functionalized samples. Listed activity values have been recorded for SOS and final product after purification. Final activity values have been decay corrected for SOS.

	Experiment 1		
	44-µm borosilicate microparticles		
	Unmodified	APTES (2 mM)	NODAGA-APTES
Timepoint	Recorded activity (MBq)		
SOS	40.3	36.3	33.7
Final product	0.681	1.03	0.833

	Experiment 2		
	2.2-µm borosilicate microparticles		
	DFO-APTES Replicate 1	DFO-APTES Replicate 2	DFO-APTES Replicate 3
Timepoint	Recorded activity (MBq)		
SOS	23.1	19.1	38.0
Final product	2.59	0.605	0.315

	2.2-µm borosilicate microparticles		
	Unmodified	HCl cleaned	APTES
Timepoint	Recorded activity (MBq)		
SOS	19.5	19.1	19.1
Final product	2.55	1.14	0.670

	Experiment 3			
	2.2-µm borosilicate microparticles			
	Unmodified	HCl cleaned	APTES	NODAGA-APTES
Timepoint	Recorded activity (MBq)			
SOS	35.1	34.8	35.4	35.3
Final product	4.10	20.1	20.9	16.9

	Experiment 4			
	2.2-µm borosilicate microparticles			
	NODAGA-APTES Replicate 1	NODAGA-APTES Replicate 2	NODAGA-APTES Replicate 3	NODAGA-APTES Replicate 4
Timepoint	Recorded activity (MBq)			
SOS	32.2	16.6	17.3	17.2
Final product	21.7	9.83	12.2	11.2

	2.2-µm borosilicate microparticles			
	HCl cleaned Replicate 1	HCl cleaned Replicate 2	HCl cleaned Replicate 3	HCl cleaned Replicate 4
	Recorded activity (MBq)			
SOS	34.0	17.7	17.3	17.3
Final product	15.8	9.55	9.81	9.37

	2.2-µm borosilicate microparticles	
	Unmodified	APTES
Timepoint	Recorded activity (MBq)	
SOS	33.8	33.6
Final product	1.37	26.6

Continuation of **Table 11**

Radioactive parameters of the final purified radiolabeled product based on the previous data can be found along **Table 12**.

Table 12. Radioactive parameters of APTES functionalized samples. RCY values have been decay corrected for SOS. Exact weight subjected to radiofluorination has also been specified. Radioactivity concentration and A_s are recorded with respect to the activity measured at the end of synthesis.

	Experiment 1		
	44-µm borosilicate microparticles		
Parameter	Unmodified	APTES (2 mM)	NODAGA-APTES
Radioactivity concentration (MBq/mL)	0.311	0.468	0.380
RCY (%)	2	3	2
A_s (MBq/mg)	0.367	0.553	0.494
Radiolabeled product (mg)	1.1	1.1	1.0

	Experiment 2		
	2.2-µm borosilicate microparticles		
Parameter	DFO-APTES Replicate 1	DFO-APTES Replicate 2	DFO-APTES Replicate 3
Radioactivity concentration (MBq/mL)	0.786	0.087	0.419
RCY (%)	11	3	1
A_s (MBq/mg)	1.9	0.650	0.335
Radiolabeled product (mg)	0.6	0.2	0.2

	2.2-µm borosilicate microparticles		
	Unmodified	HCl cleaned	APTES
Parameter	Recorded activity (MBq)		
1.70	0.366	0.164	0.096
13	6	4	13
2.55	0.549	0.492	0.240
1.0	0.5	0.6	1.0

	Experiment 3			
	2.2-µm borosilicate microparticles			
Parameter	Unmodified	HCl cleaned	APTES	NODAGA-APTES
Radioactivity concentration (MBq/mL)	1.27	6.22	6.47	5.17
RCY (%)	12	58	60	48
A_s (MBq/mg)	1.35	6.22	6.47	5.17
Radiolabeled product (mg)	1.4	1.5	1.5	1.5

	Experiment 4			
	2.2-µm borosilicate microparticles			
Parameter	NODAGA-APTES Replicate 1	NODAGA-APTES Replicate 2	NODAGA-APTES Replicate 3	NODAGA-APTES Replicate 4
Radioactivity concentration (MBq/mL)	6.30	2.55	3.13	2.92
RCY (%)	67	59	70	65
A_s (MBq/mg)	5.91	2.55	3.13	2.92
Radiolabeled product (mg)	1.6	1.5	1.5	1.5

	2.2-µm borosilicate microparticles			
Parameter	HCl cleaned Replicate 1	HCl cleaned Replicate 2	HCl cleaned Replicate 3	HCl cleaned Replicate 4
Radioactivity concentration (MBq/mL)	4.58	2.48	2.55	2.43
RCY (%)	46	54	57	54
A_s (MBq/mg)	4.58	2.48	2.55	2.43
Radiolabeled product (mg)	1.5	1.5	1.5	1.5

	2.2-µm borosilicate microparticles	
Parameter	Unmodified	APTES
Radioactivity concentration (MBq/mL)	0.400	7.73
RCY (%)	4	79
A_s (MBq/mg)	0.400	7.73
Radiolabeled product (mg)	1.5	1.5

Continuation of **Table 12**

Regarding **Experiment 1**, results showcase that ^{68}Ga-labeling of the 44-µm microparticles is not successful. RCY is lower than 5% for both the chelator functionalized sample and its correspondent precursors. Radioactivity concentration and A_s results are all below 1 MBq/mL and 1 MBq/mg, respectively, These low activity

values would not be high enough to obtain representative PET images over time. This contradicts one of the principles of the radiopharmaceutical industry, which is to administer the lowest possible dose of compound with the highest achievable radioactivity.[30]

Studies related to the modification of the 44-μm microparticles were finally suspended at this point. It is evident that [^{68}Ga]Ga^{3+} ions are not retained by the functionalized particles and becomes lost upon the washing cycles. Based on the reviewed radiolabeling performance and particle characterization, it is suggested that chelator insertion on the 44-μm microparticles does not take place in a sufficient extent, due to APTES grafting being very limited. The use of the 44-μm microparticles was then restricted to the optimization of possible silanol activation and APTES functionalization procedures to be used on the 2.2-μm borosilicates, as previously mentioned.

With respect to **Experiment 2**, tested sets of DFO-APTES functionalized borosilicates show very different radioactivity concentration, RCY and A_s values. This is strongly associated to the amount of precursor subjected for radiolabeling. Since radiolabeling with DFO was not primarily intended for the use of ^{68}Ga, associated experiments were concluded and continued only with NODAGA functionalized borosilicates under higher reaction temperatures.

Radioactive parameters indicate that ^{68}Ga-labeling of the DFO-APTES functionalized 2.2-μm borosilicates is not successful either for the chelator modified microparticles or their precursors. Recorded RCY are still below 15% for all samples. Radioactivity concentration and A_s were again considered insufficient for stability evaluations,. This is because, since gallium-68 has a relatively low half-life (67.629*(24)* minutes)[19], products must have high enough activities before performing stability assays. Otherwise, activities after a couple of hours will be too low to provide meaningful information regarding the stability of the final product in physiological media.

The extremely low retention of gallium-68 could also be associated with the use of solutions contaminated with metallic traces. New CH_3COONa buffer and SCX eluent solutions were therefore prepared at this point to ensure the highest purity of the forthcoming experiments.

In **Experiment 3**, parameters correspondent to the unmodified borosilicate appear to be somewhat consistent with those obtained along the second experiment. However, recorded radioactivity concentration, RCY and as results of the functionalized borosilicates present higher values than those previously reported for any other radiolabeled sample. Therefore, it is understood that the HCl cleaned, APTES, and NODAGA-APTES functionalized microparticles are finally being radiolabeled.

Decay corrected RCY is of about 50–60% for all these samples. The achievable extent of the radiolabeling yields may be limited by the amount of APTES and chelator that can be possibly grafted onto the surface of the microparticles. Radioactivity concentration and A_s were considered high enough for proceeding with the stability assays.

The unusually high activity values of the HCl cleaned and APTES functionalized precursors can be associated to $[^{68}Ga]GaCl_3$ substitution of the superficial silanol groups, as has been previously observed for zeolites, which are SiO_2 based structures partially substituted with aluminium. It has been observed that $GaCl_3$ interacts with superficial silanol groups through a dichlorination reaction, forming Ga-Si-O bonds, Si(OH)Ga bridges, and framework Ga-OH groups.[96] It also has been theorized that gaseous $GaCl_3$ reacts at 205 °C with hydroxyl groups associated with aluminium, where gallium then becomes grafted as $[GaCl_2]^+$ at cation exchanged sites.[97]

No evidence has been found for $[^{68}Ga]GaCl_3$ substitution of amine groups. Therefore, APTES functionalized borosilicates are most likely radiolabeled through superficial silanol groups, as well. Nevertheless, the stability of the [^{68}Ga]Ga-O-Si bond needs to be further assessed in physiological media.

Finally, in **Experiment 4**, the mean RCY of NODAGA-APTES functionalized and HCl cleaned radiolabeled products are of 65 ± 5% and 53 ± 5%, respectively. This again confirms that radiolabeling of the borosilicate particles takes place upon $[^{68}Ga]GaCl_3$ reaction with superficial silanol groups. Retention of $[^{68}Ga]Ga^{3+}$ is increased in the former sample due to NODAGA complexation with $[^{68}Ga]Ga^{3+}$ ions. Radioactivity concentration and A_s were again considered high enough for stability assays.Similar results as those previously recorded in the third experiment have been obtained for the unmodified borosilicates, indicating that these cannot be radiolabeled

due to lower exposed silanol groups prior washing with HCl. APTES functionalized borosilicates have not been studied as extensively, since their radiolabeling had been mainly explained through [^{68}Ga]$GaCl_3$ interaction with exposed silanol groups.

In conclusion, it can be confirmed that the radiolabeling of HCl cleaned, APTES and NODAGA-APTES functionalized borosilicates takes place successfully under the studied conditions (95ºC, 15 minutes). Higher RCY could be obtained with higher reaction times, although this is not convenient for studies with ^{68}Ga due to its relatively short half-life. Stability assays need to be performed to determine the behaviour of the final product in physiological media.

4.2.2.2 Determination of RCP

The RCP of the final radiolabeled products was evaluated upon analysis of the corresponding iTLCs under autoradiography. Final values are recorded along **Table 13**.

Table 13. RCP of ^{68}Ga-labeled products. Results have been classified as for experiments. RCP of [^{68}Ga]Ga-HCl cleaned and [^{68}Ga]Ga-NODAGA-APTES were obtained as a mean based on the measurement of the four radiolabeled replicas. Mean results are also presented with their associated errors (standard deviation).

	Experiment 1			
	44-µm borosilicate microparticles			
	[^{68}Ga]Ga-Unmodified		[^{68}Ga]Ga-APTES	[^{68}Ga]Ga-NODAGA-APTES
RCP (%)	75.9		88.1	93.7
	Experiment 2			
	2.2-µm borosilicate microparticles			
	[^{68}Ga]Ga-DFO-APTES			
RCP (%)	51.4			
	Experiment 3			
	2.2-µm borosilicate microparticles			
	[^{68}Ga]Ga-Unmodified	[^{68}Ga]Ga-HCl cleaned	[^{68}Ga]Ga-APTES	[^{68}Ga]Ga-NODAGA-APTES
RCP (%)	86.8	97.1	94.1	95.7
	Experiment 4			
	2.2-µm borosilicate microparticles			
	[^{68}Ga]Ga-Unmodified	[^{68}Ga]Ga-HCl cleaned	[^{68}Ga]Ga-APTES	[^{68}Ga]Ga-NODAGA-APTES
RCP (%)	83.9	96 ± 2	96.1	94 ± 2

In **Experiment 1**, although RCP of the [^{68}Ga]Ga-NODAGA-APTES borosilicate product is found to be above 90%, previously discussed radiolabeling results indicate that the particles cannot retain a sufficient amount of radioactivity for *in vivo* administration or stability assays.

Unfortunately, in **Experiment 2**, purified versions of the radiolabeled [^{68}Ga]Ga-unmodified, [^{68}Ga]Ga-HCl cleaned and [^{68}Ga]Ga-APTES precursors could not be analyzed under iTLC. Only one replicate was succesfully evaluated under iTLC.

As seen for the measured RCP values, approximately half of the activity detected from the iTLC of the purified [^{68}Ga]Ga-DFO-APTES has been released from the radiolabeled borosilicate as unbound [^{68}Ga]Ga^{3+}. Free [^{68}Ga]Ga^{3+} is still being lost in the purified product even after three centrifugation steps.

This indicates that [^{68}Ga]Ga^{3+} ions do not coordinate with the superficially grafted DFO chelator. Although DFO is not the preferred chelator for the coordination of [^{68}Ga]Ga^{3+}, it should still retain it in an acceptable proportion. Therefore, it is possible that DFO was not successfully grafted onto the surface of the microparticles in an acceptable extent.

However, it is also likely that DFO was indeed grafted, but radiolabeling reaction conditions (15 minutes, room temperature) were not optimal for the coordination of [^{68}Ga]Ga^{3+} ions. Continuation of this worked shows that ^{68}Ga-labeling is effective when the radiolabeling reaction takes place at 95 ºC. Unfortunately, these conditions were not performed for DFO-APTES functionalized borosilicates due to time constraints.

On the contrary, all radiolabeled and purified products from **Experiment 3** present close to 95% percent of purity except for the [^{68}Ga]Ga-Unmodified borosilicate, which was the only sample that did not undergo silanol group activation upon acid washing.

RCP of the final product remains along the same levels as previously seen. Radiolabeled products are purified with only a limited [^{68}Ga]Ga^{3+} release of about 5%, except for the non-silanol activated [^{68}Ga]Ga-Unmodified borosilicate.

Finally, evaluation of RCP results show no evidence of a significant improvement in the use of EDTA instead of 1 × PBS for the washing steps is recorded. However, this was finally sustained as the most appropriate purification protocol due to the ability of EDTA for encapsulating unbound [^{68}Ga]Ga^{3+} ions.

In addition to previously discussed radiolabeling results, purified [^{68}Ga]Ga-Unmodified borosilicate, [^{68}Ga]Ga-APTES borosilicate and [^{68}Ga]Ga-NODAGA-

APTES borosilicate products show maximum retention and minimal release of [^{68}Ga]Ga^{3+}.

4.2.3 Stability assays

The stability of the final purified [^{68}Ga]Ga-NODAGA-APTES radiolabeled product obtained in radiolabeling experiments 3 and 4 was evaluated at 37 ºC over a timeframe of 0-3 h in different media simulating physiological conditions.

Physiological resembling solutions were of 1 × PBS, 50% human plasma in 1 × PBS, 0.2 mM $FeCl_3$, 2 mM EDTA and SLF. PBS is used as a buffer system for that replicates physiological media (excluding proteins) by stabilizing samples to a physiological pH, similar ionic composition, and a similar osmotic pressure in order to prevent cell rupture. Stability in donated human plasma is also necessary for stability assays of tracers directed for human studies. $FeCl_3$ is a solution simulating an increased iron content than that naturally present in the human body (10-30 × 10^{-6} M). Stability in EDTA was evaluated due to its complexing agent behaviour. SLF is a solution that simulates the chemical behaviour of fluid in the lungs.[70]

Stabilities of the [^{68}Ga]Ga-HCl cleaned, [^{68}Ga]Ga-APTES functionalized and [^{68}Ga]Ga-NODAGA-APTES purified products obtained from **Experiment 3** were studied in 1 × PBS and 50% human plasma. As for **Experiment 4**, stabilities of [^{68}Ga]Ga-HCl cleaned, [^{68}Ga]Ga-APTES and [^{68}Ga]Ga-NODAGA-APTES purified products were assessed in all five different media. From these two products, three replicates were evaluated for the former and four for the latter. Only one replica of the purified [^{68}Ga]Ga-APTES was analyzed for stability. Not all the radiolabeled replicates reported in **Table 11.** could be evaluated.

Correspondent graphs portraying the overtime stability of the products in simulated physiological media can be found along **Figure 29** and **Table 14**.

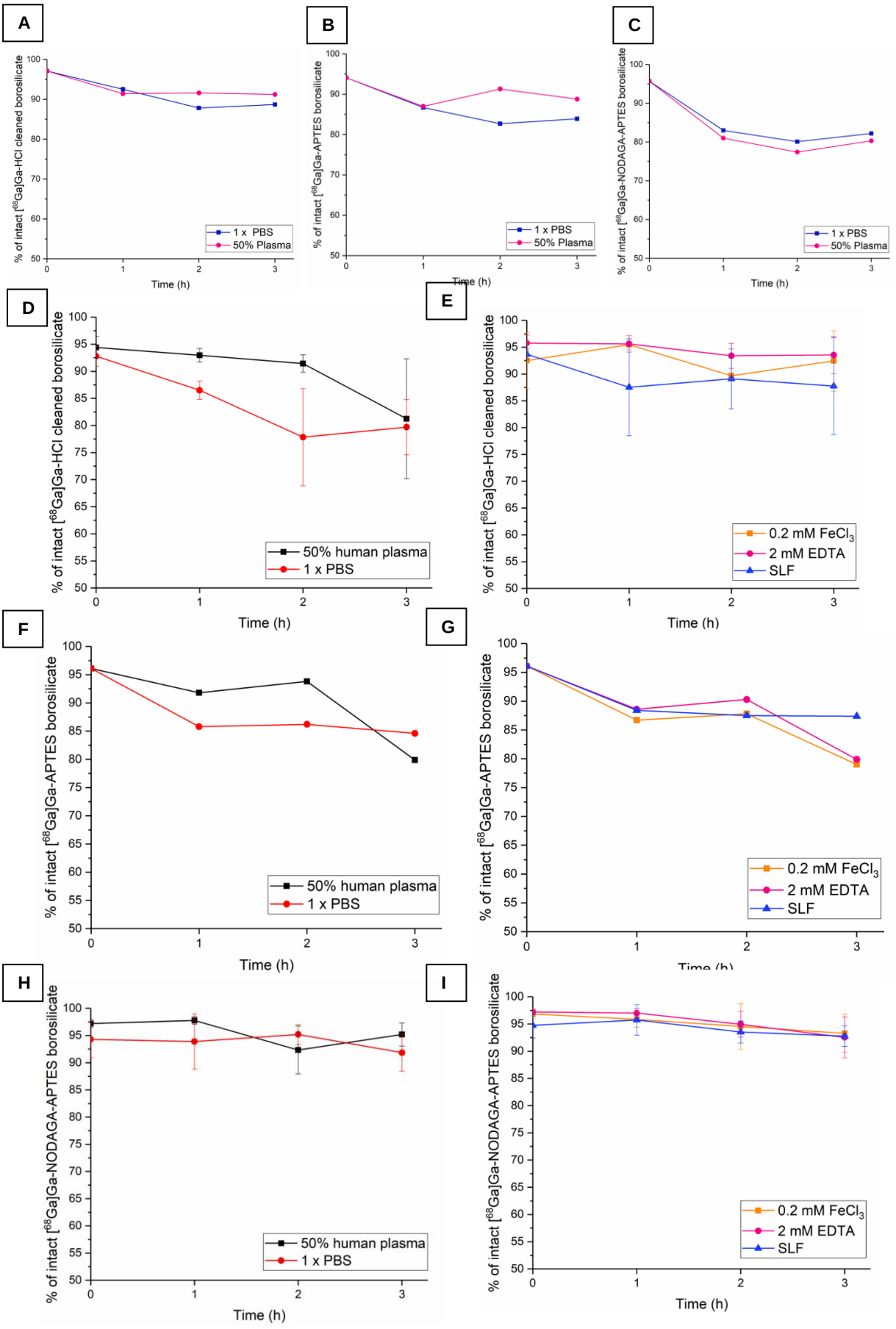

Figure 29. Stability assays over 0-3 of purified ^{68}Ga-labeled products products. (A) [^{68}Ga]Ga-HCl cleaned, **(B)** [^{68}Ga]Ga-APTES and **(C)** [^{68}Ga]Ga-NODAGA-APTES purified products from ^{68}Ga-labeling experiment 3. **(D, E)** [^{68}Ga]Ga-HCl cleaned (N=3), **(F, G)** [^{68}Ga]Ga-APTES (N=1) and **(H, I)** [^{68}Ga]Ga-NODAGA-APTES purified borosilicates (N=4) from experiment 3. N indicates the number of samples analyzed. Error bars represent the standard deviation between measurements.

Table 14. Stability assays over 0-3 of purified ^{68}Ga-labeled products. Stability assays performed in 1 × PBS, 50% human plasma, 0.2 mM $FeCl_3$, 2 mM EDTA and SLF simulated physiological media.

	Experiment 3					
	2.2-µm borosilicate microparticles					
	[^{68}Ga]Ga-HCl cleaned		[^{68}Ga]Ga-APTES		[^{68}Ga]Ga-NODAGA-APTES	
	1 × PBS	50% plasma	1 × PBS	50% plasma	1 x PBS	50% plasma
Timepoint (h)	% of intact [^{68}Ga]Ga-labeled product					
0	97.1	97.1	94.1	94.1	95.7	95.7
1	92.5	91.4	86.7	87	83	81
2	87.8	91.6	82.7	91.3	80.1	77.4
3	88.7	91.2	83.9	88.8	82.2	80.3

	Experiment 4				
	2.2-µm borosilicate microparticles				
	[^{68}Ga]Ga-HCl cleaned				
	50% human plasma	1 × PBS	0.2 mM $FeCl_3$	2 mM EDTA	SLF
Timepoint (h)	% of intact [^{68}Ga]Ga-HCl cleaned borosilicate				
0	94 ± 2	93 ± 2	93 ± 5	96 ± 1	94 ± 1
1	93 ± 1	87 ± 2	95.5 ± 0.9	96 ± 2	88 ± 9
2	91 ± 2	78 ± 9	89.7 ± 0.5	93 ± 2	89 ± 6
3	81 ± 11	80 ± 5	92 ± 6	94 ± 3	88 ± 9

	2.2-µm borosilicate microparticles				
	[^{68}Ga]Ga-APTES				
	50% human plasma	1 × PBS	0.2 mM $FeCl_3$	2 mM EDTA	SLF
Timepoint (h)	% of intact [^{68}Ga]Ga-APTES borosilicate				
0	96.1	96.1	96.1	96.1	96.1
1	91.8	85.8	86.7	88.6	88.4
2	93.8	86.2	87.8	90.3	87.5
3	79.9	84.6	79.0	79.9	87.4

	2.2-µm borosilicate microparticles				
	[^{68}Ga]Ga-NODAGA-APTES				
	50% human plasma	1 × PBS	0.2 mM $FeCl_3$	2 mM EDTA	SLF
Timepoint (h)	% of intact [^{68}Ga]Ga-APTES borosilicate				
0	97.2 ± 0.7	94 ± 3	96.8 ± 0.9	97.2 ± 0.4	95 ± 3
1	97.8 ± 0.7	94 ± 5	96 ± 1	97.0 ± 0.8	96 ± 3
2	92 ± 4	95 ± 2	95 ± 4	95 ± 2	94 ± 2
3	95 ± 2	92 ± 3	92 ± 3	93 ± 4	93 ± 2

Evaluation of the purified products from ^{68}Ga-labeling **Experiment 3** shows that stability in 50% plasma appears to be slightly higher in both [^{68}Ga]Ga-HCl cleaned and [^{68}Ga]Ga-APTES functionalized products. Stability of [^{68}Ga]Ga-NODAGA-APTES borosilicate is noticeably lower than for the other two samples. In all assays, stability seems to decrease rapidly with respect to the purified product (0-hour timepoint), but it does not oscillate significantly afterwards. This suggests that samples likely release non-specifically coordinated [^{68}Ga]Ga^{3+} ions upon contact with the PBS and plasma

solutions before becoming stable. Therefore, the need of using a different washing agent other than 1 × PBS is reaffirmed.

Stability of purified products from **Experiment 4** highlights the overtime instability of both [^{68}Ga]Ga-HCl cleaned and [^{68}Ga]Ga-APTES functionalized products. Low stability values are especially significant in 50% human plasma, 1 × PBS and SLF. This confirms that formed [^{68}Ga]Ga-O-Si bonds are not stable in physiological media. [^{68}Ga]Ga-APTES borosilicates are also unstable in 0.2 mM $FeCl_3$ and 2 mM EDTA, possibly due to sterically restricted interactions with the superficial silanol groups, hindered by the grafted APTES molecules.

Stability of the [^{68}Ga]Ga-NODAGA-APTES purified particles seems to be consistent over the evaluated timeframe. Although the percentage of intact product appears to be slowly decreasing with time, this remains over 92% for all of evaluated media. This represented the principal and most relevant results of this master thesis.

These results provide promising expectations for the *in vivo* administration of radiolabeled borosilicate particles upon functionalization with APTES, which could help examining their biological distribution under PET. Although the conducted study had to be stopped at this point because of time constraints, continuation of the project should be directed to the radiolabeling and stability evaluations of chelator-APTES functionalized microparticles, with PET radiometals of longer half-lives such as zirconium-89.

4.3 Surface functionalization of borosilicates with PEG-Ethanolamine

4.3.1 Characterization techniques

Discussion of experimental techniques used for the characterization of the borosilicates will be exactly as described for the APTES modifications. Results are presented in chronological order, which may differ with that previously observed for APTES functionalized samples.

4.3.1.1 FTIR

FTIR spectra and listed vibrations of associated bands can be found along **Figure 30** and **Table 15**.

Spectra of functionalized borosilicates presents the exact same vibration profile as HCl activated borosilicates. No bands corresponding to NH_2 stretching (3450 – 3300 cm^{-1}), NH_2 bending (1650 – 1400 cm^{-1}) or hydrocarbon stretching (3000 – 2900 cm^{-1}) confirming surface functionalization with ethanolamine are observed. Bands corresponding to C=O stretching (1800 – 1650 cm^{-1}) or an intensification of the O-H stretching band (3300 cm^{-1}), both related to carboxylic acid of the conjugated PEG moiety, are not observed either.[72]

Discussion of the rest of the bands of the recorded profiles is exactly as previously described under the characterization of silanol activated microparticles. In essence, FTIR does not have enough sensitivity for detecting surface functionalization with such small concentrations of ethanolamine. This therefore applies for functionalization with PEG as well.

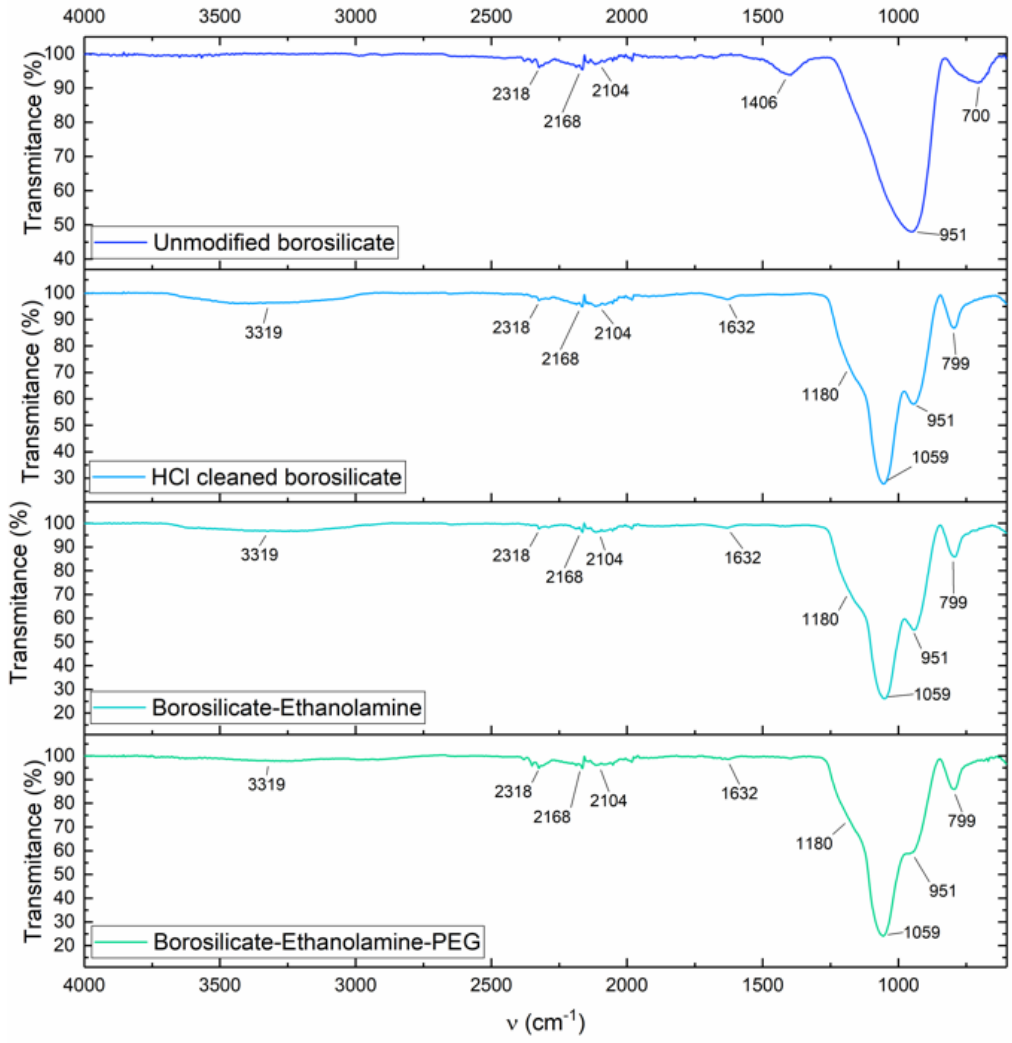

Figure 30. ATR FTIR spectra of PEG-ethanolamine functionalized borosilicates. Recorded frequency of significant vibration bands is indicated with an arrow. Borosilicate with 2.2-µm mean diameter size.

Table 15. Assignation of FTIR band vibrations observed along associated FTIR spectra. Symbols "ν" and "δ" represent stretching and bending vibrations, respectively. Borosilicate with 2.2-µm mean diameter size.

		2.2-µm borosilicate microparticles			
Vibration mode	Band intensity	Unmodified	HCl cleaned	Ethanolamine	PEG-Ethanolamine
		Frequency (cm^{-1})			
ν(Si-OH)	Medium	799	799	799	799
ν(Si-O-Si)	Intense	951	951	951	951
$\nu(Si\text{-}O\text{-}Si)_{as}$, $\nu[BO_4]$	Very intense	1059	1059	1059	1059
ν(Si-O-Si)	Medium	1180	1180	1180	1180
δ(O-H)	Very weak	1632	1632	1632	1632
Glass matrix	Weak	2104	2104	2104	2104
Glass matrix	Weak	2168	2168	2168	2168
Glass matrix	Weak	2318	2318	2318	2318
ν(O-H), ν(Si-OH)	Weak *(broad)*	3319	3319	3319	3319

4.3.1.2 TGA

TGA results of ethanolamine functionalized 2.2-µm borosilicate particles can be found along **Figure 31** and **Table 16**.

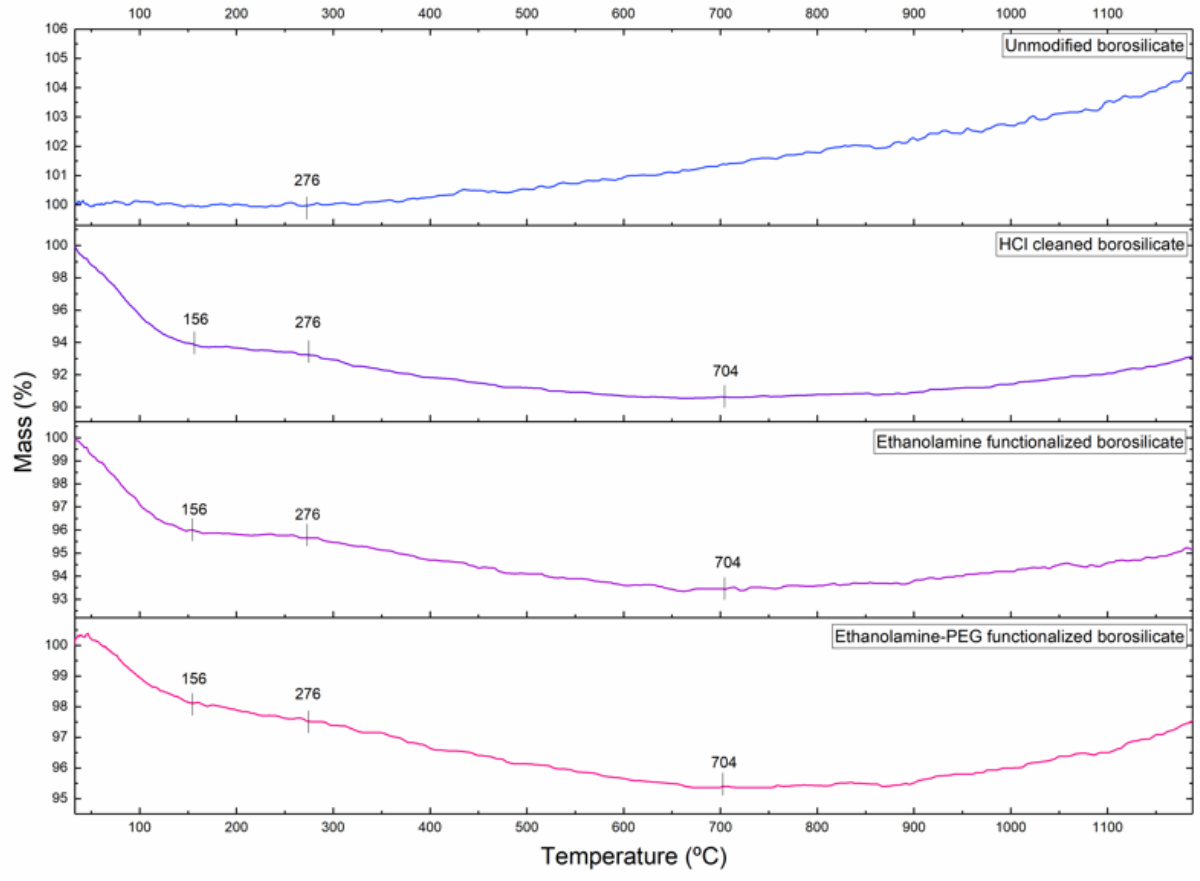

Figure 31. TGA profiles of ethanolamine functionalized borosilicate particles. Borosilicate with 2.2-µm mean diameter size.

Table 16. Assignation of TGA steps from PEG-Ethanolamine functionalized microparticles. Borosilicate with 2.2-µm mean diameter size.

2.2-µm borosilicate microparticles				
Unmodified				
Stage name	Temperature range (ºC)	Percentage range of weight loss (%)	Net percentage of weight loss (%)	Assignation
Step 1	25 – 356	100.00 – 100.5	-0.5	Stability range
Step 2	356 – 1200	100.5 – 104.9	-4.4	Sample oxidation
HCl cleaned				
Stage name	Temperature range (ºC)	Percentage range of weight loss (%)	Net percentage of weight loss (%)	Assignation
Step 1	25 – 156	100.0 – 93.9	6.1	Moisture release
Step 2	156 – 276	93.9 – 93.2	0.7	Stability range
Step 3	276 – 704	93.3 – 90.6	2.7	Glass transition
Step 4	704 – 1200	90.6 – 92.9	-2.3	Sample oxidation
Ethanolamine				
Stage name	Temperature range (ºC)	Percentage range of weight loss (%)	Net percentage of weight loss (%)	Assignation
Step 1	25 – 156	100.0 – 96.0	4.0	Moisture release
Step 2	156 – 276	96.0 – 95.7	0.3	Stability range
Step 3	276 – 704	95.7 – 93.4	2.3	Glass transition
Step 4	704 – 1200	93.4 – 95.1	-1.7	Sample oxidation
PEG-Ethanolamine				
Stage name	Temperature range (ºC)	Percentage range of weight loss (%)	Net percentage of weight loss (%)	Assignation
Step 1	25 – 156	100.0 – 98.2	1.8	Moisture release
Step 2	156 – 276	98.2 – 97.5	0.7	Stability range
Step 3	276 – 704	97.5 – 95.4	2.1	Glass transition
Step 4	704 – 1200	95.4 – 97.6	-1.9	Sample oxidation

Recorded TGA profiles and are identical to those previously evaluated for the APTES functionalized 2.2-µm borosilicate particles. Discussion of these spectra is therefore identical to that previously elaborated. In conclusion, the observed invariant profiles between analyzed samples indicate that no effect can be observed upon superficial functionalization with PEG-Ethanolamine. This again confirms that TGA is not a suitable technique for the determination of molecule grafting onto the surface of the studied synthetic borosilicates.

4.3.1.3 Zeta potential

Zeta potential values PEG-Ethanolamine functionalized borosilicates can be found along **Figure 32**.

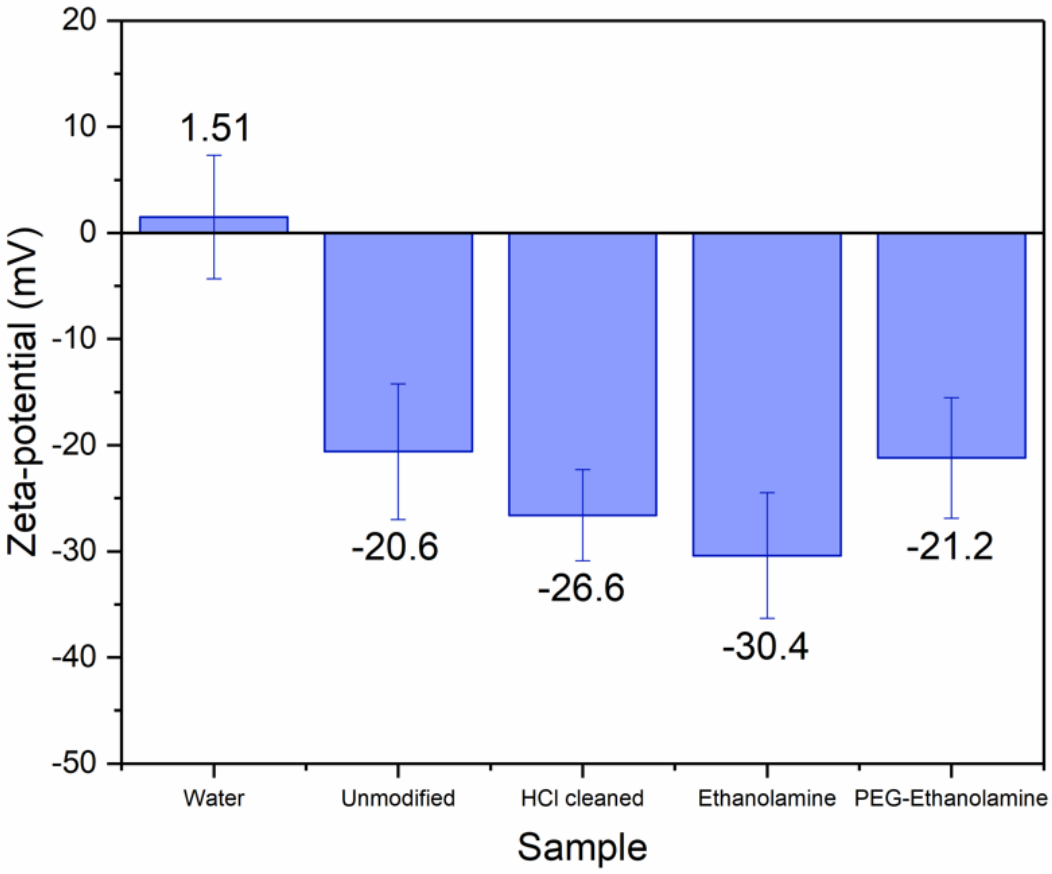

Figure 32. Zeta potential values of ethanolamine functionalized borosilicate particles. Borosilicate with 2.2-µm mean diameter size.

Functionalization with ethanolamine hydrochloride seemed to decrease the value of measured zeta potential. According to literature, this could be due to amine groups reacting with the surface of the borosilicates, exposing free hydroxyl groups from ethanolamine instead.[13] However it is more likely that functionalization with ethanolamine cannot be confirmed with the sensitivity of the technique.

Zeta potential measured for PEG-Ethanolamine functionalized particles is still negative, in agreement with research studies regarding superficial PEG coverage of negatively charged particles.[98] Nevertheless, the measured potential value is less negative than that recorded for ethanolamine functionalized borosilicates. Theoretically, the observed zeta potential of these modified samples should be even lower due to the negatively charged free carboxylic acid ends exposed by the PEG chains. Since the associated error for both ethanolamine and PEG-ethanolamine measurements falls between a common range, this mild deviation could be attributed to an instrumental error. It is also possible that the concentration of carboxyl groups

in the surface of the microparticles is not high enough for the associated instrument to detect a significant variation of the zeta potential.

The maintained negative potential of the measured samples with respect to the unmodified and HCl cleaned synthetic borosilicates represents an ideal scenario, where modifications do not cause a significant alteration of the superficial potential of the particles. On the other hand, it could also imply that the functionalization process was not successful hence no significant variations are observed between measurements.

As previously mentioned, the reliability of zeta potential evaluations is strongly limited by the relative insolubility of the borosilicate particles. Therefore, the confirmation of a successful functionalization should be supported by alternative characterization techniques.

4.3.1.4 Elemental analysis

Results obtained upon elemental analysis measurement are found listed along **Table 17**. In this case, DFO-PEG-Ethanolamine functionalized sample could also be evaluated. Mean sample mass were of 1.98 ± 0.08 mg, 1.7 ± 0.5 mg, 1.8 ± 0.3 mg, 1.1 ± 0.2 mg and 0.2540 ± 0.0001 mg for unmodified, HCl cleaned, ethanolamine, PEG-ethanolamine and DFO-PEG ethanolamine functionalized borosilicates, respectively. Weight errors were obtained as the standard deviations between weighted samples. Weight error of DFO-PEG-ethanolamine functionalized borosilicate was considered as the minimal instrumental digit since only one sample was analyzed.

Table 17. Mean elemental composition of PEG-Ethanolamine functionalized borosilicate particles. Borosilicate with 2.2-µm mean diameter size. Errors were obtained from the recorded deviations of obtained results. Minimal error was considered to be of 0.01 % for N and C, and 0.001 % for H and S.

Elemental content	2.2-µm borosilicate microparticles				
	Unmodified	HCl cleaned	Ethanolamine	PEG-Ethanolamine	DFO-PEG-Ethanolamine
Nitrogen (%)	0.02 ± 0.01	0.02 ± 0.02	0.04 ± 0.01	0.17 ± 0.01	0.36 ± 0.01
Carbon (%)	0.08 ± 0.01	0.26 ± 0.10	1.1 ± 0.2	1.2 ± 0.2	11.87 ± 0.01
Hydrogen (%)	0.23 ± 0.01	1.59 ± 0.12	1.49 ± 0.05	1.54 ± 0.02	3.30 ± 0.01
Sulphur (%)	0.01 ± 0.02	0.000 ± 0.001	0.83 ± 0.03	0.000 ± 0.001	0.000 ± 0.001

A clear difference in carbon and sulphur content can be observed in the ethanolamine functionalized borosilicate. This is directly related to DMSO absorption by the samples during the reaction and washing steps. No significant nitrogen content

increase is observed upon functionalization of the particles with ethanolamine. This could indicate that the grafting of ethanolamine molecules is not an appropriate approach for the functionalization of borosilicate microparticles.

Increases in nitrogen, carbon and hydrogen content are appreciated in both PEG-ethanolamine and DFO-PEG-ethanolamine functionalized borosilicates. Since the grafted organic molecules are rich in C, H and N content, this percentage increase could suggest that they are present in the evaluated samples. Nevertheless, this would not be coherent with the previously confirmed unsuccessful functionalization with ethanolamine, as the free amine ends from the ethanolamine molecules serve as linkers for PEG and successive DFO incorporation. In essence, if no ethanolamine was grafted on the borosilicates, PEG or DFO could not be present either. It is possible that the increased content in said elements is related to an instrumental error associated with the small weight of samples subjected to analysis, or to contamination of the samples during the analytical process.

However, results obtained from evaluation under elemental analysis of the DFO-PEG-ethanolamine and PEG-ethanolamine borosilicates are not considered conclusive due to the small amount of sample analyzed, respectively of 1.1 ± 0.2 mg and 0.2540 ± 0.0001 mg. This is below the recommended amount of 2 mg suggested by the operator.

4.3.1.5 XPS

Since the spectra of the unmodified and HCl activated precursors has already been discussed for the APTES functionalized microparticles, only new spectra are included along the added figures. High resolution XPS spectra of C_{1s}, N_{1s} and O_{1s} can be found along **Figure 33**, **Figure 34**and **Figure 35**, respectively. Peak assignation of all spectra can be found along **Table 18**.

All graphs were fitted to Gaussian curves for the detection of multiple peak contributions to the overall band profile.

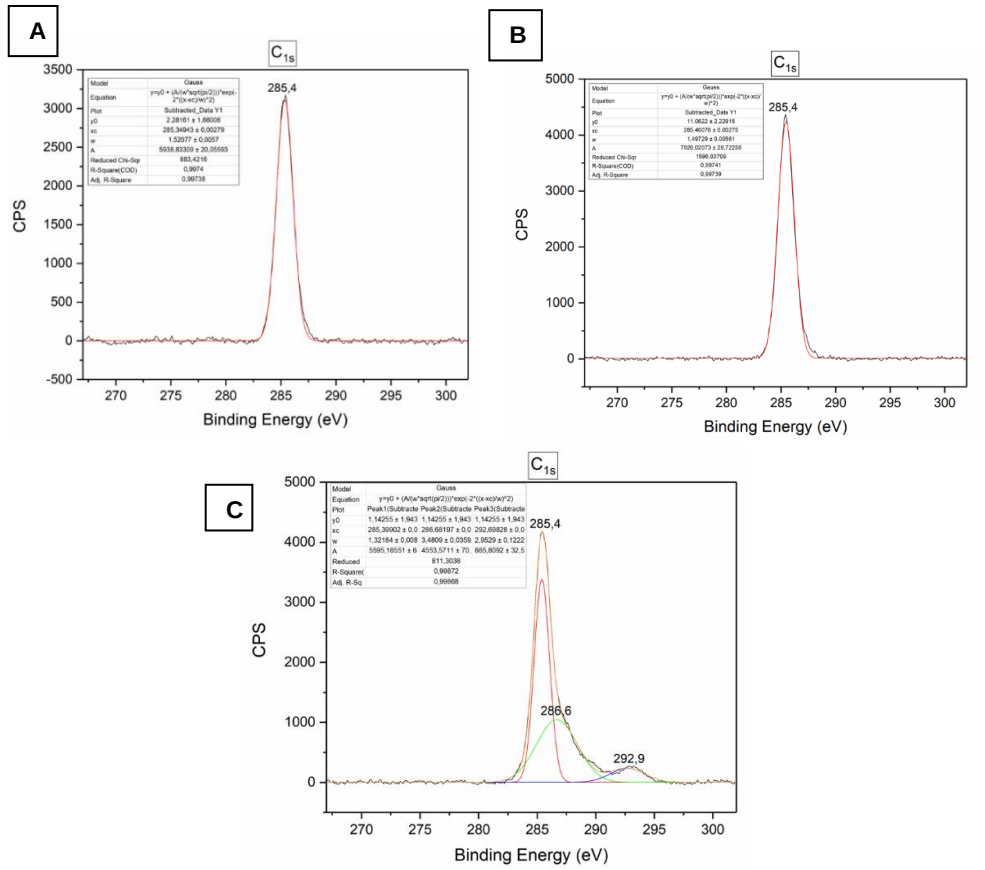

Figure 33. High resolution XPS C_{1s} spectra. (A) Ethanolamine, (B) PEG-Ethanolamine and (C) DFO-Ethanolamine 2.-µm borosilicate microparticles.

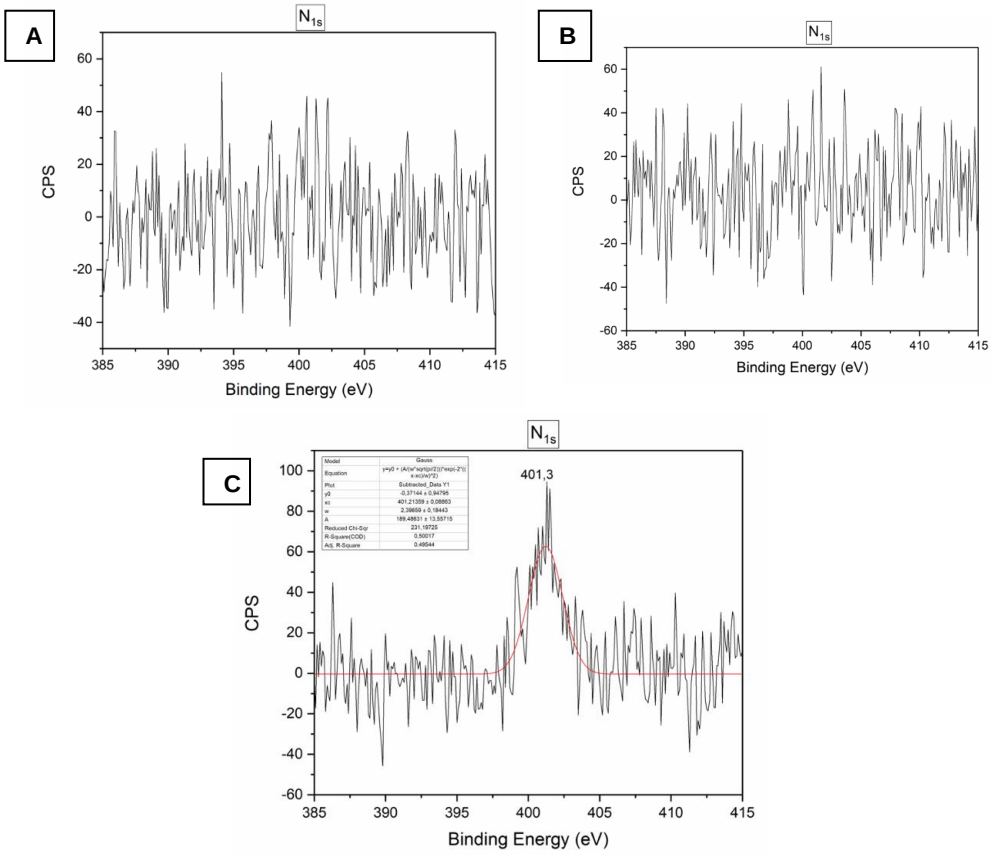

Figure 34. High resolution XPS N_{1s} spectra. (A) Ethanolamine, (B) PEG-Ethanolamine and (C) DFO-Ethanolamine 2.-µm borosilicate microparticles.

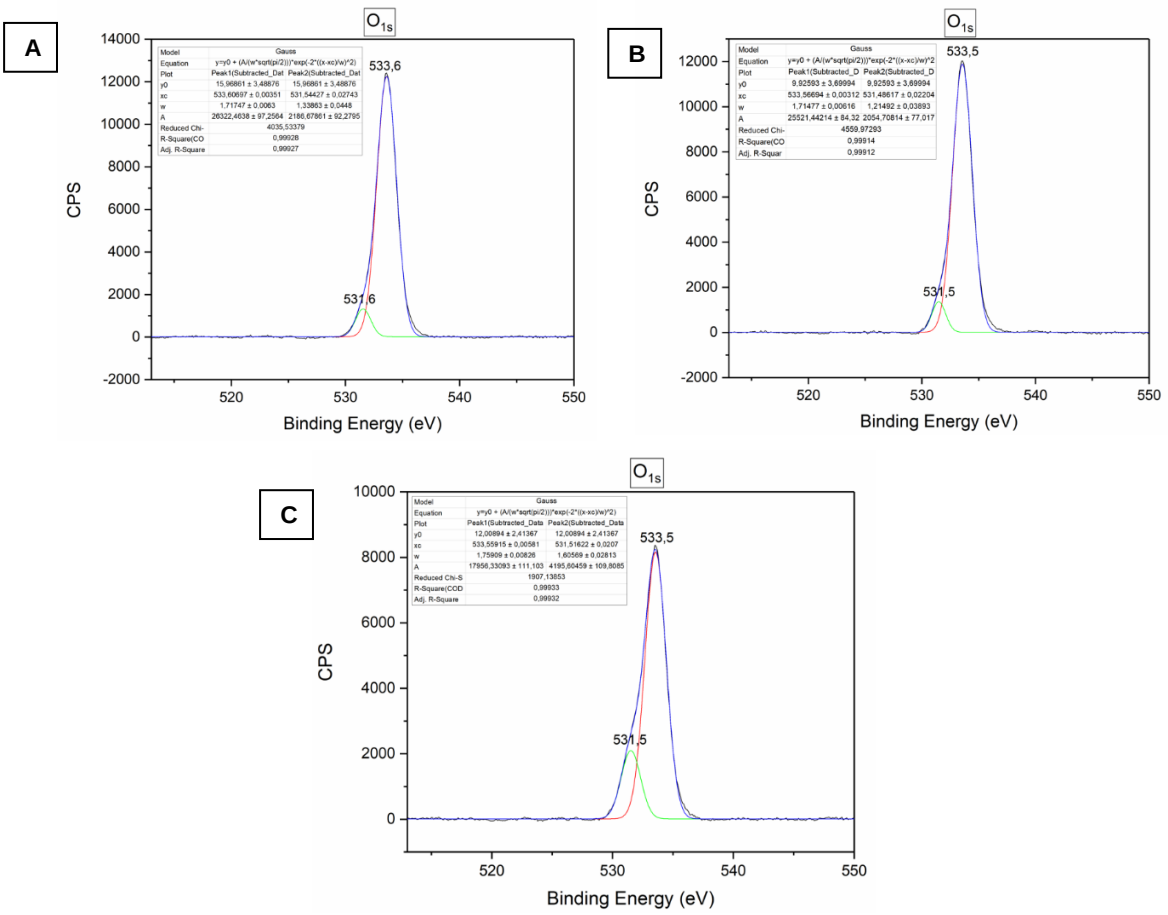

Figure 35. High resolution XPS O_{1s} spectra. (A) Ethanolamine, (B) PEG-Ethanolamine and (C) DFO-Ethanolamine 2.-µm borosilicate microparticles.

Table 18. High resolution XPS C_{1s}, N_{1s} and O_{1s} spectra. Unmodified, HCl cleaned Ethanolamine PEG-Ethanolamine and DFO-Ethanolamine 2.2-µm borosilicate microparticles.

High resolution XPS spectra of C_{1s}					
Peak assignation	2.2-µm borosilicate microparticles				
	Unmodified	HCl cleaned	Ethanolamine	PEG-Ethanolamine	DFO-PEG-Ethanolamine
	Binding Energy (eV)				
C sp^2	285.4	285.4	285.4	285.4	285.4
C-O	287.2	-	-	-	-
C=O	-	-	-	-	286.6
Satellite *(artifact)*	-	-	-	-	292.9

High resolution XPS spectra of N_{1s}					
Peak assignation	2.2-µm borosilicate microparticles				
	Unmodified	HCl cleaned	Ethanolamine	PEG-Ethanolamine	DFO-PEG-Ethanolamine
	Binding Energy (eV)				
NH_2-OH	-	-	-	-	401.3

High resolution XPS spectra of O_{1s}					
Peak assignation	2.2-µm borosilicate microparticles				
	Unmodified	HCl cleaned	Ethanolamine	PEG-Ethanolamine	DFO-PEG-Ethanolamine
	Binding Energy (eV)				
Si-O-Si/Si-O-M	531.1	531.6	531.6	531.5	531.5
Si-OH/OH	533.1	533.6	533.6	533.5	533.5

Continuation of **Table 18**

High-resolution XPS C_{1s} spectra remain the same after functionalization of the samples. C-O bonding previously observed for the APTES functionalized and unmodified particles borosilicates is now absent. . A satellite artifact possibly from the $K_{p3/2}$ band can be observed in the DFO-PEG-Ethanolamine sample.[99] Finally, a C=O band can be observed for the C=O sample, which could be associated to the carbonyl groups present in DFO. C=O band is not visible in the PEG-Ethanolamine precursor, which could be attributed to the carboxylic acids of the polymer.[91,92]

Superficial functionalization with ethanolamine is finally discontinued upon high resolution N_{1s} XPS spectra, as no traces of nitrogen can be seen on evaluated samples. A small contribution of a NH-OH band can however be observed in the DFO-PEG-Ethanolamine functionalized borosilicate. NH-OH is present in the DFO moiety, which could be associated with a successful grafting of the chelator.[12]

However, the absence of NH_2 peaks in the spectra of the associated precursors would not support this affirmation, as no DFO insertion could be possible without an initial ethanolamine functionalization. Therefore, the nitrogen band located at 401.3 eV could also be caused by tertiary amines from adsorbed DMF or DIPEA used in the synthesis of the sample.[93]

O_{1s} bands remain unchanged with respect to those previously discussed for the APTES functionalized 2.2-µm microparticles. Therefore, no change in the composition of the silica matrix of the microparticles is observed. Functionalization of the microparticles with ethanolamine and PEG was ultimately discontinued based on XPS results, which were supported by radiolabeling performance.

4.3.2 Radiolabeling studies

4.3.2.1 ^{68}Ga-labeling

Radiolabeling with gallium-68 was pursued for DFO-PEG-Ethanolamine 2.2-µm borosilicate particles. Only one ^{68}Ga-labeling experiment was performe, as previously stated along the experimental section of this thesis.

It has been previously explained that DFO is not the ideal chelator for the retention of [^{68}Ga]Ga^{3+}, compared to those derived from NOTA. Nevertheless, it can still coordinate the radiometal with an acceptable stability over time. DFO insertion on the borosilicates was mostly planned as a preliminary experiment for the 2.2-µm particles prior radiolabeling with NODAGA. DFO functionalized microparticles could then be possibly used for future radiolabeling experiments with zirconium-89, since DFO is the primary chelator used for complexation of this radiometal. Radiolabeling with zirconium-89 would ultimately provide more realistic biodistribution results thanks to the longer half-life of the radiometal.

Recorded activities for ^{68}Ga-labeling of DFO-PEG-Ethanolamine functionalized 2.2-µm particles can be found recorded along **Table *19***. Precursors were also radiolabeled for comparison.

Table 19. Activity values recorded for DFO-PEG-Ethanolamine functionalized borosilicates. Listed activity values have been recorded for SOS and final product after purification. Activity of the final product has been decay corrected with respect to SOS.

	2.2-µm borosilicate microparticles				
	Unmodified	HCl cleaned	Ethanolamine	PEG-Ethanolamine	DFO-PEG-Ethanolamine
Timepoint	Recorded activity (MBq)				
SOS	19.5	19.1	22.3	22.6	22.8
Final product	2.55	1.14	0.978	0.396	1.06

Radioactive parameters of the final purified products are listed along **Table 20**.

Table 20. Radioactive parameters of the final products. RC, RCY and A_S have been decay corrected to SOS. Exact weight subjected to radiofluorination has also been specified.

	2.2-µm borosilicate microparticles				
Parameter	Unmodified	HCl cleaned	Ethanolamine	PEG-Ethanolamine	DFO-PEG-Ethanolamine
RC (MBq/mL)	1.70	0.763	0.674	0.273	0.734
RCY (%)	13	6	4	2	5
A_S (MBq/mg)	2.55	2.29	1.63	0.660	1.77
Radiolabeled product (mg)	1.0	0.5	0.6	0.6	0.6

Results showcase that none of the samples become radiolabeled with gallium-68. Highest RCY is of 13% for the unmodified borosilicate, which should not retain [^{68}Ga]Ga^{3+} ions as no chelator was linked to their surface. Although A_s is over 1 MBq/mg for all samples, these were considered insufficient for performing stability assays.

Based on the formerly reviewed radiolabeling and characterization results, it can be confirmed that grafting of ethanolamine, and therefore, successive linker moieties, does not take place under the synthetic conditions tested. For this reason, the PEG-Ethanolamine functionalization approach was ultimately suspended.

4.3.2.2 Determination of RCP

RCPs of the final [^{68}Ga]Ga-DFO-PEG-Ethanolamine product and precursors after purification are recorded in **Table 21**. Unfortunately, purified versions of the radiolabeled [^{68}Ga]Ga-Unmodified and [^{68}Ga]Ga-HCl cleaned precursors cold not be subjected for evaluation in this case.

Table 21. RCP of ^{68}Ga-labeled products. Results have been classified as for experiments. RCP of [^{68}Ga]Ga-HCl cleaned and [^{68}Ga]Ga-NODAGA-APTES were obtained as a mean based on the measurement of the four radiolabeled replicas. Mean results are also presented with their associated errors (standard deviation).

	2.2-μm borosilicate microparticles		
	[^{68}Ga]Ga-Ethanolamine	[^{68}Ga]Ga-PEG-Ethanolamine	[^{68}Ga]Ga-DFO-PEG-Ethanolamine
RCP (%)	71.9	36.0	48.6

Evidence shows that none of the purified products are able of succesfully retaining [^{68}Ga]Ga^{3+}. In essence, [^{68}Ga]Ga-DFO coordination does not take place succesfully, possibly due to absence of succesfully grafted DFO moieties in the modified borosilicate. This is in concordance with what had been previously reviewed for the characterization of the DFO-PEG-Ethanolamine borosilicate microparticles. For this reason, unbound [^{68}Ga]Ga^{3+} ions are still being lost after every washing step.

In conclusion, PEG-Ethanolamine functionalization of the borosilicate microparticles was not a succesful technique for the design of PET radiotracers.

4.4 ^{18}F-fluorination

As previously described along the aims of this work, a third modification approach using [^{18}F]F$^-$ was pursued. The main goal was to evaluate the potential ability of [^{18}F]F$^-$ of substituting the silanol groups naturally present in the surface of borosilicates. As previously disclaimed along the experimental section, only 2.2-µm borosilicates were subjected to radiolabeling with fluorine-18.

Activity values of both unmodified and HCl cleaned borosilicate particles upon radiofluorination with [^{18}F]F$^-$ can be found along **Table 22**. Recorded values have been decay corrected to SOS. Listed activities are those recorded for SOS and final product after purification.

Table 22. Activity values recorded for unmodified and HCl cleaned borosilicates. Listed activity values have been recorded for SOS and final product after purification. Activity values have been decay corrected for SOS.

	2.2-µm borosilicate microparticles			
	Unmodified			
	Recorded activity (MBq)			
	Set 1	Set 2	Set 3	Set 4
Timepoint	RT, 15 min	RT, 30 min	60 ºC, 15 min	60 ºC, 30 min
SOS	53.9	33.4	33.7	25.7
Final product	2.35	1.04	1.33	1.36

	HCl cleaned			
	Recorded activity (MBq)			
	Set 1	Set 2	Set 3	Set 4
Timepoint	RT, 15 min	RT, 30 min	60 ºC, 15 min	60 ºC, 30 min
SOS	31.8	40.5	28.3	35.0
Final product	2.00	1.35	1.19	1.67

Radioactive parameters of the final purified radiolabeled product based of the data collected from **Table 22** can be found along **Table 23**.

Table 23. Radioactive parameters of the final product. RCY values have been decay corrected for SOS. Exact weight subjected to radiofluorination has also been specified. Radioactivity concentration and As have been obtained with respect to the activity recorded for the final product.

	2.2-µm borosilicate microparticles			
	Unmodified			
Parameter	Set 1 RT, 15 min	Set 2 RT, 30 min	Set 3 60 ºC, 15 min	Set 4 60 ºC, 30 min
Radioactivity concentration (MBq/mL)	3.147	1.382	1.753	1.773
RCY (%)	4	3	4	5
A_S (MBq/mg)	1.888	0.830	1.052	1.064
Radiolabeled product (mg)	0.5	0.5	0.5	0.5

Parameter	HCl cleaned			
	Set 1 RT, 15 min	Set 2 RT, 30 min	Set 3 60 ºC, 15 min	Set 4 60 ºC, 30 min
Radioactivity concentration (MBq/mL)	2.717	1.803	1.573	2.117
RCY (%)	6	3	4	5
A_s (MBq/mg)	1.630	1.082	0.944	1.306
Radiolabeled product (mg)	0.5	0.5	0.5	0.5

Continuation of **Table *23***

Recorded parameters highlight that the radiolabeling of borosilicate particles with $[^{18}F]F^-$ is not a successful approach. RCY values for all of evaluated samples under the different conditions tested are below 10%, showcasing that the majority of injected $[^{18}F]F^-$ was lost during the washing steps required for the purification of the final product. A_s and RC values recorded for the final product are also not ideal considering the amount of radioactivity injected to each sample.

In conclusion, the expected substitution of the silanol groups by $[^{18}F]F^-$ does not take place for either the unmodified or the HCl cleaned borosilicate under any of the studied conditions. There is no evident difference between the recorded RC, RCY or A_s values of unmodified and HCl washed samples for any of the reviewed reaction conditions. This showcases that the activation of superficial silanol groups does not play a significant role in the substitution ability of $[^{18}F]F^-$, again confirming that hydroxyl substitution does not take place under any of the evaluated scenarios.

It is also possible that the substitution of hydroxyl groups is successfully achieved by $[^{18}F]F^-$, but that due to the weak stability of the Si-^{18}F bond in aqueous media, it is all released upon the performed centrifugation steps. This is an extremely undesirable situation when designing radiotracers, as these need to be stable in blood.

RCP of the final radiolabeled products was also evaluated. RCP values are recorded in **Table 24**.

Purified products subjected to radiofluorination still present a high amount of free $[^{18}F]F^-$. All of evaluated products seem to be less than 70%, confirming that $[^{18}F]F^-$ is continuously being lost even after three centrifuge cycles.

This meets with previously discussed radiolabeling results and concludes that radiolabeling with $[^{18}F]F^-$ does not take place under the evaluated reaction conditions, and that obtained products are not successfully purified either.

Table 24. RCP of fluorine-18 labeled products. [^{18}F]F-Unmodified and [^{18}F]F-HCl cleaned products.

	2.2-µm borosilicate microparticles			
	[^{18}F]F-Unmodified			
	Set 1 RT, 15 min	Set 2 RT, 30 min	Set 3 60 ºC, 15 min	Set 4 60 ºC, 30 min
RCP (%)	43.7	53.1	67.4	5.8

	2.2-µm borosilicate microparticles			
	[^{18}F]F-HCl cleaned			
	Set 1 RT, 15 min	Set 2 RT, 30 min	Set 3 60 ºC, 15 min	Set 4 60 ºC, 30 min
RCP (%)	25.9	49.8	39.5	4.5

Although the radiofluorination of the non-functionalized borosilicates represents an ideal radiolabeling approach, as it involves minimal alteration of the original microparticles, it had to be discontinued based on the previously discussed results. In conclusion, ^{18}F-fluorination of borosilicates is not a suitable approach for the development of PET radiotracers for biodistribution studies.

5 Conclusions

Radiolabeling of synthetic borosilicate microparticles with radionuclides used for PET imaging has demonstrated to be a promising approach for the development of tracers resembling CsMPs released on the FDNPP accident.

The main idea of this project was to modify the surface of synthetic borosilicate microparticles with APTES in order to graft a suitable chelator for the coordination of positron emitting radiometals like gallium-68 or zirconium-89. However, throughout the duration of this work, limitations associated with sample characterization or accessibility to specific techniques called for the design of alternative approaches. Innovative alternatives, born upon extensive literature research, were based on the use of alternative surface functionalization units, like PEG-Ethanolamine, or PET radionuclides, like fluorine-18, giving place to the three radiolabeling approaches discussed in this thesis.

The major limitation of this study is that radiolabeling real CsMPs for tracking under PET is not possible, as these particles are too difficult to obtain. Throughout this work, two different types of spherical borosilicate microparticles resembling the composition and morphology of CsMPs were used as surrogates, with diameters of 44-μm and 2.2-μm. The 2.2-μm synthetic microparticles were of special interest due to their size and morphological similarity to type A CsMPs (0.1–10 μm), which are the most common type of radioactive particles observed after the FDNPP accident. Their smaller size is a topic of concern regarding inhalation studies, as that they can penetrate deeper into the body. For this reason, experiments with larger 44-μm microparticles were discontinued early on.

Surface modification of the 2.2-μm and 44 μm synthetic borosilicate microparticles with APTES and PEG-Ethanolamine functionalizing agents was studied under FTIR, Zeta-potential, TGA, SEM, EDS, Elemental Analysis, XPS and ERDA. Although APTES functionalization of the 2.2-μm microparticles was successfully confirmed under XPS and supported by elemental analysis and zeta-potential measurements, functionalization with PEG-Ethanolamine could not be confirmed by any of the used techniques. APTES functionalization was also confirmed for the 44-μm borosilicates via XPS analysis. SEM images showed no morphological alterations for any of the functionalized samples.

The wide variety of characterization techniques needed along this project required intensive study and understanding of their operation principles. Knowledge about the functionalized microparticles was increased during the interpretation of results, as deep literature research was needed to understand the proper way to present and analyze obtained data. This is the first detailed study to demonstrate the successful functionalization of 2.2-µm and 44-µm spherical borosilicate microparticles with APTES.

Radiolabeling of the 2.2-µm borosilicate microparticles with gallium-68 was performed on NODAGA-APTES, DFO-APTES, DFO-PEG-Ethanolamine, HCl cleaned and unmodified samples. ^{18}F-fluorination was performed on the HCl cleaned and unmodified particles. NODAGA-APTES functionalized 44-µm borosilicates were also ^{68}Ga-labeled.

^{68}Ga-labeling of NODAGA-APTES functionalized 2.2-µm borosilicates was proved successful, with a mean RCY of 65 ± 5%. RCP of the final [^{68}Ga]Ga-NODAGA-APTES product. RCP was of 94 ± 2% after centrifugation with an EDTA complexing solution, which ensured almost total elimination of loosely bound [^{68}Ga]Ga^{3+}. On the other hand, ^{68}Ga-labeling of DFO-APTES and DFO-PEG-Ethanolamine 2.2-µm microparticles was not successful, with RCYs below 15% and RCPs of the final radiolabeled product of about 50%. ^{68}Ga-labeling of the HCl cleaned precursor suggests that the high non-specific coordination of [^{68}Ga]Ga^{3+} ions with silanol groups present on the surface of the microparticles possibly holds a supporting effect in the ^{68}Ga-labeling of NODAGA-APTES modified microparticles. ^{68}Ga-labeling of the 44-µm NODAGA-APTES functionalized particles was also unsuccessful, with an RCY below 10%, and RCP of the final product over 90%.

^{18}F-fluorination of unmodified and HCl cleaned 2.2-µm microparticles was proven unsuccessful at four different reaction conditions (15 min, room temperature; 30 min, room temperature; 15 min, 60 ºC; and 30 min, 60 ºC). This was associated to the tendency of the [^{18}F]F-Si bond to undergo hydrolysis aqueous media, .

Radiolabeling results were essential for the discontinuation of the radiofluorination approach, as well as of ^{68}Ga-labeling experiments on the 44-µm microparticles and PEG-ethanolamine functionalized 2.2-µm borosilicates. Although radiolabeling with PET radionuclides did not yield positive results for all of the

approaches, it was the most determinant step in the confirmation of a reliable synthetic radiotracer. Effective labeling of the NODAGA-APTES borosilicate microparticles with gallium-68 aligned with the initial the aims of the project. This is the first reported evidence for the radiolabeling of synthetic borosilicates with a positron emitting radionuclide.

NODAGA proved to be the most efficient chelator for the coordination of gallium-68, thanks to the marching size of the chelator cavity with the ionic radius of the $[^{68}Ga]Ga^{3+}$ ions. Coordination of $[^{68}Ga]Ga^{3+}$ ions with the DFO chelator was not experimentally observed, possibly due to the low temperature conditions used during the radiolabeling reaction. Although radiolabeling with zirconium-89 upon coordination with DFO chelator was initially considered in the extent of this project, it could not be performed due to time constraints. This unfortunately prevented the *in vivo* administration of the designed radiotracers into mice or rats, and therefore, their observation under PET for realistic biodistribution studies.

Stability assays were performed over a 0-3 hour timeframe in 1 × PBS, 50% plasma, 0.2 mM $FeCl_3$, 2 mM EDTA and SLF media resembling physiological conditions. These showed that the stability of the final product remained above 90% for all of evaluated media, suggesting that the designed $[^{68}Ga]$Ga-NODAGA-APTES tracer was stable under physiological conditions.

The overtime stability of the $[^{68}Ga]$Ga-NODAGA-APTES tracer shows a promising advance in the design of tracers resembling CsMPs. Since the use of synthetic borosilicate particles radiolabeled with PET radionuclides has not been previously reported, the results obtained along this thesis are very promising for the assessment of CsMPs behaviour in biological systems. The continuation of this study should be directed to the use of longer-lived radionuclides such as zirconium-89, which would allow for the *in vivo* administration and PET tracking of synthetic radiotracers.

If the biodistribution and pharmacokinetics of synthetic borosilicate microparticles could be fully addressed using imaging techniques, it would be possible to estimate the received dose and subsequent radiobiological health effects associated with the inhalation of CsMPs. Designing a stable radiotracer that represents the behaviour of inhaled CsMPs would therefore have an incredible impact on the lives of

those affected by the FDNPP accident. The results collected along this thesis prove that science is one step closer to the completion of this goal.

References

1. Furuki, G., Imoto, J., Ochiai, A., Yamasaki, S., Nanba, K., Ohnuki, T., Grambow, B., Ewing, R. C., & Utsunomiya, S. (2017). Caesium-rich micro-particles: A window into the meltdown events at the Fukushima Daiichi Nuclear Power Plant. Scientific Reports, 7(1). https://doi.org/10.1038/srep42731. Caesium-rich micro-particles A Wind. into meltdown events Fukushima Daiichi Nucl. Power Plant. Sci. Reports, 7(1). https//doi.org/10.1038/srep42731.
2. Suetake, M., Nakano, Y., Furuki, G., Ikehara, R., Komiya, T., Kurihara, E., Morooka, K., Yamasaki, S., Ohnuki, T., Horie, K., Takehara, M., Law, G. T. W., Bower, W. R., Grambow, B., Ewing, R. C., & Utsunomiya, S. (2019). Dissolution Radioact. cesium-rich microparticles released from Fukushima Daiichi Nucl. Power Plant simulated lung fluid, pure-water, seawater. Chemosphere, 233, 633–644. https//doi.org/10.1016/j.chemosphere.2019.05.248.
3. Miura, H., Kurihara, Y., Yamamoto, M., Sakaguchi, A., Yamaguchi, N., Sekizawa, O., Nitta, K., Higaki, S., Tsumune, D., Itai, T., & Takahashi, Y. (2020). Miura, H., Kurihara, Y., Yamamoto, M., Sakaguchi, A., Yamaguchi, N., Sekizawa, O., Nitta, K., Higaki, S., Tsumune, D., Itai, T., & Takahashi, Y. (2020). Characterization of two types of cesium-bearing microparticles emitted from the Fukushima accident via. Charact. two types cesium-bearing microparticles Emit. from Fukushima Accid. via Mult. synchrotron Radiat. Anal. Sci. Reports, 10(1). https//doi.org/10.1038/s41598-020-68318-2.
4. Ikehara, R., Morooka, K., Suetake, M., Komiya, T., Kurihara, E., Takehara, M., Takami, R., Kino, C., Horie, K., Takehara, M., Yamasaki, S., Ohnuki, T., Law, G. T. W., Bower, W. R., Grambow, B., Ewing, R. C., & Utsunomiya, S. (2020b). Abundance Distrib. Radioact. cesium-rich microparticles released from Fukushima Daiichi Nucl. Power Plant into Environ. Chemosphere, 241, 125019. https//doi.org/10.1016/j.chemosphere.2019.125019.
5. European Union, DG Health and Consumer Protection, Public Health. What are potential harmful effects of nanoparticles? (n.d.). https://ec.europa.eu/health/scientific_committees/opinions_layman/en/nanotechnologies/l-3/6-health-effects-nanoparticles.htm#3p0.
6. Mobley, C., & Hochhaus, G. (2001). Methods used to assess pulmonary deposition and absorption of drugs. Drug Discovery Today, 6(7), 367–375. https://doi.org/10.1016/s1359-6446(01)01691-9.
7. Fröhlich, E., & Salar-Behzadi, S. (2014). Toxicological Assessment of Inhaled Nanoparticles: Role of in Vivo, ex Vivo, in Vitro, and in Silico Studies. International Journal of Molecular Sciences, 15(3), 4795–4822. https://doi.org/10.3390/ijms15034795.
8. Suzui, N., Shibata, T., Yin, Y., Funaki, Y., Kurita, K., Hoshina, H., Yamaguchi, M., Fujimaki, S., Seko, N., Watabe, H., & Kawachi, N. (2020). Non-invasive imaging radiocesium Dyn. a living Anim. using a positron-emitting 127Cs tracer. Sci. Reports, 10(1). https//doi.org/10.1038/s41598-020-73351-2.
9. McInnes, L. E., Rudd, S. E., & Donnelly, P. S. (2017). Copper, gallium and zirconium positron emission tomography imaging agents: The importance of metal ion speciation. Coordination

Chemistry Reviews, 352, 499–516. https://doi.org/10.1016/j.ccr.2017.05.0.

10. Tsionou, M. I., Knapp, C. E., Foley, C. A., Munteanu, C. R., Cakebread, A., Imberti, C., Eykyn, T. R., Young, J. P., Paterson, B. M., Blower, P. J., & Michelle, T. (2017a). Comp. Macrocycl. acyclic chelators Gall. radiolabelling. RSC Adv. 7(78), 49586–49599. https//doi.org/10.1039/c7ra09076e.
11. Yoon, J., Park, B., Ryu, E., An, Y., & Lee, S. J. (2020). Current Perspectives on 89ZR-PET Imaging. International Journal of Molecular Sciences, 21(12), 4309. https://doi.org/10.3390/ijms21124309.
12. Massera, J., Mishra, A., Guastella, S., Ferraris, S., & Verné, E. (2016b). Surface functionalization of phosphate-based bioactive glasses with 3-aminopropyltriethoxysilane (APTS). Biomedical Glasses, 2(1). https://doi.org/10.1515/bglass-2016-0007.
13. Gobbo, V. A., Parihar, V., Prato, M., Kellomäki, M., Verné, E., Spriano, S. M., & Massera, J. (2023a). Surf. Modif. Silic. borosilicate phosphate Bioact. Glas. to Improv. protein Adsorpt. PART I. Ceram. Int. 49(1), 1261–1275. https//doi.org/10.1016/j.ceramint.2022.09.105.
14. Janissen, R., Oberbarnscheidt, L., & Oesterhelt, F. (2009). Optimized straight forward procedure for covalent surface immobilization of different biomolecules for single molecule applications. Colloids Surfaces B Biointerfaces, 71(2), 200–207. https//doi.org/10.1016/j.colsurfb.2009.02.011.
15. Halder, R., & Ritter, T. (2021). 18F-Fluorination: Challenge and Opportunity for Organic Chemists. The Journal of Organic Chemistry, 86(20), 13873–13884. https://doi.org/10.1021/acs.joc.1c01474.
16. Cole, E. L., Stewart, M. N., Littich, R., Hoareau, R., & Scott, P. J. H. (2014). Radiosyntheses using Fluorine-18: The Art and Science of Late Stage Fluorination. Current Topics in Medicinal Chemistry, 14(7), 875–900. https://doi.org/10.2174/1568026614666.
17. Wängler, C., Kostikov, A., Zhu, J., Chin, J., Wängler, B., & Schirrmacher, R. (2012). Silicon-[18F]Fluorine Radiochemistry: Basics, applications and challenges. Applied Sciences, 2(2), 277–302. https://doi.org/10.3390/app2020277.
18. Fukushima Daiichi Accident - World Nuclear Association. (n.d.). August 2023. https://world-nuclear.org/information-library/safety-and-security/safety-of-plants/fukushima-daiichi-accident.aspx. Accessed on 08/01/2023.
19. Nuclide Search. (n.d.). https://nucleardata.nuclear.lu.se/toi/nucSearch.asp; Accessed on 09/01/2024.
20. Ono, T., Iizawa, Y., Abe, Y., Nakai, I., Terada, Y., Satou, Y., Sueki, K., Adachi, K., & Igarashi, Y. (2017). Investigation of the Chemical Characteristics of Individual Radioactive Microparticles Emitted from Reactor 1 by the Fukushima Daiichi. Nucl. Power Plant Accid. by Using Mult. Synchrotron Radiat. X-ray Anal. Bunseki Kagaku, 66(4), 251–261. https//doi.org/10.2116/bunsekikagaku.66.251.
21. Kurihara, Y., Takahata, N., Yokoyama, T., Miura, H., Kon, Y., Takagi, T., Higaki, S., Yamaguchi, N., Sano, Y., & Takahashi, Y. (2020). Isotopic ratios of uranium and. caesium spherical Radioact. caesium-bearing microparticles Deriv. from Fukushima Dai-ichi Nucl. Power Plant. Sci. Reports,

10(1). https//doi.org/10.1038/s41598-020-59933-0.

22. Aliyu, A. S., Evangeliou, N., Mousseau, T. A., Wu, J. W., & Ramli, A. T. (2015). An overview of current knowledge concerning the health and environmental. consequences Fukushima Daiichi Nucl. Power Plant Accid. Environ. Int. 85, 213–228. https//doi.org/10.1016/j.envint.2015.09.020.
23. Oberdörster, G., & Kuhlbusch, T. a. J. (2018). In vivo effects: Methodologies and biokinetics of inhaled nanomaterials. NanoImpact, 10, 38–60. https://doi.org/10.1016/j.impact.2017.10.007.
24. Eedara, B. B., Bastola, R., & Das, S. C. (2022b). Dissolution and absorption of inhaled drug particles in the lungs. Pharmaceutics, 14(12), 2667. https://doi.org/10.3390/pharmaceutics14122667.
25. Fröhlich, E. (2018). Comparison of conventional and advanced in vitro models in the toxicity testing of nanoparticles. Artificial Cells Nanomedicine and Biotechnology, 46(sup2), 1091–1107. https://doi.org/10.1080/21691401.2018.1479709.
26. Alfaro-Moreno, E., Nawrot, T. S., Vanaudenaerde, B. M., Hoylaerts, M., Vanoirbeek, J., Nemery, B., & Hoet, P. (2008). Co-cultures Mult. cell types mimic Pulm. cell Commun. response to urban PM10. Eur. Respir. Journal, 32(5), 1184–1194. https//doi.org/10.1183/09031936.00044008.
27. Grimaud, J., & Murthy, V. N. (2018). How to monitor breathing in laboratory rodents: a review of the current methods. Journal of Neurophysiology, 120(2), 624–632. https://doi.org/10.1152/jn.00708.2017.
28. Sakagami, M. (2020). In vitro, ex vivo and in vivo methods of lung absorption for inhaled drugs. Advanced Drug Delivery Reviews, 161–162, 63–74. https://doi.org/10.1016/j.addr.2020.07.025.
29. Longest, P. W., & Holbrook, L. T. (2012). In silico models of aerosol delivery to the respiratory tract — Development and applications. Advanced Drug Delivery Reviews, 64(4), 296–311. https://doi.org/10.1016/j.addr.2011.05.009.
30. Bergström, M., Grahnén, A., & Långström, B. (2003). Positron emission tomography microdosing: a new concept with application in tracer and early clinical drug development. European Journal of Clinical Pharmacology, 59(5–6), 357–366. https://doi.org/10.100.
31. Fahey, F. H. (2002, June 1). Data acquisition in PET imaging. Journal of Nuclear Medicine Technology. https://tech.snmjournals.org/content/30/2/39.full.
32. Bar-Shalom, R., Valdivia, A. Y., & Blaufox, M. D. (2000). PET imaging in oncology. Seminars in Nuclear Medicine, 30(3), 150–185. https://doi.org/10.1053/snuc.2000.7439.
33. Jiang, W., Chalich, Y., & Deen, M. J. (2019). Sensors for positron emission tomography applications. Sensors, 19(22), 5019. https://doi.org/10.3390/s19225019.
34. Murshed, H. (2019). Fundamentals of Radiation Oncology: Physical, Biological, and Clinical Aspects (3rd edition., pp. 675-689). Academic Press.
35. Price, E. W., & Orvig, C. (2014). Matching chelators to radiometals for radiopharmaceuticals. Chemical Society Reviews, 43(1), 260–290. https://doi.org/10.1039/c3cs60304k.
36. Rong, J., Haider, A., Jeppesen, T. E., Josephson, L., & Liang, S. H. (2023). Radiochemistry for positron emission tomography. Nature Communications, 14(1). https://doi.org/10.1038/s41467-023-36377-4.
37. Singh, A. N., Liu, W., Hao, G., Kumar, A., Gupta, A., Öz, O., Hsieh, J. T., & Sun, X. (2011).

Multivalent bifunctional chelator scaffolds for gallium-68 based positron emission Tomography Imaging probe design: Signal Amplif. via multivalency. Bioconjugate Chem. 22(8), 1650–1662. https//doi.org/10.1021/bc200227d.

38. Nuclear data – Laboratoire National Henri Becquerel. (n.d.). http://www.lnhb.fr/home/nuclear-data/; Accessed on 03/02/2023.
39. Nelson, B. J. B., Andersson, J., Wuest, F., & Spreckelmeyer, S. (2022). Good practices for 68Ga radiopharmaceutical production. EJNMMI Radiopharmacy and Chemistry, 7(1). https://doi.org/10.1186/s41181-022-00180-1.
40. Rösch, F. (2012). 68GE/68GA Generators: Past, Present, and future. In Recent results in cancer research (pp. 3–16). https://doi.org/10.1007/978-3-642-27994-2_1.
41. Gaja, V., Cawthray, J. F., Geyer, C. R., & Fonge, H. (2020). Production and Semi-Automated processing of 89ZR using a commercially available TRASIS MiniAIO module. Molecules, 25(11), 2626. https://doi.org/10.3390/molecules25112626.
42. Neumaier, B. (2014). 18F-Labelled Intermediates for Radiosynthesis by Modular Build-Up Reactions: Newer Developments. BioMed Research International, 2014, 1–15. https://doi.org/10.1155/2014/812973.
43. Kirjavainen, A. (2014). Radiosynthesis and use of [18F]F2 derivatives [18F]selectfluor Bis(triflate) and [18F]CIF [PhD dissertation,. Univ. Turku]. https//www.utupub.fi/bitstream/handle/10024/102062/AnnalesD1149Kirjavainen.pdf?sequence=2&isAllowed=y.
44. Ferraris, S., Nommeots-Nomm, A., Spriano, S. M., Verné, E., & Massera, J. (2019c). Surface reactivity and silanization ability of borosilicate and Mg-Sr-based bioactive glasses. Applied Surface Science, 475, 43–55. https://doi.org/10.1016/j.apsusc.2018.12.
45. Grandi, S., Spinella, A., Tomasi, C., Bruni, G., Fagnoni, M., Merli, D., Mustarelli, P., Guidetti, G. F., Achilli, C., & Balduini, C. (2012). Synthesis and characterisation. Funct. borosilicate nanoparticles boron neutron capture Ther. Appl. J. Sol-Gel Sci. Technol. 64(2), 358–366. https//doi.org/10.1007/s10971-012-2865-9.
46. Flink, S., Van Veggel, F. C. J. M., & Reinhoudt, D. N. (2001b). Functionalization of self-assembled monolayers on glass and oxidized silicon wafers by surface reactions. Journal of Physical Organic Chemistry, 14(7), 407–415. https://doi.org/10.1002/poc.37.
47. Howarter, J. A., & Youngblood, J. P. (2006). Optimization of silica silanization by 3-Aminopropyltriethoxysilane. Langmuir, 22(26), 11142–11147. https://doi.org/10.1021/la061240g.
48. Mutua, F. N., Lin, P., Koech, J. K., & Wang, Y. (2012b). Surface modification of hollow glass microspheres. Materials Sciences and Applications, 03(12), 856–860. https://doi.org/10.4236/msa.2012.312125.
49. Nor, S. S. M., Patah, M. F. A., & Salleh, M. M. (2022). Surface modification of bio-based composites via silane treatment: a short review. Journal of Adhesion Science and Technology, 37(5), 801–816. https://doi.org/10.1080/01694243.2022.2049087.
50. Ebner, A., Hinterdorfer, P., & Gruber, H. J. (2007). Comparison of different

aminofunctionalization strategies for attachment of single antibodies to AFM cantilevers. Ultramicroscopy, 107(10–11), 922–927. https://doi.org/10.1016/j.ultramic.2007.02.035.

51. Lu, L., Duong, V. T., Shalash, A. O., Skwarczynski, M., & Tóth, I. (2021c). Chemical Conjugation Strategies for the development of Protein-Based Subunit Nanovaccines. Vaccines, 9(6), 563. https://doi.org/10.3390/vaccines9060563.
52. FTIR | FTIR Microscopes | FTIR Spectrometers | Thermo Fisher Scientific - IE. (n.d.). https://www.thermofisher.com/es/es/home/industrial/spectroscopy-elemental-isotope-analysis/molecular-spectroscopy/fourier-transform-infrared-ftir-spectroscopy.html.
53. U. Hassan, M. S. Anwar, H. Laser, and T. Labs, “Michelson Interferometry,” pp. 2–6, 2010.
54. P. Hinton-Sheley, “ATR-FTIR: An Overview.” https://www.azolifesciences.com/article/What-is-ATR-FTIR.aspx (accessed May 07, 2022).
55. Malvern Instruments Worldwide. Zeta potential - An introduction in 30 minutes. https://www.research.colostate.edu/wp-content/uploads/2018/11/ZetaPotential-Introduction-in-30min-Malvern.pdf. Accessed on 08/05/2024.
56. Ferraris, S., Cazzola, M., Peretti, V., Stella, B., & Spriano, S. M. (2018). ZETA Potential measurements on solid surfaces for in vitro biomaterials testing: Surf. Charg. React. upon contact with fluids protein absorption. Front. Bioeng. Biotechnol. 6. https//doi.org/10.3389/fbioe.2018.00060.
57. Hunter, R. J. (1981). Zeta potential in colloid science : principles and applications. http://ci.nii.ac.jp/ncid/BA07258103.
58. PerkinElmer. FAQ. Thermogravimetric Analysis (TGA). https://resources.perkinelmer.com/lab-solutions/resources/docs/faq_beginners-guide-to-thermogravimetric-analysis_009380c_01.pdf. Accessed on 08/05/2024.
59. Ebnesajjad, S. (2006). Surface and material characterization techniques. In Elsevier eBooks (pp. 43–75). https://doi.org/10.1016/b978-081551523-4.50006-7.
60. STA 449 F3 Jupiter. (n.d.). NETZSCH - Analyzing and Testing. Leading in Thermal Analysis, Rheology and Fire Testing. https://analyzing-testing.netzsch.com/es/productos/termogravimetria-simultanea-calorimetria-de-barrido-diferencial/sta-449-f3-jupiter.
61. University Complutense of Madrid. Technique Scanning Electron microscopy (SEM). (n.d.). https://cai.ucm.es/en/earth-sciences-archeometry/geological-techniques/techniques/scanning-electron-microscopy-sem/24. Accessed on 08/05/2024.
62. SERC. Scanning Electron Microscopy (SEM). (n.d.-b). Techniques. https://serc.carleton.edu/research_education/geochemsheets/techniques/SEM.html. Accessed on 08/05/2024.
63. Nanoscience Instruments. Scanning Electron Microscopy | Nanoscience Instruments. (n.d.). https://www.nanoscience.com/techniques/scanning-electron-microscopy. Accessed on 08/05/2024.
64. Bruker. What is EDS? | Energy Dispersive X-Ray Spectroscopy. (n.d.). https://www.bruker.com/es/landingpages/bna/technology/what-is-eds.html. Accessed on

07/05/2024.

65. Celignis Analytical. Equipment used in Celignis - Elemental Analyser. (n.d.). https://www.celignis.com/equip.php?value=4. Accessed on 09/05/2024.
66. Physical Electronics. X-Ray Photoelectron Spectroscopy (XPS) surface analysis technique. (n.d.). https://www.phi.com/surface-analysis-techniques/xps-esca.html. Accessed on 07/05/2024.
67. Montana State University. X-ray photoelectron spectroscopy. (n.d.). Methods. https://serc.carleton.edu/msu_nanotech/methods/xps.html. Accessed on 08/05/2024.
68. Jokinen, J., Keinonen, J., Tikkanen, P., Kuronen, A., Ahlgren, T., & Nordlund, K. (1996). Comparison of TOF-ERDA and nuclear resonance reaction techniques for range profile measurements of keV energy implants. Nuclear Instruments and Methods in Physics. Res. Sect. B, Beam Interact. With Mater. Atoms/Nuclear Instruments Methods Phys. Res. Sect. B, Beam Interact. With Mater. Atoms, 119(4), 533–542. https//doi.org/10.1016/s0168-583x(96)00469-7.
69. D. Guillaume, P. Anne-Sophie, B. Thomas; Chemical element imaging for speleothem geochemistry: Application to a uranium-bearing corallite with aragonite diagenesis to opal (Eastern Siberia, Russia); February 2012; DOI:10.1016/j.chemgeo.2011.12.003.
70. Imlimthan, S., Khng, Y. C., Keinänen, O., Zhang, W., Airaksinen, A. J., Kostiainen, M. A., Zeglis, B. M., Santos, H. A., & Sarparanta, M. (2021). A Theranostic Cellul. Nanocrystal-Based Drug Deliv. Syst. with Enhanc. Retent. Pulm. Metastasis Melanoma. Small, 17(18). https//doi.org/10.1002/smll.202007705.
71. Zhang, X., Zhang, M., & Lin, J. (2022c). Effect of PH on the in vitro degradation of borosilicate bioactive glass and its modulation by direct current electric field. Materials, 15(19), 7015. https://doi.org/10.3390/ma15197015.
72. Pretsch, E., Bühlmann, P., Badertscher, M. Structure determination of organic compounds. (2009). https://doi.org/10.1007/978-3-540-93810-1.
73. Hamidon, T. S., Ishak, N. ‘., & Hussin, M. H. (2021). Enhanced corrosion inhibition of low carbon steel in aqueous sodium chloride employing sol–gel-based hybrid silanol coatings. J. Sol-gel Sci. Technol. 97(3), 556–571. https//doi.org/10.1007/s10971-021-05474-5.
74. Li, X., Feng, J., Jiang, Y., & Lin, H. (2018). Preparation and anti-oxidation performance of Al2O3-containing TaSi2–MoSi2–borosilicate glass coating on porous SiCO ceramic composites for thermal protection. RSC Adv. 8(24), 13178–13185. https//doi.org/10.1039/c8ra00703a.
75. Wan, J., Cheng, J., & Ping, L. (2008). The coordination state of B and Al of borosilicate glass by IR spectra. Journal of Wuhan University of Technology, 23(3), 419–421. https://doi.org/10.1007/s11595-007-3419-9.
76. Santha, N., Nideep, T. K., & Rejisha, S. R. (2011). Synthesis and characterization of barium borosilicate glass–Al2O3 composites. Journal of Materials Science. Materials in Electronics, 23(7), 1435–1441. https://doi.org/10.1007/s10854-011-0609-1.
77. Wang, W., Cai, D., & Zhang, L. (2018). A review of fluorine-free mold flux development. ISIJ International, 58(11), 1957–1964. https://doi.org/10.2355/isijinternational.isijint-2018-232.
78. Li, J., Sun, Y., Li, Z., & Zhang, Z. (2016). Short-range and Medium-range Structural Order in

CaO–SiO2–TiO2–BO3 Glasses. ISIJ International, 56(5), 752–758. https://doi.org/10.2355/isijinternational.isijint-2015-586.

79. Majoul, N., Aouida, S., & BessaïS, B. (2015). Progress of porous silicon APTES-functionalization by FTIR investigations. Applied Surface Science, 331, 388–391. https://doi.org/10.1016/j.apsusc.2015.01.107.
80. Precision Micro Optics. Corning Pyrex borosilicate glass. (n.d.). https://www.pmoptics.com/corning_pyrex.html.
81. Peeraphatdit, C. (2022, December 9). What is the Difference Between Thermogravimetric Analysis (TGA) and Differential Scanning Calorimetry (DSC) - Particle Technology Labs. Part. Technol. Labs. https//particletechlabs.com/ptl-press/what-is-the-difference-between-thermogravimetric-analysis-tga-and-differential-scanning-calorimetry-dsc/.
82. Rafferty, A. (2003). An investigation into the amorphous phase separation characteristics of an ionomer glass series and a Sodium-Boro-Silicate glass system. Journal of Materials Science, 38(11), 2311–2319. https://doi.org/10.1023/a:1023972127593.
83. Maurya, P., GS, V., & Kamath, R. C. (2023). Evaluation of glass-transition temperature and influence of low-temperature condition on the moduli of acrylonitrile-butadiene rubber. Materials Today: Proceedings. https://doi.org/10.1016/j.matpr.2023.03.451.
84. Zapf-Gottwick, R., Seren, S., Fernandez-Robledo, S., Wete, E., Schiliró, M., Hassan, M., Mihailetchi, V. D., Bück, T., Kopecek, R., Köhler, J., & Werner, J. (2022). Solar Cells with Laser Doped Boron Layers from Atmospheric Pressure Chemical Vapor. Depos. Solar, 2(2), 274–292. https//doi.org/10.3390/solar2020015.
85. D. B. Thombre and Megha D. Thombre (2014). Study of Physical Properties of Lithium-borosilicate glasses. https://api.semanticscholar.org/CorpusID:55966746.
86. Barret. (2023, September 11). How to estimate glass transition temperature of PLGA? My WordPress. https://polylactide.com/estimate-glass-transition-temperature-of-plga/.
87. Buchwalter, S. L. (2001). Semiconductor chip underfill materials. (pp. 8332–8335). https://doi.org/10.1016/b0-08-043152-6/01492-3.
88. Phadatare, M., Patil, R., Blomquist, N., Forsberg, S., Örtegren, J., Hummelgård, M., Meshram, J., Hernández, G., Brandell, D., Leifer, K., Sathyanath, S. K. M., & Olin, H. (2019). Silicon-Nanographite Aerogel-Based anodes high Perform. lithium ion Batter. Sci. Reports, 9(1). https//doi.org/10.1038/s41598-019-51087-y.
89. 1801 - Kapton® Polyimide Silicone Adhesive tape. (n.d.). https://www.scapaindustrial.com/products/product-details/details/1801.
90. Ektessabi, A. M., & Hakamata, S. (2000). XPS study of ion beam modified polyimide films. Thin Solid Films, 377–378, 621–625. https://doi.org/10.1016/s0040-6090(00)01444-9.
91. Dolgov, A. A., Lopaev, D., Lee, C., Zoethout, E., Медведев, В. В., Yakushev, O. F., & Bijkerk, F. (2015a). Charact. carbon Contam. under ion hot atom Bombard. a tin-plasma Extrem. Ultrav. Light source. Appl. Surf. Sci. 353, 708–713. https//doi.org/10.1016/j.apsusc.2015.06.079.
92. Blanco, M., Mosconi, D., Otyepka, M., Medveď, M., Bakandritsos, A., Agnoli, S., & Granozzi, G. (2019). Combined high degree of carboxylation and electronic conduction in graphene acid sets

new limits for metal free catalysis in alcohol oxidation. Chem. Sci. 10(41), 9438–9445. https//doi.org/10.1039/c9sc02954k.

93. Hatada, R., Flege, S., Ensinger, W., Hesse, S., Tanabe, S., Nishimura, Y., & Baba, K. (2020). Preparation of Aniline-Based Nitrogen-Containing Diamond-Like Carbon Films with Low Electrical Resistivity. Coatings, 10(1), 54. https://doi.org/10.3390/coatings.
94. Zhang, Y., Zhu, L., Chen, L., Liu, L., & Ye, G. (2019). Influence of magnesia on demoulding strength of colloidal Silica-Bonded castables. Reviews on Advanced Materials Science, 58(1), 32–37. https://doi.org/10.1515/rams-2019-0008.
95. W, J., Lee, W. J., Bae, J. M., Jeong, K. S., Oh, S. H., Kim, J. H., Kim, S., Seo, J., Ahn, J. P., Kim, H., & Cho, M. (2015). Carr. Mobil. Enhanc. tensile strained SI SIGE nanowires via Surf. defect Eng. Nano Lett. 15(11), 7204–7210. https//doi.org/10.1021/acs.nanolett.5b01634.
96. Xu, M., Jin, F., Peng, A., Jiang, X., Guo, X., & Wu, G. (2024). Influence of different Ga species in MWW zeolite bifunctional catalysts on the ethane dehydrogenation and dehydroaromatization in the absence and presence of CO2. Fuel, 363, 130968. https://doi.org/10.1016/j.fuel.2024.130968.
97. Phadke, N. M., Van Der Mynsbrugge, J., Mansoor, E., Getsoian, A. “., Head-Gordon, M., & Bell, A. T. (2018). Characterization of Isolated Ga3+ Cations in Ga/H-MFI Prepared by Vapor-Phase Exchange of H-MFI Zeolite with GaCl3. ACS Catalysis, 8(7), 6106–6126. https://doi.org/10.1021/acscatal.8b01254.
98. Rabanel, J., Hildgen, P., & Banquy, X. (2014). Assessment of PEG on polymeric particles surface, a key step in drug carrier translation. Journal of Controlled Release, 185, 71–87. https://doi.org/10.1016/j.jconrel.2014.04.017.
99. Zhang, Z., Hu, M., Lv, B., Kang, J., Tang, J., Fei, Z., Chen, X., Liu, Q., Cui, M., & Qiao, X. (2018). Solvent-Assisted Stepwise Redox Approach To Generate Zeolite NaA-Supported K2O as Strong Base Catalyst for Michael. Addit. Ethyl Acrylate with Ethanol. ACS Omega, 3(8), 10188–10197. https//doi.org/10.1021/acsomega.8b00704.

Appendix 1 – iTLCs for determination of RCP

Examples of iTLCs evaluated under autoradiography will be shown very briefly throughout this appendix. This is only contemplated as supporting information for interest of the reader. Not all of evaluated iTLCs will be registered.

- APTES functionalization: ^{68}Ga-labeling Experiment 1

In this case, free [^{68}Ga]$GaCl_3$ was also spotted only for visual comparison with the radiolabeled product.

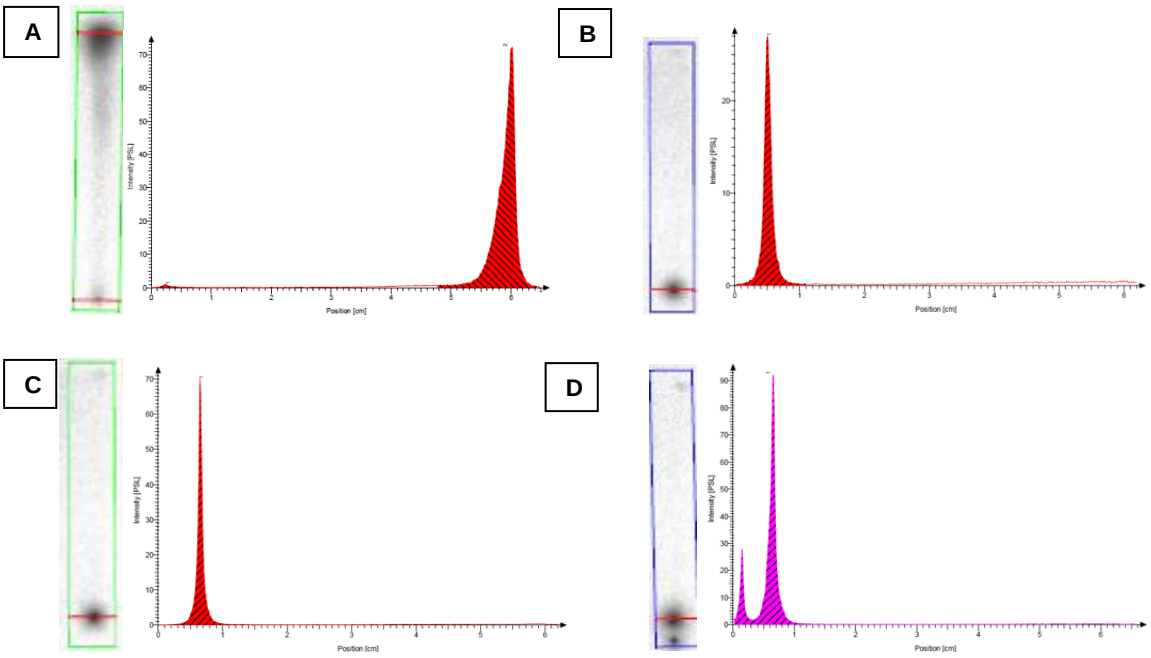

Figure 36. iTLC plates evaluated under autoradiography. Exposed plate is on the left, radiation intensity in PSL versus position in cm on the right. **(A)** Free [^{68}Ga]$GaCl_3$ and **(B)** [^{68}Ga]Ga-Unmodified, **(C)** [^{68}Ga]Ga-APTES and **(D)** [^{68}Ga]Ga-NODAGA-APTES purified radiolabeled borosilicates. 44-µm microparticles.

- PEG-Ethanolamine functionalization: ^{68}Ga-labeling

Free [^{68}Ga]$GaCl_3$ was also spotted for visual comparison. Unfortunately, purified versions of the radiolabeled [^{68}Ga]Ga-Unmodified and [^{68}Ga]Ga-HCl cleaned precursors cold not be subjected for evaluation in this case.

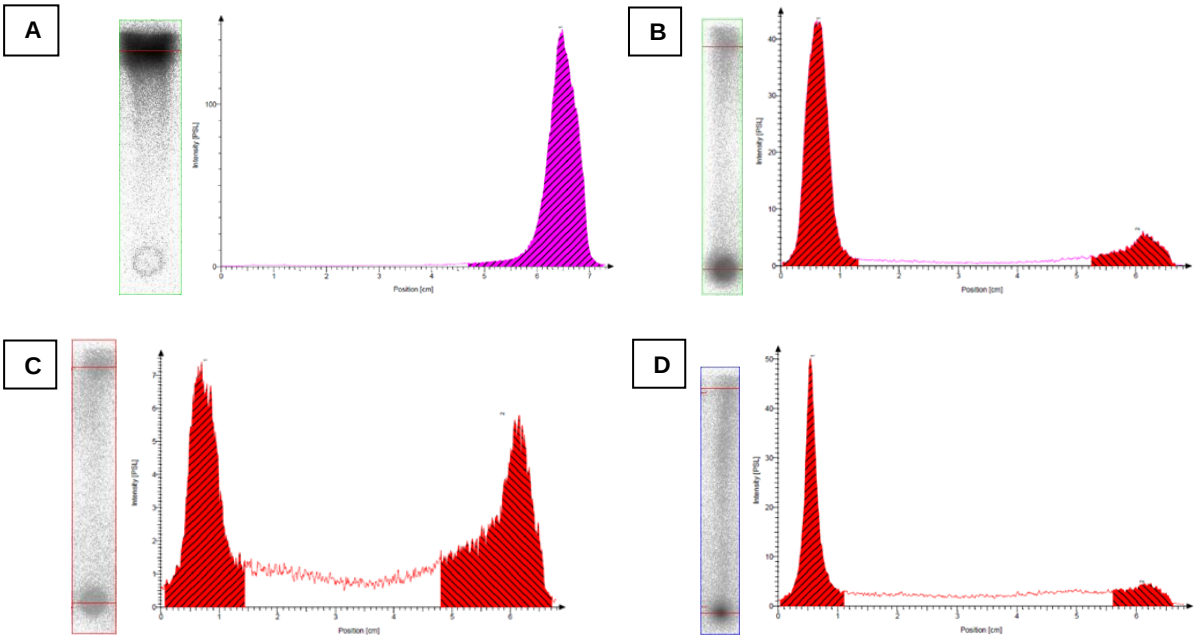

Figure 37. TLC plates evaluated under autoradiography. Exposed plate is on the left, radiation intensity in PSL versus position in cm on the right. **(A)** Free [^{68}Ga]$GaCl_3$, **(B)** [^{68}Ga]Ga-Ethanolamine, **(C)** [^{68}Ga]Ga-PEG-ethanolamine and **(D)** [^{68}Ga]Ga-DFO-Ethanolamine purified radiolabeled borosilicates. 2.2-µm microparticles.

- APTES functionalization: ^{68}Ga-labeling Experiment 2

Free [^{68}Ga]$GaCl_3$ was also spotted only for visual comparison with the final product. Unfortunately, purified versions of the radiolabeled [^{68}Ga]Ga-unmodified, [^{68}Ga]Ga-HCl cleaned and [^{68}Ga]Ga-APTES precursors cold not be subjected for evaluation in this case.

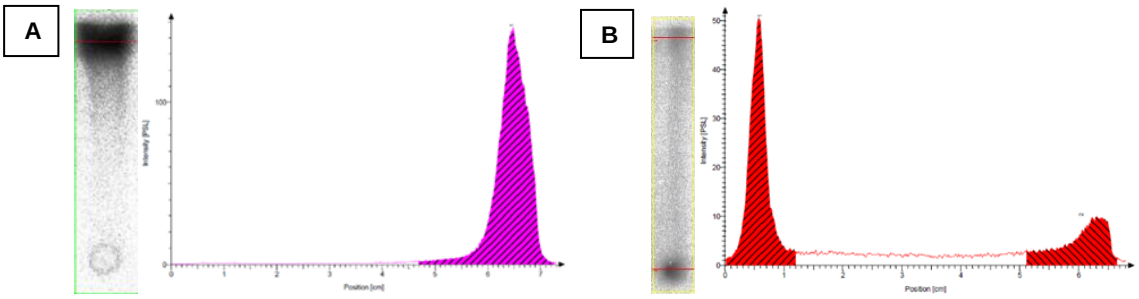

Figure 38. iTLC plates evaluated under autoradiography. Exposed plate is on the left, radiation intensity in PSL versus position in cm on the right. **(A)** Free [^{68}Ga]$GaCl_3$ and **(B)** [^{68}Ga]Ga-DFO-APTES purified radiolabeled product. 2.2-µm microparticles.

- APTES functionalization: ^{68}Ga-labeling Experiment 3

In this case, free [^{68}Ga]$GaCl_3$ was also spotted only for visual comparison with the radiolabeled products.

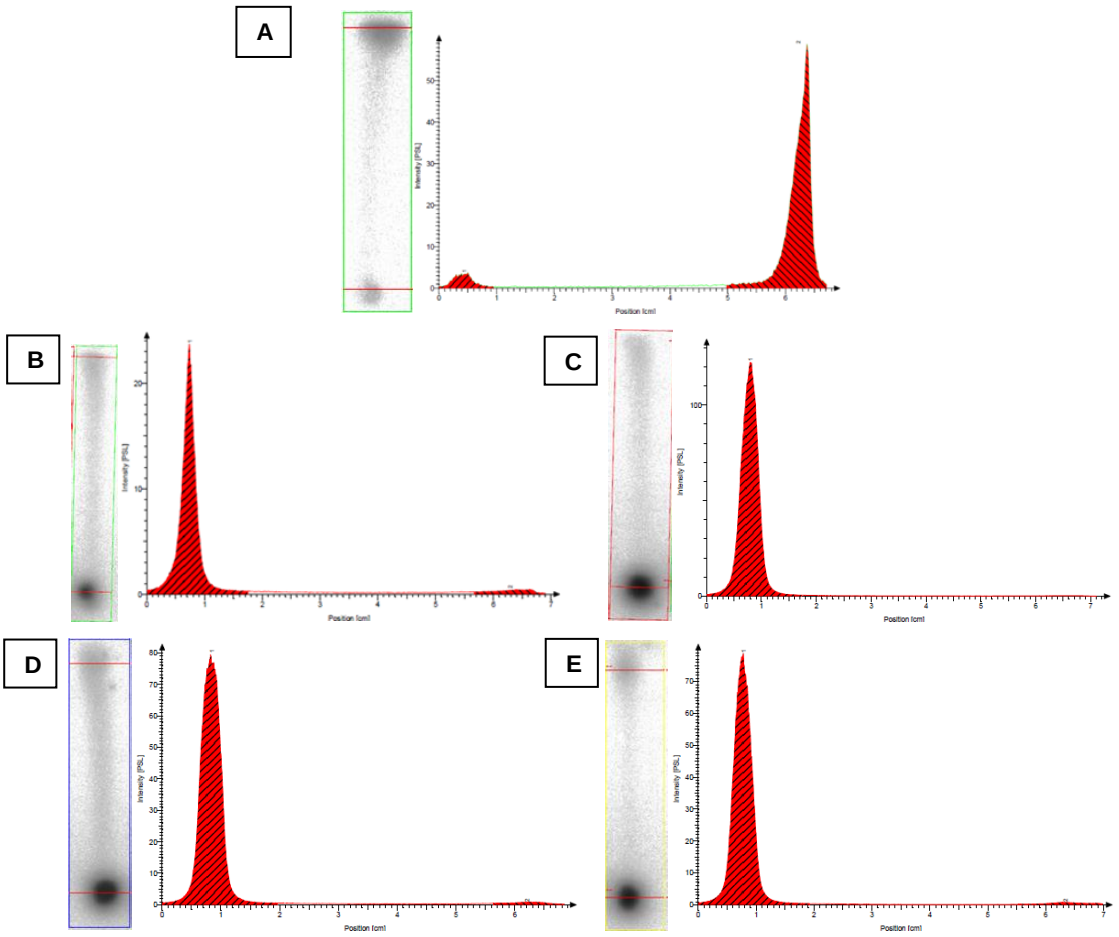

Figure 39. iTLC plates evaluated under autoradiography. Exposed plate is on the left, radiation intensity in PSL versus position in cm on the right. **(A)** Free [^{68}Ga]$GaCl_3$, **(B)** [^{68}Ga]Ga-Unmodified, **(C)** [^{68}Ga]Ga-HCl cleaned, **(D)** [^{68}Ga]Ga-APTES and **(E)** [^{68}Ga]Ga-NODAGA-APTES purified radiolabeled product. 2.2-µm microparticles.

- APTES functionalization: ^{68}Ga-labeling Experiment 3

In this case, free [^{68}Ga]$GaCl_3$ was also spotted only for visual comparison with the radiolabeled products.

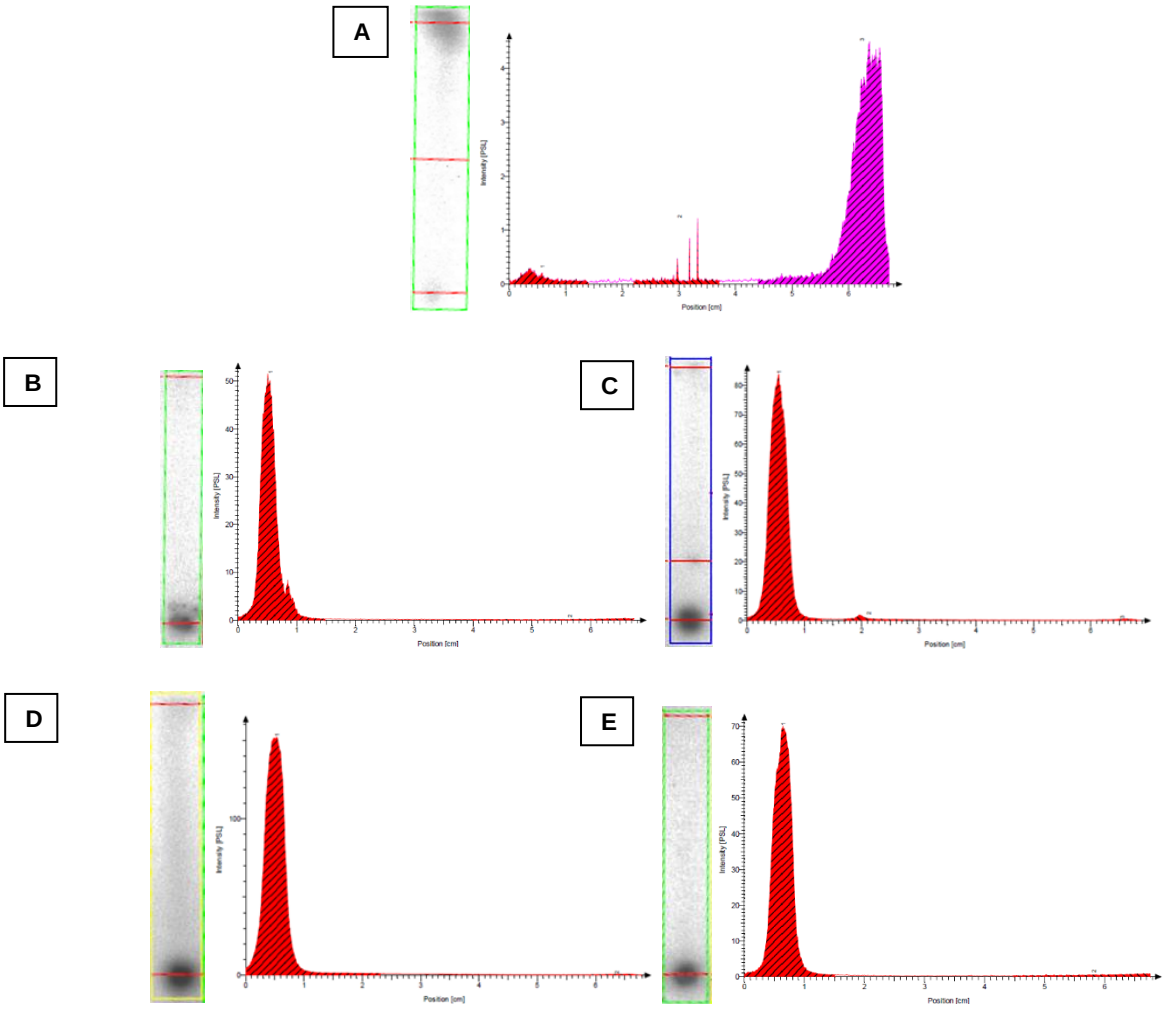

Figure 40. TLC plates evaluated under autoradiography. Exposed plate is on the left, radiation intensity in PSL versus position in cm on the right. **(A)** Free [^{68}Ga]$GaCl_3$, **(B)** [^{68}Ga]Ga-Unmodified, **(C)** [^{68}Ga]Ga-HCl cleaned, **(D)** [^{68}Ga]Ga-APTES and **(E)** [^{68}Ga]Ga-NODAGA-APTES purified radiolabeled product. 2.2-µm microparticles.

- ^{18}F-fluorination

  Correspondent iTLCs of the radiofluorination approach.

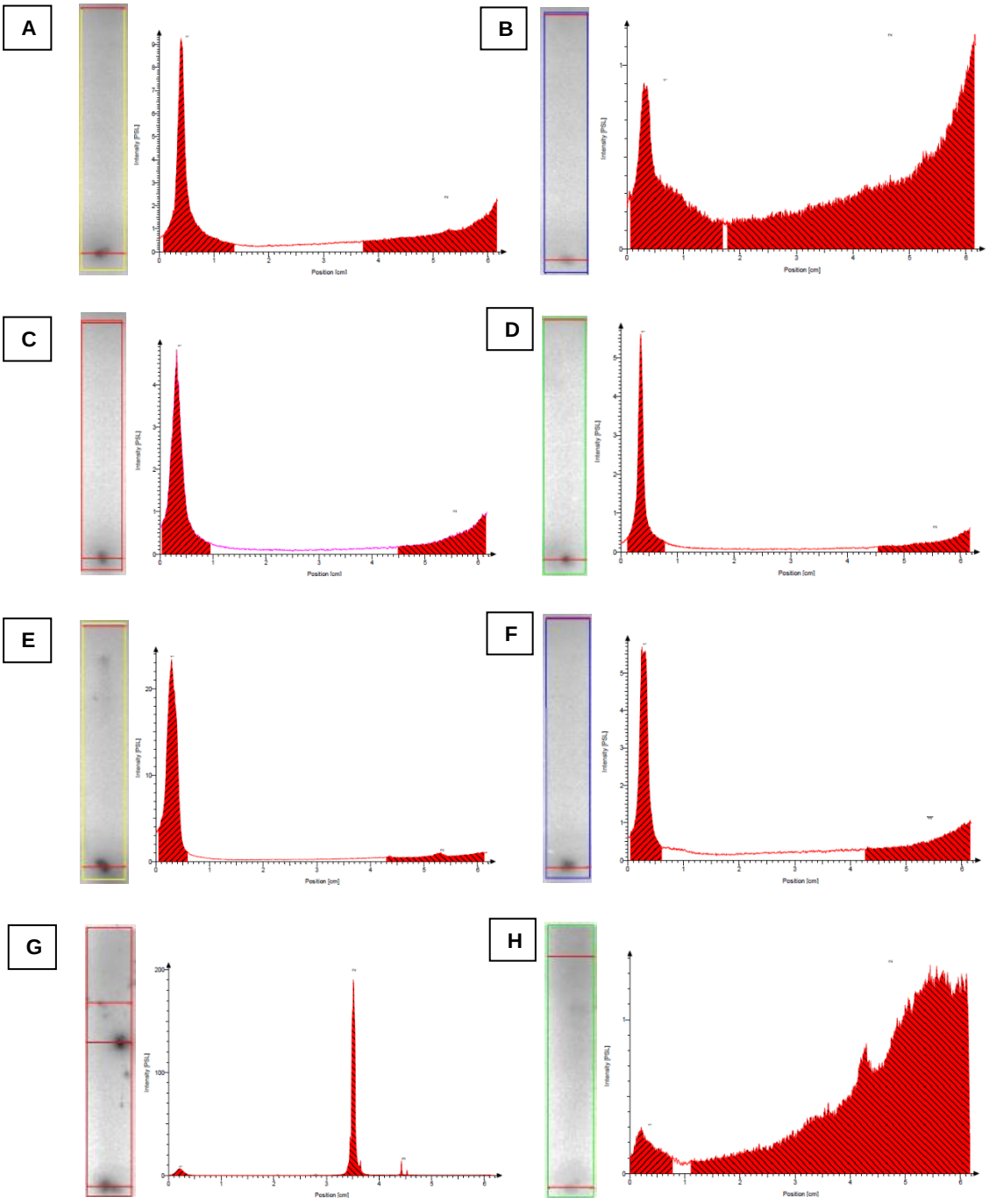

Figure 41. iTLC plates evaluated under autoradiography. Exposed plate is on the left, radiation intensity in PSL versus position in cm on the right. **(A, C, E, G)** [^{18}F]F-Unmodified and **(B, D, F, H)** [^{18}F]F-HCl cleaned for sets 1-4 respectively.